Far-infrared Radiation Response of Antenna-coupled Quantum-effect Devices

by

Rolf A. Wyss

B.S. Physics, Massachusetts Institute of Technology (1987)
M.S. and E.E., Massachusetts Institute of Technology (1990)

Submitted to the Department of Electrical Engineering and Computer Science
in partial fulfillment of the requirements for the degree of

Doctor of Philosophy

at the

MASSACHUSETTS INSTITUTE OF TECHNOLOGY

September 1995

Author .....
Department of Electrical Engineering and Computer Science
July 28, 1995

Certified by 7/31/95
Qing Hu
Associate Professor of Electrical Engineering
Thesis Supervisor

Accepted by .....
F. R. Morgenthaler
Chairman, Departmental Committee on Graduate Students

Far-infrared Radiation Response of Antenna-coupled Quantum-effect Devices

by

Rolf A. Wyss

Submitted to the Department of Electrical Engineering and Computer Science
on July 31, 1995, in partial fulfillment of the
requirements for the degree of
Doctor of Philosophy

Abstract

This thesis explores the high-frequency transport characteristics of two quantum effect devices: the quantum point contact and the lateral dual gate field-effect transistor (FET). Electron transport in these devices is predominantly phase coherent, since transport takes place in two-dimensional electron gas with high mobility. Phase-coherent devices can detect radiation with quantum-limited sensitivity, making them ideal photodetectors. Quantum phase-coherent devices such as ours respond best to radiation whose photon energy is nearly equal to the devices' subband energy spacing, thus we have measured the photoconductive response of our devices to millimeter-wave and far-infrared radiation.

The quantum effect devices were fabricated using an AlGaAs/GaAs modulation-doped heterostructure. Radiation was coupled to each sub-micron sized device with a planar, self-complementary antenna. This antenna focussed the radiation field and produced an ac voltage across the device which sinusoidally modulates the electrostatic potential.

The relationship between the efficiency of modulation quanta absorption by ballistic electrons and the confinement of the time-oscillating electric field was investigated. The motion of the electrons, initially represented as a Gaussian wavepacket, through single and double barrier potentials was found by direct integration of the time-dependent Schrödinger equation. We found that efficient absorption occurs in the classically forbidden regions if the time of interaction is on the order of the period of the oscillations and the ac voltage amplitude is larger than the photon energy divided by the electronic charge.

In the first set of experiments, the transport characteristics of a quantum point contact (QPC) were measured. The energy level structures of a quantum point contact was found by measurement of the temperature dependence of the transconductance and using perpendicular magnetic fields. Radiation experiments in the frequency range from 90 GHz to 2.5 THz reveal that the radiation-induced currents are caused by heating of the electron gas and rectification. Complete reversal of the polar-

ity of the radiation-induced current was achieved for a QPC with a gate coupled antenna by changing the direction of incidence of the radiation. The radiation-induced current was successfully described with a one-dimensional thermopower model accounting for unequal heating of the drain and the source electron reservoir. The radiation-induced current for a QPC with a drain/source coupled antenna was caused by rectification.

In the second set of experiments, the transport characteristics of the lateral dual gate FET was measured. The energy level structures of a symmetric and an asymmetric gate design were found from dc $I - V$ characteristic. We found the resonant level spacings near the top of the barriers agreed well with predictions based on a potential profile model we developed. Measurements of the radiation-induced currents for an asymmetric dual gate FET at 90 and 270 GHz showed a distinctive frequency dependence. The measurement results agreed well with calculations based on Tien-Gordon theory of photon-assisted tunneling and including the energy-dependent transmission coefficient.

Thesis Supervisor: Qing Hu
Title: Associate Professor of Electrical Engineering

Acknowledgments

I have been at MIT for many years and I have had the pleasure of working with many people who were excited about their work and executed it with great skill. I have been fortunate enough to participate in a worthwhile scientific endeavour. In particular, I thank Professor Qing Hu for providing my PhD thesis project and the neccessary means to perform the work. I also thank my academic advisor and thesis reader Professor Terry P. Orlando for patching me together multiple times, and steering me away from disaster. I thank Professor Jesús del Alamo and Dr. Cris C. Eugster for our initial collaboration and providing me with my first devices. I also like to mention Professor Dimitri Antoniadis for acting as a thesis reader and Professor Steve Senturia for helping me through my oral and area qualification exams.

Members of our research group deserve special mention. Thomas Schäpers, who has found the perfect balance in life between hard work and time for fun; Noah Zamdmer for his diligent reading and correction of my poor writing; Simon Verghese, Gert de Lange, Jurgen Smet, Jim Ernstmayer, Bin Xi, Elliot Hui and Farhan Rana who with their skill expanded my knowledge. I am indebted to David Greenberg for sharing his processing knowledge and Thalia Rich for sharing her computer account to run the space-consuming simulations. I particular like to thank Dr. Mike Rooks at the National Nanofabrication Facility at Cornell University for his intense efforts to help fabricate my many designs, Professor Mike Melloch at Purdue University and Dr. Arno Förster at KFA Jülich for the MBE growth of high electron mobility GaAs/AlGaAs heterostructure films.

I am also grateful for the assistance of Professor Hank Smith, James Carter and Mark Mondol of the Submicron Structures Laboratory for numerous e-beam evaporations, Richard Perilli and Tim McClure of the Microelectronics Laboratory at MIT; and Robert Cuikey and Paul Tierney at MTL for teaching me the basics of bonding and making masks.

My education at MIT did not only require sacrifices on a personal behalf, but also put demands on the pocket book of family members and neglecting time with loved ones. I would like to thank my fiancé, Wendy Hunter, for patiently enduring a two year long-distance relationship and my parents for financially supporting my education. I also would like to pay respect to my godfather who inspired and supported me through all the years and thank Dr. C. Hunter for the critical last minute editing of this work.

Contents

List of Figures

List of Tables

Chapter 1

Introduction

1.1 Motivation

Advances in semiconductor crystal growth and lithographic techniques have made it possible to achieve ballistic electron transport in specially designed material geometries. These ballistic electrons suffer virtually no scattering over length scales comparable to the device size. This absense of scattering has been experimentally verified for the first time by the observation of quantized steps in the conductance of point contacts by van Wees *et al.* [1] and Wharam *et al.* [2]. The study of quantum-effect devices, in which ballistic electron transport is achieved, has grown into one of the most active research fields in solid state physics. The manifestations of ballistic electron transport in point contacts have been studied in the nonlinear regime [3] and in magnetic fields [4, 5]. Specific device geometries have also been designed to observe interference phenomena due to the ballistic electron propagation in these one-dimensional waveguides. Resonant transport through zero-dimensional states in a series ballistic point contacts has been reported by Hirayama and Saku [6], interference phenomena in a double bend quantum wire has been measured by Wu *et al.* [7], and devices have been proposed and investigated based on the principle of

directional coupling between two electron waveguides [8]. The signature of resonant transport has also been observed in lateral dual gate field-effect devices, where the interference effects are caused by ballistic electrons traversing a double barrier electrostatic potential [9, 10]. The transport of ballistic electrons has even been studied through a two-dimensional potential gratings by Ismail *et al.* [11].

The common denominator of all these experimental efforts has been the study of the dc transport properties of quantum-effect devices. Studies of ballistic transport in the presence of ac modulated potential barriers have to date been predominantly limited to theoretical studies [12]. Galeczki [13] and Nimitz [14] proposed to take advantage of the reduced dimensionality of quantum-effect devices to build new types of far-infrared detectors. A detailed design of a quantum point contact for radiation detection has been discussed by Hu [15]. In particular, the analysis focussed on the theoretical limit of the responsivity that ballistic detectors might achieve in the far-infrared frequency range.

Today, the two most commonly used heterodyne detectors in the submillimeter frequency range are the superconducting-insulator-superconducting (SIS) tunnel junctions [16] and the Schottky diode [17]. The advantage of an SIS tunnel junction is that it offers near quantum-limited sensitivity for photon energies below the superconducting gap energy. Electrons tunneling through the insulator barrier in these device do not suffer inelastic scatterings and the transport is phase-coherent. The superconducting state of the contacts insures strong confinement of the radiation field and photon-assisted transport (PAT) is efficient. These detectors operate therefore close to the theoretical detection limit. The ideal performance of these devices at low radiation frequencies is however not achievable when the energy of the photon approaches the superconducting gap energy. For $Nb/Al_3O_2/Nb$-junctions this frequency is $\sim$700 GHz. Above this cut-off frequency the junction becomes very lossy. The pro-

cess responsible for photo-detection in SIS tunnel junction, PAT, is well-known in the field of superconductivity. Modulation quanta with the energy of a photon can be absorbed by quasi-particles close to the superconducting-insulator interface. Subsequently, these electrons can then tunnel through the insulator to the other side of the junction and contribute to the photocurrent. These devices have proved superior to any other radiation detectors in terms of sensitivity [18]. The speed of SIS tunnel junctions is determined by the junction capacitance and the series resistance. The resistance is chosen to optimize radiation coupling into the device by matching it to the antenna impedance. The capacitance is determined by the insulator film thickness. Typical values for a high-quality tunnel junction are 50 Ω and 10 fF, respectively [16]. The resulting roll-off frequency of this SIS device is hence 300 GHz. In contrast, the Schottky diode does not achieve photon-limited responsivity because the detection process in this device is classical. The main advantage of the Schottky diode is that it offers an acceptable photo-response up to very large frequencies. Schottky diodes have been made with series resistances of 20 Ω and with junction capacitances as small as 0.25 fF [19]. The figure-of-merit of these junctions is as high as 30 THz, far exceeding the SIS tunneling junction frequency cut-off. However, since the electrons in Schottky diodes do not propagate ballistically the detector response is not photon limited.

The objective of this work is to experimentally investigate if PAT can be achieved in quantum-effect devices. This would provide not only the photon-limited sensitivity of SIS tunnel junctions but possibly also exceed its upper frequency limit. The lack of experimental evidence to date for the PAT process in semiconductors and the successful utilization of the phenomena in the field of superconductivity provided therefore the motivation to investigate the manifestations of the process in quantum-effect devices. The study of PAT in quantum-effect devices can contribute substantially to

our understanding of the high-frequency behavior of quantum transport phenomena in semiconductors. This research may also lead to the development of novel long-wavelength optoelectronic devices and hence benefit the field of submillimeter-wave and THz detection.

1.2 Approach

The study of quantum effects in semiconductor materials has largely been made possible by advances in the growth of high-quality crystal film [20]. The material system of choice for most investigators, including us, has been GaAs because it is a well-characterized material system. An extensive review of quantum mechanical transport in this material system is given by Timp and Howard [21].

In Fig. 1-1(a) we have illustrated the basic material layers of a molecular beam epitaxy (MBE) grown film. Starting from the bottom, a thick intrinsic layer of GaAs is grown, then an undoped AlGaAs layer, then an n-doped AlGaAs layer and finally a thin GaAs cap layer on top. A schematic view of the conduction band profile is shown in Fig 1-1(b). The Fermi level for the GaAs cap layer is located at midgap because we assumed a high density of surface states. For a sufficiently high doping density in the AlGaAs layer a significant conduction band bending is achieved. By clever choice of doping profile the conduction band for the GaAs can dip below the Fermi energy in the vicinity of the heterointerface. Consequently, a sharp, approximately triangular conduction band profile forms with quantized energy levels inside the GaAs layer. By proper adjustment of the doping concentration in the AlGaAs layer it is possible to selectively populate only the lowest energy level, as indicated in Fig 1-1(b). The doping in these structures is restricted to a few Si-atom monolayers in the doped AlGaAs layers; a technique referred to as δ-doping. This doping techniques separates the donors atoms spatially from the conduction channel in the GaAs by a few 100 Å.

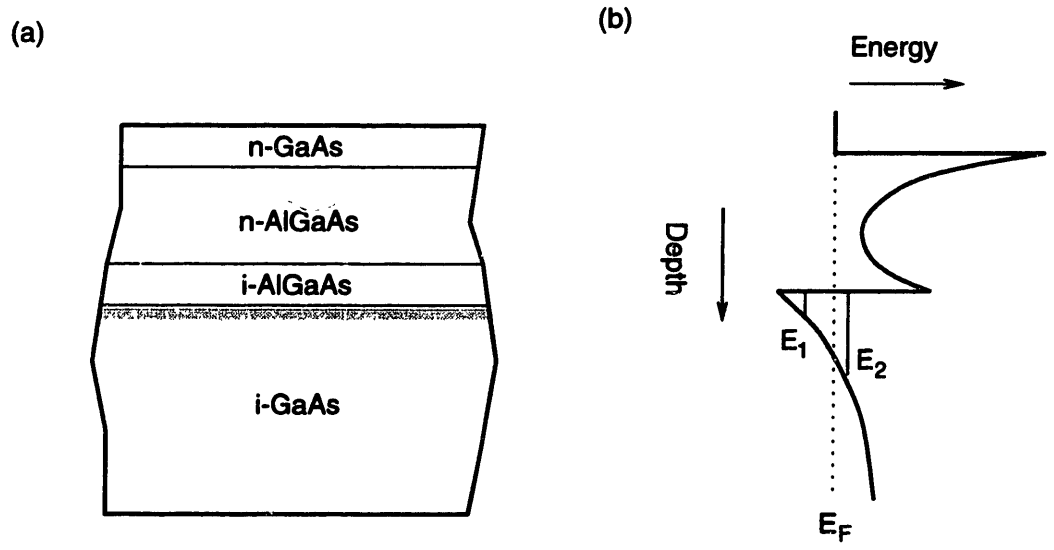

Figure 1-1: (a) Individual growth layers for modulation-doped AlGaAs/GaAs heterostructure used for vertical confinement. (b) Diagram of conduction band profile of heterostructure.

The use of the AlGaAs separation layer, commonly referred to as a spacer layer, serves to decrease the scattering rate of the electrons by placing donor atoms remote to the conduction channel. The conduction electrons confined to the lowest energy state at the heterointerface can move freely in the plane of the interface. This sheet of highly mobile electrons is referred to as a two-dimensional electron gas (2DEG). High mobilities have been achieved in substrates with such MBE-layers and we have therefore utilized this structure for fabrication of our devices.

The two-dimensional motion of the electrons in the 2DEG can be further restricted. Application of negative voltages to Schottky electrodes patterned on top of the substrate surface can selectively deplete the 2DEG. The geometry of the gate pattern can be designed as desired. If however, the motion of the electrons is constrained to a dimension smaller than the Fermi wavelength, λ_F, quantum mechanical effects start to play a significant role in the electron transport. These quantum mechanical

effects is what forms the basis for the quantum-effect devices we will study [22].

1.3 Overview of this work

In chapter 2 we investigate the phenomena of absorption and emission of modulation quanta by ballistic electrons while they propagate in a spatially varying, sinusoidally oscillating potential. We develop a model for the effective dc potential barrier an electron experiences while propagating between the drain and the source contacts. This model is consequently used to study the efficiency of modulation quanta absorption by ballistic electrons while tunneling through a single and a dual barrier potential. The study of the electron wavepacket propagation is performed using numerical techniques by direct integration of the time-dependent Schrödinger equation. The numerical approach allows variation of the degree of spatial confinement of the ac electric field. The dependence of the absorption efficiency on the tunneling time, the oscillation frequency, and the ac electric field confinement is explored. On the basis of this study we find that a number of experimental conditions which must be satisfied to make the absorption process experimentally observable.

In chapter 3 we present the device design choices we made. The heterostructure layers, the radiation coupling scheme, and the device fabrication process are discussed. We then show and explain two of the device designs we have studied. At last, an account is given of the experimental measurement system.

We then present the experimental findings for the quantum-effect devices we have studied: the quantum point contact (QPC) and the lateral dual gate device. In chapter 4 we explain the dc transport characteristics of a QPC. We adapt the saddle-point potential profile model to describe the electrostatic potential of a QPC at the constriction. We then present a novel method which relates the current-voltage ($I-V$) characteristics of a QPC to the curvatures of the saddle-point potential. Numerical

estimates for the curvatures of the potential are valuable since they are directly related to the device's transmission coefficient and subband energy spacing. In chapter 5 the results of radiation measurements using a QPC are presented for two orthogonal radiation coupling structures: (1) the antenna is connected to the gate leads of the QPC; and (2) the antenna is connected to the drain and the source ohmic contacts. In the second approach, the tight confinement of the ac electric field is achieved by extending the antenna terminals beyond the position of the ohmic contacts to within microns of the active device region.

In chapter 6 we present the dc transport measurements of lateral dual gate devices. The structures in the device's $I - V$ characteristic are analyzed using the potential profile model derived in chapter 2. By comparison of the structures in the theoretical $I - V$ characteristic to measurement results an understanding of the device behavior is achieved. In chapter 7 we present the results of radiation measurements for the lateral dual gate devices. Finally, we conclude our study with chapter 8 with a brief discussion of future research opportunities.

Chapter 2

Radiation-enhanced transport

2.1 Introduction

This chapter presents a theoretical investigation of electron transport through a quantum-effect device in the presence of a radiation field. Many authors have investigated the frequency dependence of ballistic transport through ac modulated single barrier [23, 24, 25] and double barrier [12, 26, 27, 28]. We will examine the interaction of ballistic electrons with ac modulated barriers by direct simulation [29]. The algorithm we used to solve the time-dependent Schrödinger equation was written by de Raedt and Michielsen [30].

In section 2.2 we examine the case in which the radiation field induces a sinusoidally varying ac voltage between the electrochemical potentials of the drain and the source electron reservoirs. We find that the effect of the ac voltage can be described mathematically as a splitting of the electron density in one of the electron reservoirs into sidebands. In section 2.3 and section 2.4 we develop a procedure to calculate the dc current through a device in the absence of a radiation field. In this procedure an approximate method is introduced for determining the electrostatic potential of a device along the direction of charge transport, and using the transmission-matrix

method (TMM) to calculate the transmission coefficient [31]. The transmission coefficient is then used to find the dc current. In section 2.5 we return to the study of the effects of a radiation field on transport through both a single and a double barrier device. This is achieved by analyzing the transmission of a Gaussian electron wavepacket through a time-oscillating potential by numerical integration of the time-dependent Schrödinger equation. We discuss both the influence of the dc potential barrier and the ac voltage confinement on the energy absorption of ballistic electrons. The key findings of this chapter are summarized in section 2.6.

2.2 Theoretical background

Section 2.2 studies the response to a radiation field for an idealized device. This treatment follows closely the derivation given by Tien and Gordon [32]. We assume that the radiation field induces a sinusoidally varying ac voltage between the drain and the source electrochemical potentials. For the case we consider no ac voltage is present inside the electron reservoirs, the electric field is entirely confined to the barrier region separating the drain and the source contacts. In the absence of the radiation field, we can approximate the envelope function of the total electronic wavefunction as

$$\psi_0(\mathbf{r}, t) = f(\mathbf{r})e^{-iEt/\hbar} \tag{2.1}$$

which is an eigenfunction of the unperturbed Hamiltonian H_0. This wavefunction describes the electron distribution in both contacts. The ac voltage difference V_{ac} between the electrochemical potentials of the two contacts due to the radiation field can be written as

$$V_{\mathrm{ac}}(t) = V_1 \cos \omega t, \tag{2.2}$$

where V_1 is the maximum amplitude of the ac voltage and $f = \omega/2\pi$ is the frequency of the radiation field. Without sacrificing generality, the electrochemical potential of one of the contacts, for example the drain, can be considered fixed; while the other, the source, is modulated by addition of Eq. 2.2. Since the ac voltage is spatially uniform throughout the source reservoir and zero in the drain reservoir, only the time-dependence part of the electronic wavefunction in the source is modified. By substituting the trial wavefunction $\psi_s(\mathbf{r}, t) = \psi_{s0}(\mathbf{r}, t)g(t)$ into the time-dependent Schrödinger equation with the modified Hamiltonian $H_0 + eV_{\text{ac}}$ we have

$$i\hbar\frac{\partial}{\partial t}\psi_s(\mathbf{r}, t) = (H_0 + eV_{\text{ac}})\psi_s(\mathbf{r}, t). \tag{2.3}$$

After substitution of the trial wavefunction $\psi_s(\mathbf{r}, t)$ into Eq. 2.3 we find that $g(t)$ must satisfy the following differential equation

$$\frac{dg(t)}{dt} = -i\frac{eV_1}{\hbar}g(t)\cos\omega t. \tag{2.4}$$

An exact solution for $g(t)$ can be found by direct integration of Eq. 2.4,

$$\ln g(t) = -i\frac{eV_1}{\hbar}\int^t \cos\omega t' dt'. \tag{2.5}$$

After subsitution of $g(t)$ into the trial wavefunction we find

$$\psi_s(\mathbf{r}, t) = \psi_{s0}(\mathbf{r}, t)e^{-i\alpha\sin\omega t}, \tag{2.6}$$

where the dimensionless parameter α is defined as

$$\alpha \equiv \frac{eV_1}{\hbar\omega}. \tag{2.7}$$

This parameter compares the maximum amplitude of the ac potential to the radiation frequency. It is helpful to further manipulate the solution for $g(t)$ and write it in a series representation

$$\sum_{n=-\infty}^{\infty} B_n e^{-in\omega t} = e^{-i\alpha \sin \omega t}. \tag{2.8}$$

The coefficients B_n in the expansion are found by differentiating both sides with respect to the time variable t. By equating equal powers of ωt we find the coefficients obey the recursive relationship $2nB_n = \alpha(B_{n+1} + B_{n-1})$. This relationship is satisfied by the Bessel function of n-th order $J_n(\alpha)$, hence $B_n \equiv J_n(\alpha)$ [35]. By collecting the above results the new wavefunction given in Eq. 2.6 can be written in the equivalent form

$$\psi_s(\mathbf{r}, t) = f_s(\mathbf{r}) \sum_{n=-\infty}^{\infty} J_n(\alpha) e^{-i(E+n\hbar\omega)t/\hbar}. \tag{2.9}$$

This new notation makes it easier to interpret the results of the ac voltage perturbation. We find that the unperturbed wavefunction with energy E has been split into new eigenstates having the same spatial dependence but with energies $E + n\hbar\omega$ and amplitudes $J_n(\alpha)$. A positive value of n means the eigenstate has absorbed energy from the ac voltage perturbation while a negative value of n means the eigenstate has emitted energy to the ac voltage perturbation. The corresponding electron densities of these radiation-induced eigenstates are $J_n^2(\alpha)$. We conclude that the electron density in each sideband depends on the amplitude of the ac voltage and hence on the strength of the radiation field. The Bessel function behavior of the sidebands is characteristic of a purely sinusoidal time-perturbation of the Hamiltonian.

The main result in this section has been to show how new electron eigenstates are formed in the presence of a sinusoidally varying voltage. In the next two sections we will focus on the dc transport properties of a quantum-effect device. We will find the effective potential profiles and the transmission coefficients which will make it possible to calculate the dc current through the device. We will then incorporate the

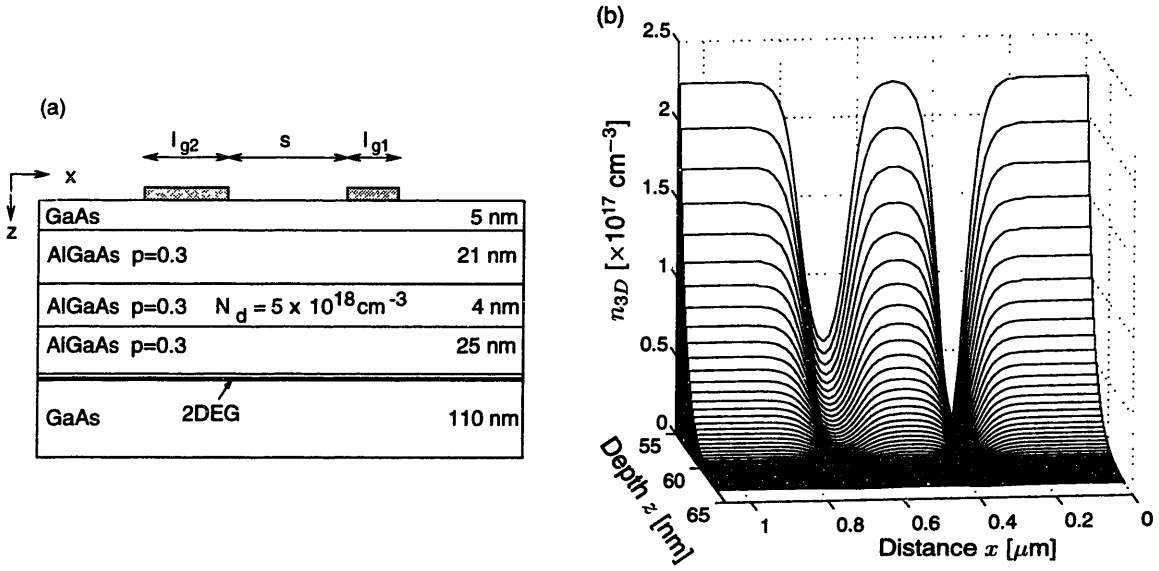

Figure 2-1: (a) Cross section of $Al_pGa_{1-p}As/GaAs$ heterostructure. The 2DEG is located inside the GaAs layer 55 nm below the substrate surface. Two gates, with length l_{g1} and l_{g2} separated by s are shown. A donor density of $N_d = 5 \times 10^{18}$ cm^{-3} was used in the simulation. The variable p indicates the fractional content of Al, i.e. $Al_pGa_{1-p}As$. (b) Three-dimensional charge distribution $n_{3D}(x, z)$ for voltages $V_{g1} = -0.65$ V and $V_{g2} = -0.3$ V applied to gate 1 and 2, respectively. The dimensions used in the simulation are $l_{g1} = 50$ nm, $l_{g2} = 130$ nm and $s = 250$ nm.

results of this section to find the radiation-induced current through the device.

2.3 Potential-profile model

In this section we derive a model for the effective electrostatic potential an electron in the two-dimensional electron gas (2DEG) encounters while propagating between the source and the drain reservoirs. Although analytical expressions have been derived for varies shaped gate geometries [33] we have resorted to solving the two-dimensional Poisson equation numerically [34]. We will first find the three-dimensional electron charge distribution in the AlGaAs/GaAs heterostructure as a function of the voltage applied to a gate on the surface. The resulting charge distribution in the GaAs is then

integrated along a direction normal to the heterojunction interface and equated with the 2DEG charge density. The 2DEG charge density is then related to an effective conduction band bending, or, equivalently, to a potential profile.

Figure 2-1(a) shows a cross-section of the AlGaAs/GaAs heterostructure we used for device modeling. The dimensions chosen for the individual layers are representative for the MBE-grown substrates we have used for fabrication of our devices (see Table 3.1). The two shaded areas on top of the 5 nm thick GaAs cap layer represent the gates which are used to deplete the 2DEG. By solving the two-dimensional Poisson equation for this structure we have found the three-dimensional charge distribution, $n_{3D}(x,z)$ [34]. In the simulation we used the following boundary conditions: the gates were treated as Schottky contacts and the Fermi level at the surface for the bare GaAs was pinned at mid-gap. The Si-donor dopant density in the 4 nm thick AlGaAs layer, which was taken to be fully ionized, was adjusted by trial-and-error until the desired 2DEG charge density of 3.6×10^{11} cm^{-2} was obtained for the case when no voltage was applied to the gates; this value corresponded to a Fermi energy of 12.9 meV, which was typical for our MBE structures. A spatial mesh size of 7.5 nm in the x-direction was used, while in the z-direction it was set to 1 nm in the GaAs cap layer, 2.5 nm in the AlGaAs layers, and 2 nm in the bottom GaAs layer. Figure 2-1(b) shows $n_{3D}(x,z)$ below the AlGaAs/GaAs heterointerface when we applied a negative voltage to the gates on the surface. In this simulation run, the gate lengths were set to 50 nm and 130 nm with a separation of 250 nm. The voltage applied to the short gate was -0.65 V and the voltage applied to the long gate was -0.3 V.

The two-dimensional charge density of the 2DEG, $n_{2D}(x)$, is found by integrating $n_{3D}(x,z)$ along the z-direction throughout the bottom GaAs layer. The result of this integration is shown in Fig. 2-2(a), where n_{2D} is plotted for a 50 nm gate as a function of the x position for different values of the gate voltage. Based on such simulation

Table 2.1: Fitting parameters for functional description of the potential profile V. Parameters are valid for a 2DEG depth of 55 nm and gate lengths ranging from 40 nm to 160 nm.

n	β_n [eV/V·nm^n]	σ_n [μm/nm^n]
0	-9.308×10^{-4}	3.409×10^{-2}
1	-3.730×10^{-4}	7.775×10^{-5}
2	1.012×10^{-6}	7.547×10^{-7}

results using a gate length from 50 to 500 nm we find that the n_{2D} at the center of the gate decreases nearly proportionally with the applied gate voltage. Also, the overall characteristics of n_{2D} closely resemble an inverted Gaussian profile. For modeling purposes it is helpful to introduce a potential profile V, which effectively accounts for the conduction band bending. For a two-dimensional system, the density of states is independent of energy and we can write

$$E_F - V(x) = \frac{\pi\hbar^2}{m^*} n_{2D}(x), \tag{2.10}$$

where E_F is the Fermi energy of the undepleted 2DEG and m^* is the electron effective mass in GaAs. Eq. 2.10 relates the spatial dependence of the 2DEG charge density to the potential profile V. The potential profile can now be approximated by using a Gaussian function

$$V(x) = \beta V_g \exp\left[-\frac{(x - x_c)^2}{2\sigma^2}\right], \tag{2.11}$$

where x_c is the center position of the gate and V_g is the gate voltage. The scaling factor β and the width σ are expanded to second order in the gate length l,

$$\beta \equiv \sum_{n=0}^{2} \beta_n l^n \quad \text{and} \quad \sigma \equiv \sum_{n=0}^{2} \sigma_n l^n. \tag{2.12}$$

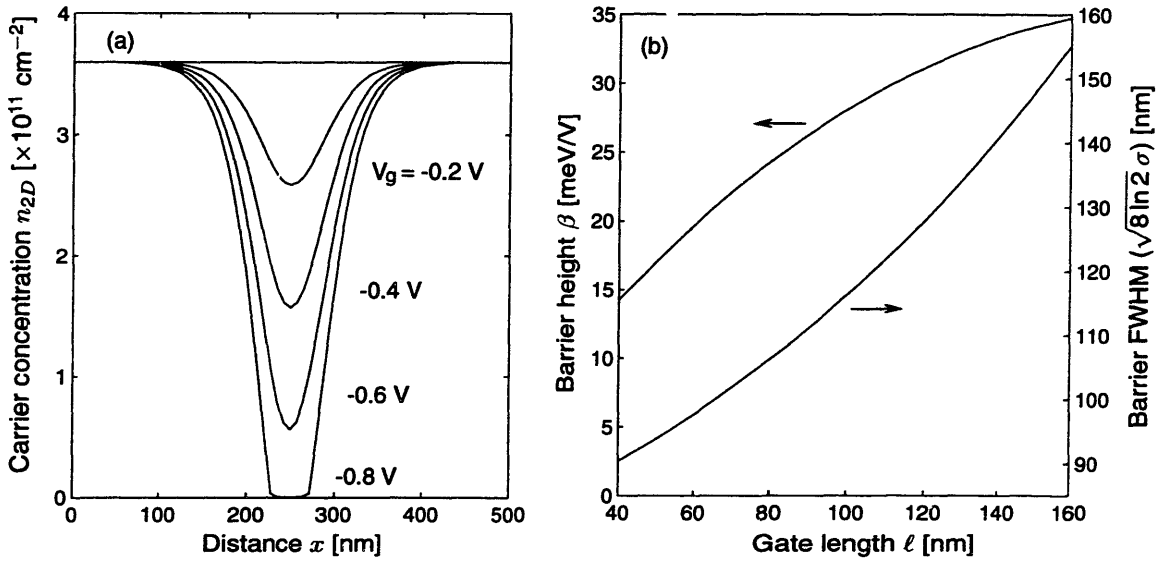

Figure 2-2: (a) Charge depletion of the electrons in the 2DEG for gate voltage values equal to 0 V, -0.2 V, -0.4 V, -0.6 V and -0.8 V. The gate length was 50 nm, the 2DEG depth was 55 nm, and the carrier concentration was 3.6×10^{11} cm^{-2}. (b) Scaling factor β and FWHM of Gaussian function describing the electrostatic potential as a function of gate length. The parameter values are based on two-dimensional Poisson simulation results of the cross-section shown in Fig. 2-1(a).

Numerical values for the fitting parameters β_n and σ_n are given in Table 2.1. A plot of β and σ as functions of the gate length is shown in Fig. 2-2(b). The FWHM is found to be limited to about 80 nm even for an infinitesimally short gate. This intrinsic broadening of the barrier potential exists because the 2DEG is located 55 nm below the substrate surface. From the values of β, we can extract values for the threshold voltage, V_t, which is defined as the voltage required for complete depletion of the charge at the center of the gate. For a gate length of 50 nm we have $\beta = -17$ meV/V. For a Fermi energy of 12.9 meV the threshold voltage is

$$V_t = E_F/\beta = -0.76\,\mathrm{V}.$$

The procedure we have used to derive n_{2D} is only approximately valid. We did not consider the formation of subbands at the AlGaAs/GaAs heterointerface due to the conduction band bending. Although we have matched the 2DEG charge density in our description to the real system, the depopulation with decreasing gate voltage is expected to differ and result in a smaller threshold voltage. This is not surprising, since the bottom energy of the lowest subband at the heterojunction interface does coincide with the conduction band energy. Typically, though, we found that the threshold voltage for a 50 nm gate device is -0.7 V when the device thermally cycled for the first time. This voltage is not very different from the prediction based on our simple model. The threshold voltage, however, can drift significantly over time because of fluctuation in the number and position of trapped charges.

2.4 Transmission coefficient

In this section, we calculate the transmission coefficient for a single and a dual gate structure using the transmission-matrix method (TMM) [31, 36]. These transmission coefficients can then be used to calculate the drain/source current through the devices.

We begin by analyzing the case for a dual gate structure. Figure 2-3 shows the resulting potential profile for such a structure. The gates used are 50 nm long, separated by 250 nm. The voltage applied to both gates is equal to -0.78 V, which places the top of the barrier, E_b, just above the Fermi energy E_F. In the simulation we set $E_F = 12.9$ meV and $E_b = 13.7$ meV.

For the 2DEG, assuming the parabolic energy dispersion holds, the total electron energy E of an electron can be separated into a longitudinal component E_x along the x-direction, and a transverse component E_y along the y-direction,

$$E = E_x + E_y = \frac{\hbar^2}{2m^*}(k_x^2 + k_y^2),$$

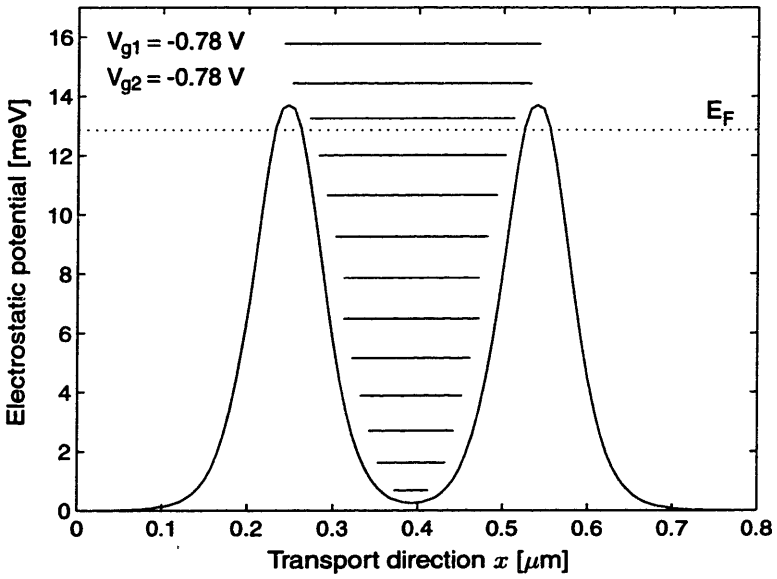

Figure 2-3: Conduction band profile for dual gate device along the transport direction. The length of both gates is 50 nm; they are separated by 250 nm. A voltage of -0.78 V is applied to both gates. The resonant levels between the two barriers are indicated by the horizontal lines.

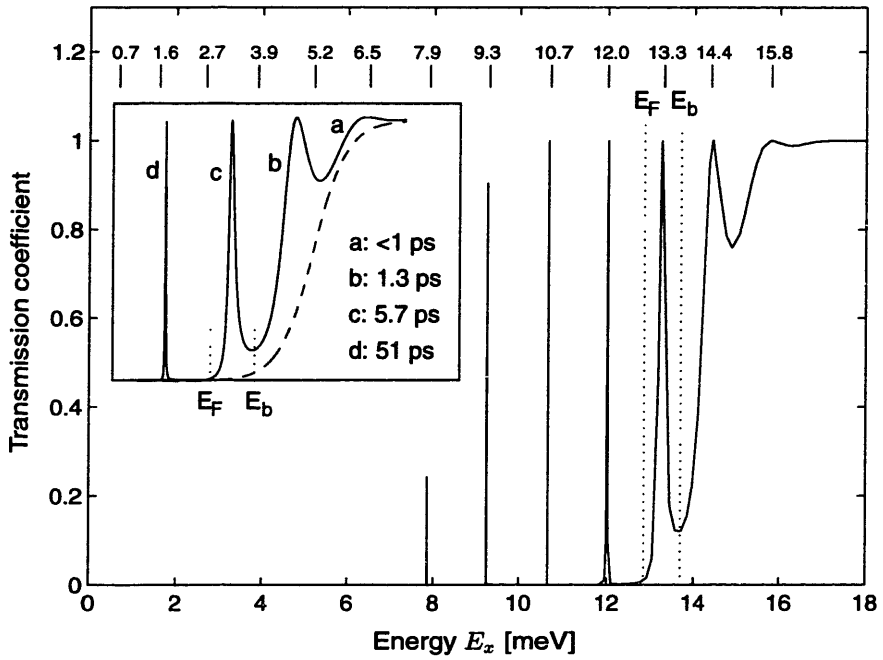

Figure 2-4: Transmission coefficient for a dual gate device as a function of longitudinal electron energy E_x. The length of both gates is 50 nm; they are separated by 250 nm. Resonant level energies are referenced with respect to the conduction band. Eleven quasi-bound states and two above-the-barrier resonant states are marked using short vertical lines along the top of the graph. The inset shows a detail of the four highest resonant levels with lifetimes τ ($\equiv \hbar/\Delta E$) [37]: <1, 1.3, 5.7 and 51 ps, in order of decreasing energy. The transmission coefficient for a single gate device with a barrier height of 14.4 meV is indicated by the dashed line.

where k_x and k_y are the electron wavevectors along the x- and y-direction, respectively. For a potential profile $V(x)$, which depends only on the position along the transport direction, the transmission coefficient for the electron propagating through the barrier is only a function of the electron's longitudinal energy E_x.

Using the TMM, we found several transmission resonances through the double barrier potential. A plot of the transmission coefficient $T(E_x)$ as a function of the electron injection energy E_x is shown in Fig. 2-4. Eleven resonant levels are found below the energy E_b, corresponding to the top of the potential barrier. Two addi-

tional resonant levels exist above E_b. The position of these levels with respect to the potential profile has been indicated in Fig. 2-3 by the vertical lines. The resonant level separation close to E_b is about 1.4 meV. The quasi-bound states far below E_b are extremely narrow in energy and hence have a very long lifetime. These levels do not contribute significantly to the current at measurement temperatures of $\sim$1 K and can be ignored. Only the two resonant levels located immediately above and below E_b may be important for the current flow, and an expanded plot of them is shown in the inset of Fig. 2-4. Experimental evidence for the two levels marked b and c is presented in chapter 7. The lifetime for these states is on the order of 10^{-12} s which represents an upper limit for the speed of ballistic electrons through the structure. In the inset we have also plotted the transmission coefficient through a single barrier potential, shown by the dashed line.

The transmission coefficient, calculated by the TMM, can be used to find the net current flow between the drain and the source contacts. Assuming each contact to be at thermodynamic equilibrium, each supplies electrons with an energy spectrum described by the Fermi-Dirac distribution function

$$f = \frac{1}{1 + e^{(E-\mu)/k_B T}},$$

where μ is the chemical potential of a contact. The drain/source current density J_{ds} is found by summing over all energies:

$$J_{ds} = e \int T(E_x) \left(\frac{1}{\hbar} \frac{\partial E}{\partial k_x} \right) (f_s - f_d) \frac{d^n \mathbf{k}}{(2\pi)^n}. \tag{2.13}$$

Here f_s and f_d are the Fermi-Dirac distribution functions for the source and the drain contacts with chemical potentials μ_s and μ_d, respectively. The externally applied drain/source voltage V_{ds} determines the difference between the two chemical

potentials, $V_{ds} = (\mu_s - \mu_d)/e$. The value of n (1 or 2) depends on the dimensionality of the propagating electrons. In this section we have illustrated the procedure by which dc current due to ballistic electron in a device can be calculated. We will now return to our discussion of the effect of radiation on the dc transport through a device.

2.5 Modified transmission coefficient

The objective in this section is to arrive at a method for predicting the effect of radiation on ballistic electron transport through a device. We have already learned that a spatially uniform sinusoidally oscillating ac potential leads to the formation of new eigenstates. We will now explore how the formation of these sidebands affects the dc drain/source current. In order to be able to explore realistic device geometries we decided to study the transmission through the time-oscillating barriers by numerical techniques. Such an approach enabled us to study both the radiation induced transport through a tunneling barrier as well as over-the-barrier processes.

2.5.1 Direct simulation

As explained above, we chose to study the radiation-induced transport through either a single or double barrier potential by numerical integration of the time-dependent Schrödinger equation (TDSE). The integration algorithm we used was developed by de Raedt and Michielson [30]. Similar simulation of the time evolution of the electron interaction with an ac potential has also been investigated by other researchers using a numerical path integral technique [29].

In our approach, the electron incident on the time-oscillating barrier is represented by a wavepacket. The incremental evolution in space and time of this wavepacket is

found by integration of the TDSE. If we write the potential profile as $V(x,t)$ then the TDSE is given by

$$\left\{-\frac{\hbar^2}{2m^*}\frac{\partial^2}{\partial x^2}+V(x,t)\right\}\psi(x,t)=i\hbar\frac{\partial}{\partial t}\psi(x,t), \tag{2.14}$$

where the Hamilonian $H(t)$ is equal to the expression in the bracket $\{\cdot\}$. If the wavefunction at time t is known, the solution of Eq. 2.14 at time $t+\tau$ is

$$\psi(x,t+\tau)=e^{-i\tau H(t)}\psi(x,t). \tag{2.15}$$

This relationship is used to update the wavefunction at each instance in time. Time-dependent Hamiltonian is updated accordingly to reflect the change in the potential due to the ac variation. The potential can be separated into two parts: (1) a time-independent dc potential $V_{\rm dc}(x)$ present in the case of no radiation, and a time-dependent contribution $eV_{\rm ac}(x,t)=\xi(x)\cos(\omega t+\phi)$ describing the spatial distribution of the sinusoidally varying ac potential. When the interaction time of the wavepacket with the potential $V(x,t)$ is short compared to the period of the ac oscillation, $2\pi/\omega$, the initial phase ϕ, assigned to the ac potential, becomes important. The total transmission is then found by averaging the transmission obtained when using many different initial phases. We found that using the values $\phi=0,\pi/4,\ldots,7\pi/4$ is generally sufficient. In the simulation, we assume that the screening of the ac potential becomes perfect beyond a characteristic distance $\xi_{\rm ac}$ from the center of the dc potential barrier, x_c; $\xi(x)$ is therefore constant for $|x-x_c|\gg|\xi_{\rm ac}-x_c|$. We should keep in mind that the simulation results presume perfect phase coherence for the electrons traversing the potential barrier.

An electron incident on the barrier is represented using a Gaussian wavepacket

$$\psi(x, t = 0) = \frac{1}{\sqrt{2\pi\sigma^2}} e^{-(x-x_0)^2/2\sigma^2} e^{ik_0 x}, \tag{2.16}$$

where the electron has been localized at $x = x_0$ at time zero and σ determines the spatial extent of the wavepacket. In the simulation $\sigma \gg 1/k_0$ and the mean energy of the wavepacket is therefore

$$E_0 = \frac{\hbar^2}{2m^*}\left(k_0^2 + \frac{1}{4\sigma^2}\right) \approx \frac{\hbar^2 k_0^2}{2m^*}.$$

The temperature broadening of the wavepacket can be estimated by equating the width of the step in the Fermi-Dirac distribution at temperature T_ψ to the FWHM of the wavepacket

$$3.5 k_B T_\psi = \sqrt{8\ln 2}\,\frac{\hbar^2}{2m^*}\frac{k_0}{\sigma}\sqrt{1 + \frac{1}{8\sigma^2 k_0^2}} \approx \frac{\sqrt{8\ln 2}}{k_0\sigma} E_0.$$

At an electron injection energy of $E_0 = 10$ meV with $\sigma = 12\pi/k_0 = 6\lambda_0 \approx 0.28$ μm we have $T_\psi \approx 2$ K. This broadening is comparable to the energy width of the resonant levels near the top of a dual barrier. We are therefore able to resolve these levels. In all simulation runs we set the spatial mesh size equal to $0.1\lambda_0$ and the time increment $\tau = 0.03125\hbar/E_0$. Using a value of $\sigma = 6\lambda_0$ reflected a compromise between sufficient energy resolution and a reasonable execution time for the simulation runs. A total system size of 2000 nodes was chosen which made it possible to simulate the evolution of the wavepacket for about 20 ps after interaction with the potential barrier.

2.5.2 Enhanced tunneling through square barrier

As a simplest case, we chose to analyze transmission of a wavepacket through a single square barrier in the presence of an oscillating voltage. An illustration of the geometry is shown in the inset of Fig. 2-5. The oscillating voltage was split symmetrically between the left and right side of the barrier,

$$V_{\rm ac}(x,t) = \begin{cases} V_1(x/2|x|)\theta(|x| - d/2)\cos\omega t & |x| > d/2 \\ V_1(x/d)\cos\omega t & |x| \leq d/2 \end{cases}, \tag{2.17}$$

where eV_1 is the maximum ac excursion of the contact potentials, d is the total barrier length and $\theta(x)$ is the unit step function. For this ac potential the ac electric field is entirely confined within the barrier region, $-d/2 \leq x \leq d/2$. In the simulation run we set the dc barrier height to $V_0 = 50$ meV and the mean energy of the incident electron wavepacket to $E_0 = 10$ meV. The length of the barrier was $0.3\lambda_0 \approx 47$ nm.

The result of the simulation is shown in Fig. 2-5. The Fourier components of the transmitted wavepacket are plotted as a function of the wavevector k_x. In the simulation run, a propagation time of 12 ps beyond interaction of the wavepacket with the square barrier was used. This proved sufficient for the probability density of the transmitted and reflected wavepacket to add to unity. The plot shows curves for both $\alpha = 0$ (dashed line) and $\alpha = 0.25$ (solid line). For the second case, when the ac potential is non-zero, a broadening of the spectrum and the development of several peaks on both sides of the initial wavevector is seen. This additional structure is evidence of the formation of sidebands. In Fig. 2-6 the value of each wavevector corresponding to a sideband peak is plotted along the abscissa; and the energy for that wavevector, using a parabolic energy dispersion, is plotted along the ordinate. We find that the vertical separation in energy between the data point is equal to an integer multiple of the modulation quanta $\hbar\omega$. Hence, the sidebands are due to

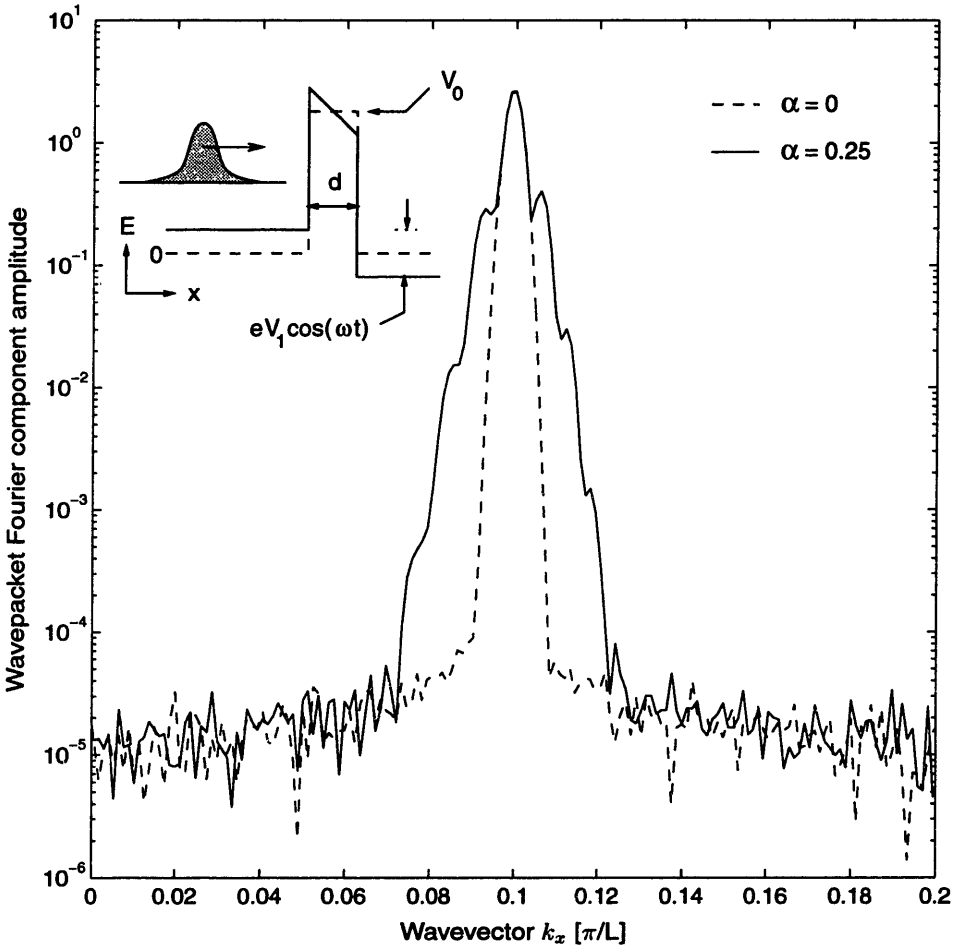

Figure 2-5: Result in Fourier space of a wavepacket propagating through a time-oscillating potential barrier. Inset shows definition of barrier dimensions. Parameters used are: $E_0 = 10$ meV, $V_0 = 50$ meV, $f = 300$ GHz, $d = 0.3\lambda_0$, $\alpha = 0$ or 0.25, and $L = 2.35$ nm.

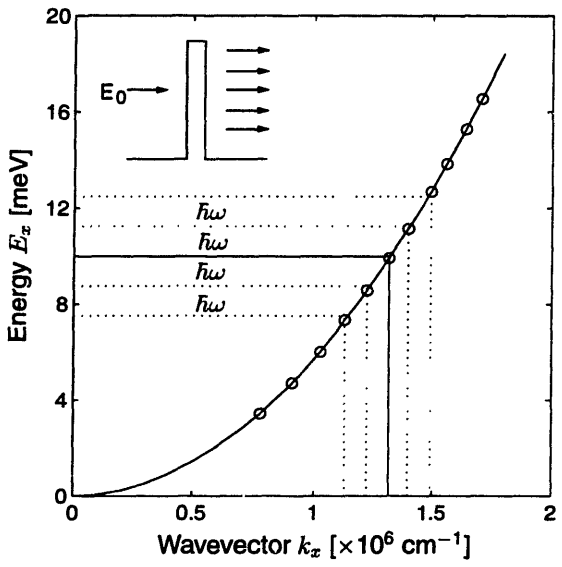

Figure 2-6: Electron wavepacket dispersion curve after being transmitted through the sinusoidally oscillating square barrier (circles). Solid line shows the parabolic energy dispersion. Each data point is vertically separated by units of integer multiples of the modulation quanta $\hbar\omega$. Parameters used are: $E_0 = 10$ meV, $V_0 = 50$ meV, $f = 300$ GHz, $d = 0.3\lambda_0$ and $\alpha = 1$.

absorption and emission of modulation quanta $\hbar\omega$ by the wavepacket while traversing the square barrier.

We next investigated the amplitude variation of the Fourier components for each sideband as a function of the parameter α, as shown in Fig. 2-7. The simulation result for the lowest four absorption and emission sidebands is shown (circles). The absolute value of the n-th order Bessel function, $J_n(\alpha)$, is also shown for $n = 0, \pm1, \ldots, \pm4$ (dashed line). Comparison to the Bessel function is motivated by the results we obtained in section 2.2 for the amplitude of the sidebands. A striking resemblance to the behavior of the simulation data is seen, although the height only matches in case of the the center component. The ratio of each Fourier component amplitude, $FC_n(\alpha)$, and the corresponding Bessel function, $|J_n(\alpha)|$, is shown in Fig. 2-8. Each data point was evaluated by averaging the ratios obtained for all values α's as long as $FC_n(\alpha) > 0.25$. Values smaller than 0.25 have been neglected because of the large uncertainties associated with extracting the peak heights from the spectrum. For comparison, we have plotted the ratio $T(E_0 + n\hbar\omega)/T(E_0)$ of the analytical

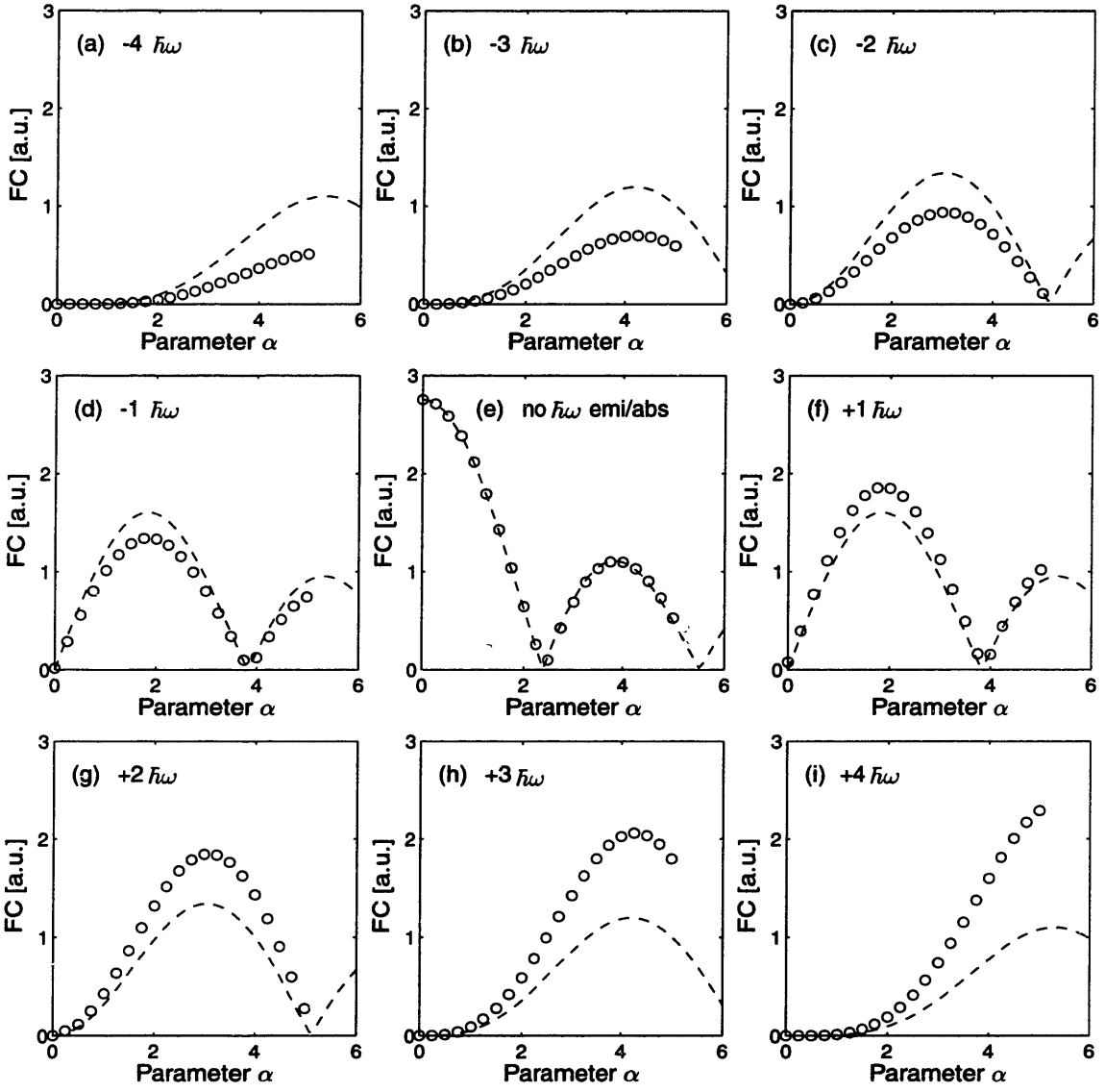

Figure 2-7: Simulation result of Gaussian wavepacket propagation through a time-oscillating square barrier (circles). The Fourier component amplitudes for sidebands n=0,±1,±2,±3 and ±4 are plotted versus the α parameter. (a) through (d) are the modulation quanta emission sidebands, (e) is the center band, while (f) through (i) are the modulation quanta absorption sidebands. Parameters used are: $E_0 = 10$ meV, $V_0 = 50$ meV, $d = 0.3\lambda_0$, and $f = 300$ GHz. The magnitude of the Bessel functions $J_n(\alpha)$ (dashed lines) are scaled by a common factor determined from matching $J_0(0)$ to the amplitude of the Fourier component in (e) for $\alpha = 0$ from the simulation.

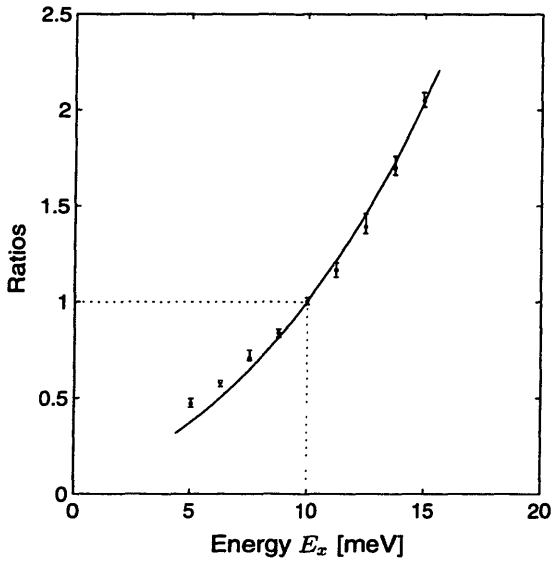

Figure 2-8: Discrete points show ratio $FC_n(\alpha)/|J_n(\alpha)|$, amplitude of Fourier component divided by absolute value of Bessel function. Value of ratio for each value of n is averaged over all α's. The errorbars show the standard deviation at each value of n. The energy dependence of the transmission coefficient is depicted by the ratio $T(E_0 + n\hbar\omega)/T(E_0)$ (solid line). Parameters used are: $E_0 = 10$ meV, $V_0 = 50$ meV, $f = 300$ GHz, $d = 0.3\lambda_0$.

transmission coefficient through the square barrier when $\alpha = 0$

$$T(E_x) = \frac{1}{1 + V_0^2 \sinh^2 \kappa d / 4E_x(V_0 - E_x)}, \tag{2.18}$$

where $\kappa^2 = 2m^*(V_0 - E_x)/\hbar^2$ (solid line in Fig. 2-8). Deviations between the ratios are seen for $n = -2, -3$ and -4. Such deviations are most probably caused by uncertainties introduced when extracting the Fourier component amplitudes for these sidebands, since no well-defined sideband peaks develop, see Fig. 2-5. No peak occurs in the spectrum for these sidebands since the transmission probabilities for the square barrier rapidly decreases as E_x decreases. The increased overlap between adjacent sidebands results in an overestimation of the Fourier component amplitude, and hence too large a value for the ratio. Apart from this discrepancy, the values for the two ratios compare well. We conclude that the transmission coefficient through an sinusoidally oscillating square barrier characterized by Eq. 2.17 can be written as follows

$$T_\omega(E_x) = \sum_n J_n^2(\alpha) T(E_x + n\hbar\omega). \tag{2.19}$$

This altered transmission coefficient in the presence of a radiation field will be referred to as the modified transmission coefficient [32, 23].

2.5.3 Enhanced over-the-barrier transport

In this section we study the radiation-enhanced transport for a single barrier potential when the height of the barrier is reduced to such an extent that absorption of a single modulation quanta $\hbar\omega$ by an electron will result in over-the-barrier transport. Further, we introduce a finite width ac potential profile.

Following the example of Yakubo *et al.* [29], we chose an identical model for the ac voltage profile

$$V_{\rm ac}(t) = \frac{V_1}{2} \tanh\left(\frac{x - x_c}{\xi_{\rm ac}}\right) \cos\omega t, \tag{2.20}$$

where $2\xi_{\rm ac}$ is used to describe the characteristic length of the ac electric field confinement. The electric field in this model reaches a maximum at the center of the structure, x_c, and decreases rapidly to zero at a distance on the order of a few $\xi_{\rm ac}$ on either side the barrier region. Using this model for the ac voltage allows adjustment of the ac electric field confinement. Investigation of how the efficiency of modulation quanta absorption by ballistic electrons depends on the ac electric field confinement is important. In superconducting-insulator-superconducting tunnel junctions, where the the electric field is localized within the insulator region and extends about a London penetration depth into the superconductor. In contrast, for quantum-effect devices, where the 2DEG has a relatively long screening length, the ac electric field extends beyond the dc potential profile. Additional confinement of the ac electric field might be achieved by reducing the separation between the antenna terminals. We are therefore going study the dependence of the Fourier components FC_n as the confinement parameter $\xi_{\rm ac}$ is varied.

The results of the simulation run are shown in Fig. 2-9. In the simulation we

kept the radiation frequency fixed at 300 GHz, the electron injection energy was $E_0 = 10$ meV and the dc barrier height (described by Gaussian profile) was equal to $V_0 = E_0 + 4\hbar\omega/5$. The Fourier component FC_n of the transmitted wavepacket for the center and the two sidebands corresponding to absorption of $\hbar\omega$ and $2\hbar\omega$ are shown ($n = 0, 1$ and 2) as a function of the ac confinement ξ_{ac}. In the simulation the α parameter was set to 1. The three solid curves show the effect on the spectrum when the FWHM of the Gaussian dc potential barrier is 140 nm. For a very strongly confined ac electric field, $2\xi_{ac} < 100$ nm, we find that the FC_1 exceeds the FC_0 component, and consequently, the radiation-induced current should exceed the dark current. When the width of the dc potential barrier is decreased to 60 nm, the amplitude of the absorption sidebands decreases strongly (dashed curve). In fact, they are only slightly larger than the sidebands obtained without any dc barrier (dotted curves). Without a barrier, phase-matching between the incident wavepacket and the excited plane wave at energy $E_0 + n\hbar\omega$ becomes essential [29]. From this simulation run we learn that strong coupling between the incident wavepacket and an over-the-barrier propagating state is obtained for the case of a strong ac electric confinement, on the order of the dc barrier FWHM; and the dc barrier must have a sufficient length. If we consider the two barriers used in the simulation, the length of the classically forbidden region for the 60 nm and 140 nm barriers are 22 nm and 52 nm, respectively. The traversal times through the barriers at 10 meV are 0.48 ps and 1.37 ps [23]. These traversal times result in interaction times of $\omega\tau = 0.91$ and 2.57, respectively. For $2\xi_{rmac} = 50$ nm we get $\alpha = 0.41$, and 0.78 for the two cases. The transitions therefore favor a condition with $\omega\tau > 1$ and $\alpha > 1$.

In Fig. 2-10(a) we have replotted the result of the previous simulation but we display the difference in the amplitude of the Fourier component due to the radiation field which is the result of the photonic effect. The FWHM of the Gaussian dc

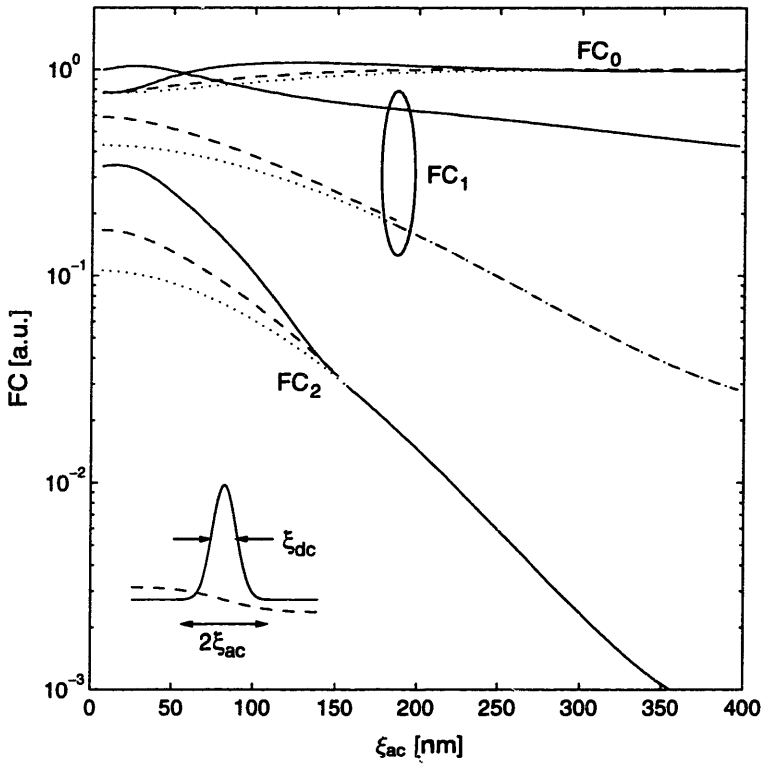

Figure 2-9: Simulation result showing magnitude of Fourier components FC_n as a function of the ac potential confinement ξ_{ac}. The FWHM of the dc Gaussian potential barrier is $\xi_{dc} = 140$ nm (solid line) and 60 nm (dashed line). For comparison, we also show Fourier components for absorption in case of no dc barrier (dotted line). Parameters used are: $E_0 = 10$ meV, $V_0 = E_0 + 4\hbar\omega/5$, $\alpha = 1$ and $f = 300$ GHz.

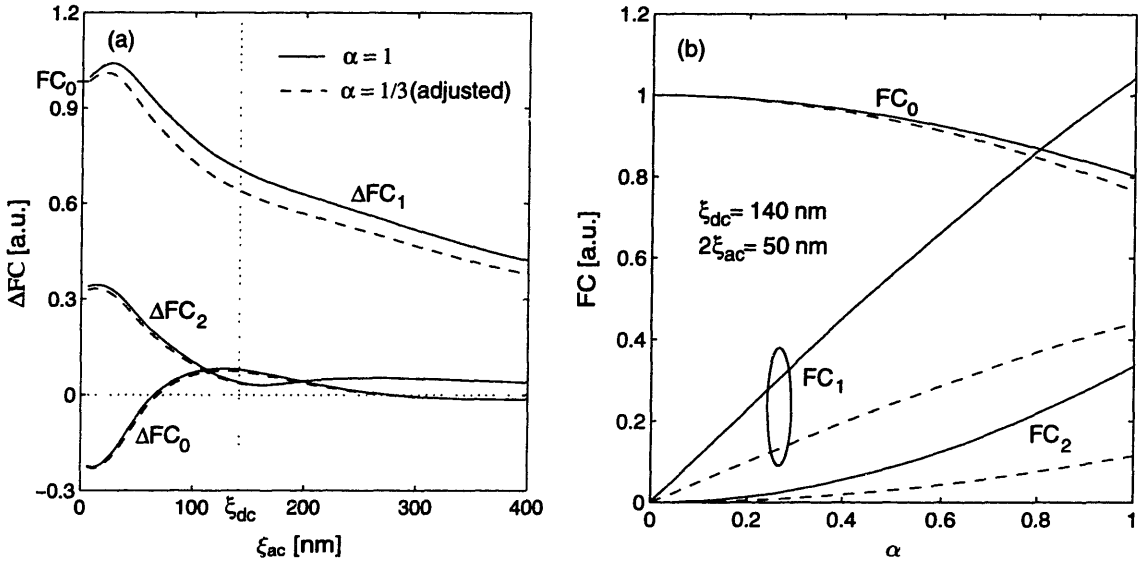

Figure 2-10: (a) Simulation result for dc Gaussian potential barrier with FWHM of 140 nm. The change of the Fourier components, ΔFC_n, is plotted versus the ac potential confinement ξ_{ac}. The calculations are done for $\alpha = 1$ (solid lines) and $\alpha = 1/3$ (dashed lines). The latter set of three curves has been appropriately scaled to compare to the $\alpha = 1$ case. (b) The Fourier components FC_n are plotted as a function of α for $\xi_{dc} = 140$ nm and $2\xi_{ac} = 50$ nm (solid lines). For comparison, we also show the value of the Bessel functions $J_n(\alpha)$ (dashed lines). Parameters used are: $E_0 = 10$ meV, $V_0 = E_0 + 4\hbar\omega/5$ and $f = 300$ GHz.

potential is 140 nm. It is evident that only the first absorption sideband gains significantly in amplitude as the ac electric field confinement is increased. The change of the FC_0 and the FC_2 almost offset each other. We therefore expect a large increase in the current due to radiation-induced over-the-barrier transport. For comparison, we show simulation results for both $\alpha = 1$ and $\alpha = 1/3$. The latter has been adjusted appropriately for comparison. Since the two curves match each other well, the effect of barrier distortion when using a larger value for α is minimal.

In order to compare this result to the prediction based on Eq. 2.19 we have calculated the amplitude of the Fourier component as a function of α, as shown in Fig. 2-10(b). The zeroth Fourier component does indeed follow $J_0(\alpha)$ and an excess

amplitude is observed for both FC_1 and FC_2. This excess amplitude is encouraging, because the transmission coefficient for over-the-barrier transport is significantly larger than at the incident electron energy. In the simulation result FC_1 is not much larger than FC_0 for $\alpha = 1$. This is caused by the relatively large dark current for the zeroth component since the equivalent wavepacket temperature is $T_\psi \approx 2$ K. In the experiment, a temperature of 0.5 K can be achieved, thus the dark current is expected to be significantly reduced.

The process we have studied in this section is schematically illustrated in Fig. 2-11. We have divided the region into three domains. In domain I and III the electrons propagate as plane waves and no transition can occur them. In domain II the electron wavefunction incident at energy E_0 enters a classically forbidden region at x_1. Transition can efficiently occur between this decaying wavefunction and a propagating state at $E_0 + \hbar\omega$. In the schematic we only show the propagating wavepacket. Of course to satisfy all boundary conditions, wavepackets will both be transmitted through and reflected from the structure. We found that for a sufficiently confined ac electric field ($\alpha > 1$), we expect that absorption of modulation quanta by the incident ballistic electron is possible while it is evanescently decaying into the barrier. A tight confinement of the ac electric field would also reduce the amount of heating of the electrons in the 2DEG. In addition, a sufficiently long interaction time was required of the wavepacket with the barrier to absorb modulation quanta from the oscillating potential ($\omega\tau > 1$). We have also found that the absorption within the classically forbidden region and from an evanescently decaying wavefunction to a propagating state dominated; excitations taking place between two plane waves in the presence of a confined ac electric field is found to be inefficient when compared to the previous two processes.

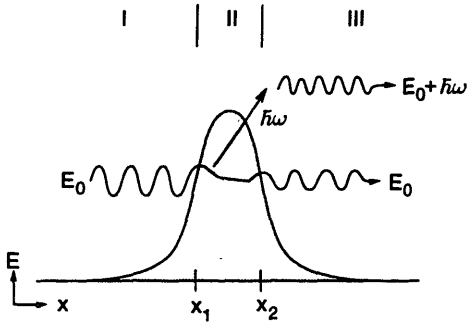

Figure 2-11: Schematic illustration of modulation quanta $\hbar\omega$ absorption at the front edge of the potential barrier.

2.5.4 Enhanced transport through double barrier

As the third example, we simulated a symmetric double barrier potential. In the simulation we have chosen dimensions which correspond closely to our devices. Yakubo *et al.* [29] has simulated similar double barrier structures, but he uses smaller dimensions and a different potential profile description. The transmission coefficient for 50 nm long gates separated by 130 nm with an applied voltage of -0.725 V is shown in Fig. 2-12(a). We chose a wavepacket with a center energy of 10 meV and 10.5 meV. According to Eq. 2.19, we expected to observe an enhanced transmission for radiation frequencies at 340 GHz and 220 GHz, respectively. We chose to model the ac potential profile using Eq. 2.20. In the simulation we set $2\xi_{ac} = 400$ nm, which was slightly larger than the spatial extent of the potential profile for the double barrier.

Figure 2-12(b) shows the simulation result of total transmission $T_\omega(E_0)$ for $E_0 =$ 10 meV and 10.5 meV. The simulation was performed keeping the α parameter constant to one. The frequency was varied from dc to 600 GHz. Enhanced transmission is observed at frequencies approximately equal to the energy difference between resonant level and initial wavepacket injection energy. We interpret this behavior as absorption of a modulation quanta $\hbar\omega$ from the oscillating potential barriers. However, we observed two discrepancies from the ideal model description, Eqn. 2.19. The first was the shift of the peak position in $T_\omega(E_0)$, predicting a larger difference between the electron initial energy and the resonant level. The reason for this shift originated

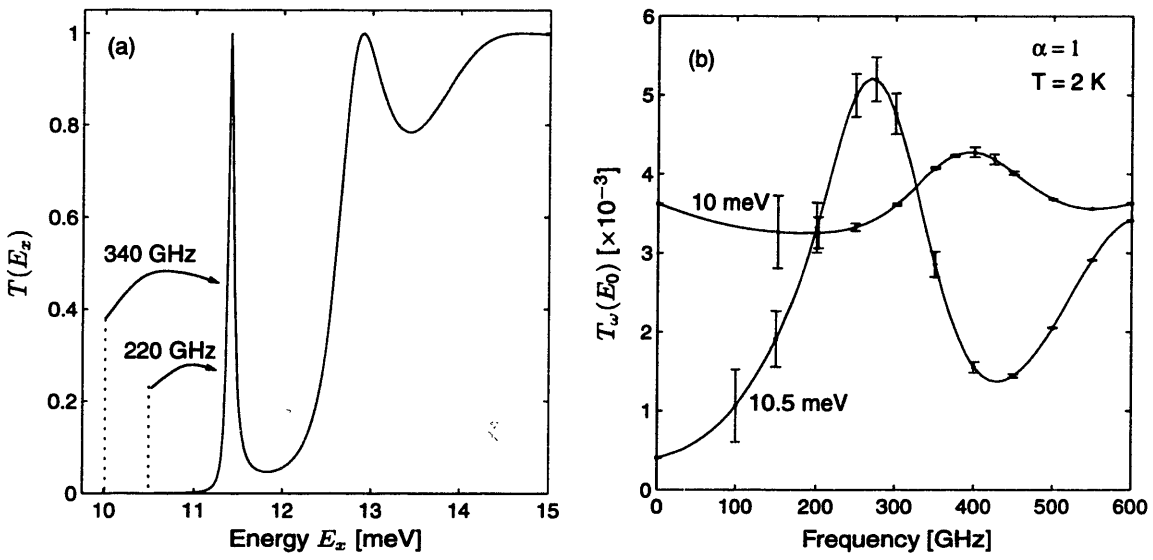

Figure 2-12: (a) Transmission coefficient $T(E_x)$ of dual barrier structure as a function of electron injection energy E_x. Length of both gates is 50 nm and the separation is 130 nm. The voltage applied to both gates was -0.725 V. (b) Simulation result for a time-oscillating dual barrier. The modified transmission coefficient, $T_\omega(E_0)$, is plotted as a function of frequency for $E_0 = 10$ meV and 10.5 meV. Enhanced transmission is observed at a frequencies corresponding approximately to the energy difference between the resonant level and the initial wavepacket injection energy. Each data point is the mean of eight simulation runs. In each run, the initial phase ϕ of the ac potential was incremented by $\pi/4$. The error bars indicate the standard deviation of the set of eight data points these runs.

in the method used for calculating the dc transmission coefficient $T(E_x)$. The TMM predicted a slightly lower position of the peak transmission resonance, about 50 GHz, when compared to the position that occured when we used a propagating wavepacket approach. We attribute this to the asymmetry with respect to the energy of the transmission coefficient close to the top of the barrier, see Fig. 2-4. Since the wavepacket senses the transmission coefficient for an interval of energies, a shift upward in energy is expected. The second discrepancy relates to the general shape of $T_\omega(E_0)$. For the two injection energies we have analyzed, $T_\omega(E_0)$ was expected to appear the same, but shifted upward in frequency by 120 GHz. We found that the undulations in the curve for $E_0 = 10.5$ meV are larger and the transmission peak is narrower. We propose the following mechanism is at work: for a constant value of α, the voltage V_1 increases linearly with the angular frequency ω. Such an increase in the amplitude of the ac modulation leads to an increase in the distortion of the dc potential profile, and consequently to the destruction of the resonant levels. Other mechanisms that also contribute to the broadening of the transmission resonance level are the finite width of the incident wavepacket, and the enhanced coupling of the resonant state to the outside via escape through the absorption and the emission sidebands.

2.6 Summary

This chapter has dealt with the theoretical aspects of radiation-enhanced transport of ballistic electrons through a quantum effect device. We have found that when the radiation field induces a sinusoidally varying ac voltage in the contacts of the device the density of states is split into sidebands. We have then presented a simple model for the potential profile for a device, and calculated the transmission coefficient through the structure using TMM.

The influence of a radiation field on the electron transport through both a single

and a double barrier potential was then studied. The radiation field was described as a sinusoidally oscillating voltage across the barrier region, much like in our initial approach in which we focussed on the difference in the electrochemical potentials deep inside the contact regions. In this model, the electrons entering the active region of the device are assumed to retain their phase coherence while traversing the potential barrier. We found that if this condition is satisfied, the transmission through a potential profile for a sufficiently confined electric field can be approximately described using a modified transmission coefficient. This modified transmission coefficient agrees well with the simulation results for tunneling through a single square barrier potential. For over-the-barrier transport the Bessel behavior of the sidebands remains valid, except that the full value of the transmission coefficient is not gained. For the double barrier potential, deviations from this ideal behavior were observed. In part, we attributed these deviations to potential profile distortions caused by the large ac voltages. We conclude that the modified transmission coefficient description provides a convenient method to describe the effects of a radiation field on the ballistic transport through mesoscopic structures.

Chapter 3

Device design, fabrication and measurement

3.1 Introduction

This chapter covers device design, fabrication technology and experimental apparatus. Section 3.2 outlines four design objectives which resulted from the theoretical treatment in chapter 2. One section is then devoted to each of the following topics: (1) the details of the AlGaAs/GaAs heterostructure are discussed in section 3.3; (2) the properties of the planar antennas which are used to couple the radiation into the sub-micron sized devices are reviewed in section 3.4; (3) the mask layout, the device fabrication, and the test structures (incorporated for material characterization and process monitoring) are presented in section 3.5; and (4) the measurement system is discussed in section 3.6.

3.2 Device design objectives

The design of the quantum-effect devices required that we address the following four issues:

- Observation of the quantum limited detection process necessitates phase-coherent transport of the electrons between the drain and the source contacts. Therefore, high electron mobility material and a sufficiently small device structure were used.

- Tight confinement of the ac voltage produced by the radiation field is needed to observe the desired radiation-induced processes in QPCs and dual gate devices. The fabrication of the radiation focussing antenna had to be integrated with the lithographic process.

- Fabrication of quantum point contacts and dual gate devices requires the use of sub-micron fabrication techniques.

- Broad-band optics and antennas must be used so that the radiation coupling efficiency to the device remains constant throughout the frequency band of interest.

3.3 AlGaAs/GaAs heterostructure

The quantum effect devices in this thesis have been fabricated using molecular-beam epitaxy (MBE) grown modulation-doped AlGaAs/GaAs heterostructures. High mobilities are achieved in these material systems, commonly on the order of 10^6 cm^2/V·s at liquid helium temperatures, making it possible to observe quantized transport phenomena in sub-micron sized devices [20].

The two-dimensional electron gas (2DEG) has been located at different depths to find the best balance between mobility in the 2DEG and sharpness of the gate-induced confining electrostatic potential. For the quantum point contact (QPC), the 2DEG was located at a depth of 83 nm below the substrate surface [38]. For the dual gate device, this depth was reduced to a dimension comparable to or smaller than the gate length. The minimum gate length fabricated, using an electron-beam lithography process, was 50 nm. As shown by the potential profile calculations in chapter 2, little is gained by growing an MBE film with a 2DEG depth much shallower than 50 nm. Achieving high electron mobilities in such shallow structures is intrinsically difficult for the following reasons: (1) a decrease in the spacer thickness increases the overlap between the wavefunction describing the extent of the vertically confined 2DEG and the donor atoms. This leads to an increase in the 2DEG scattering rate and reduces the mobility; (2) when the Si-dopant monolayer is positioned closer to the surface, a larger fraction of the donor electrons are captured by surface states. This loss of donor electrons can be compensated partially by increasing the dopant density to a certain extent, as long as the creation of a parallel conducting channel in the AlGaAs is avoided. If such a secondary channel forms, the MBE layer is rendered unusable for the fabrication of quantum-effect devices. Also, placing donor atoms close to the surface results in a larger variability in device characteristics, such as the pinch-off voltage, since the carrier density in the 2D channel is more strongly dependent on surface conditions. Because of these difficulties associated with realizing shallow and high-mobility 2DEGs, a series of MBE films were grown by collaborators [39]. The thickness of the AlGaAs top and spacer layer were gradually decreased; an effort that produced several shallow 2DEG structures with sufficient mobilities for quantum devices.

A typical shallow AlGaAs/GaAs heterostructure is shown in Fig. 3-1. The layers,

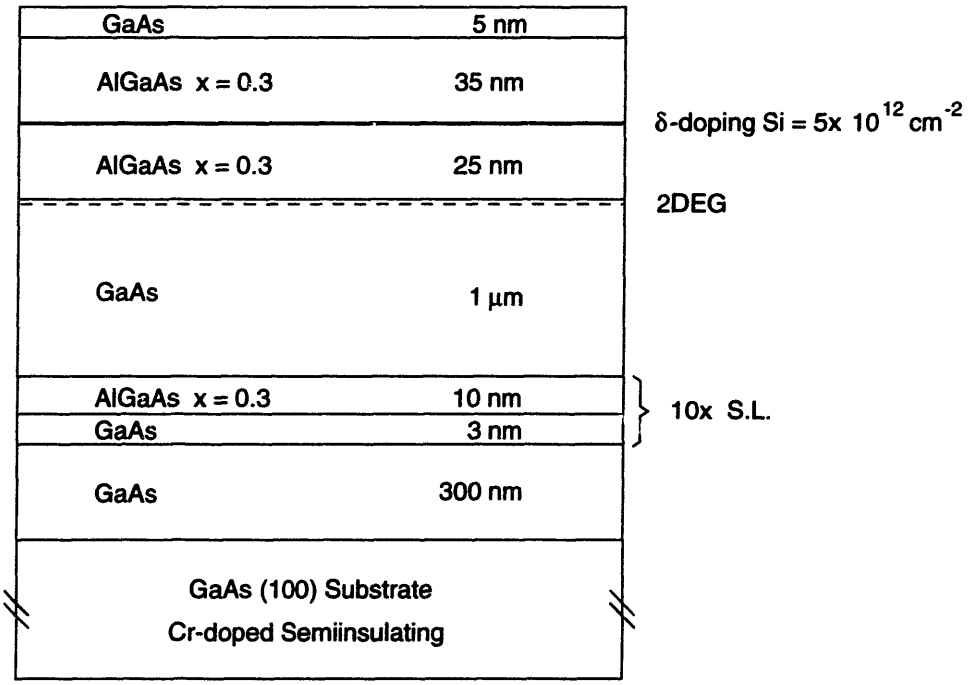

Figure 3-1: MBE film 6081 with shallow 2DEG grown by A. Förster at KFA Jülich in November 1993.

from top to bottom, are a 5 nm undoped GaAs cap, a 35 nm undoped $Al_{0.3}Ga_{0.7}As$ top layer, a Si monolayer with an area density of 5×10^{12} cm^{-2}, a 25 nm undoped $Al_{0.3}Ga_{0.7}As$ spacer, a 1 μm undoped GaAs layer, a 10 times repeated superlattice of 10 nm $Al_{0.3}Ga_{0.7}As$ and 3 nm GaAs, and a 300 nm GaAs buffer layer on top of a semi-insulating GaAs substrate. The AlGaAs/GaAs superlattice is initially grown to reduce the number of oval defects in the finished epitaxial film. The depth of the 2DEG for this sample was 65 nm, measured from the substrate surface, and the carrier density was 3.8×10^{11} cm^{-2}. This means that only a small fraction of the electrons from the donor atoms diffuse to the channel, about 8% [40]. For very shallow heterostructures this fraction decreases further to only 3%. The remainder of the electrons are frozen out or captured by DX-centers in the AlGaAs [41] and surface/interface states. This low yield becomes particularly serious for very shallow 2DEG structures. For the shallowest structure tested, which had a 2DEG depth of 40 nm (wafer 6128), only 3% of the electrons diffused to the heterointerface. This variability in yield makes it difficult to determine the proper doping density in advance. When a 2DEG's carrier density is too small, the effectiveness of charge screening is reduced, resulting in a lower mobility. Excessive doping populates the second subband at the heterointerface, again causing an increase in the scattering rate. Often, for high doping concentration, a parallel conduction channel also forms in the AlGaAs layer with a much reduced mobility. This large variability forced an incremental decrease of the thickness of the two AlGaAs layers.

Table 3.1 shows the dimensions of the MBE films and their transport characteristics. The GaAs cap layer for all the films was 5 nm. The doping of the first two samples, m22 and 6034, was achieved using 13 Si monolayers uniformly separated by 5 nm of AlGaAs in the top AlGaAs layer. These two substrates were used for the fabrication of QPCs. The doping in the remainder of the samples was accomplished

Table 3.1: Summary of MBE layers.

Wafer #	Doping [10^{12} cm^{-2}]	Depth [nm]	Spacer [nm]	Density [$\times 10^{11}$ cm^{-2}]	Mobility [$\times 10^4$ cm^2/V·s]
m22		83	20	2.8[a]	20.0[a]
6034		83	20	2.4[b]	13.2[b]
6081	5	65	35	3.8	16.5
6082	5	65	25	3.7	17.3
6167	7	55	25		
6122		55	25	3.6	17.8
6133		50	25	3.8	13.5
6123	8	45	20	4.5	17.1
6128	13	40	20	4.4	16.2

Measurements done at [a]45 K, [b]4.2 K and the remaining at 77 K. Sample m22 was grown by Professor M. Melloch and coworkers at Purdue University [42]. Sample 6034 was grown by Dr. J. Smet while working in the MBE group of Professor C. Fonstad at MIT. All shallow 2DEG samples were grown by Dr. A. Förster at ISI Forschungszentrum GmbH, Jülich, Germany.

using a single Si monolayer located between the two AlGaAs layers, similar to the structure shown in Fig. 3-1. The distance between the 2DEG and the surface was decreased by reducing the thickness of both the top and spacer AlGaAs layers. As the Si monolayer is brought closer to the surface, more donor electrons are captured by the surface states. The doping concentration was therefore increased to insure sufficient population of the 2DEG. For sample 6128, the mobility at 4.2 K (in the dark) was 0.93×10^6 cm^2/V·s with a carrier density of 4.25×10^{11} cm^{-2}. SdH-measurements showed that a parallel conducting channel was present in this film [40]. This sample was therefore not used for device fabrication. The mobility of the remaining samples was also expected to be close to 10^6 cm^2/V·s at 4.2 K.

3.4 Radiation coupling

Measurement of the photoconductive response of an individual quantum effect device at millimeter and submillimeter wavelengths requires a radiation focussing method which is precisely aligned with the device's gate structure. A quasi-optical system consisting of multiple lenses is used to guide the radiation towards the substrate. Additional focussing is then achieved using a planar antenna [43]. Without the use of such an antenna, almost no radiation would be coupled into the device, since the free space wavelength of the radiation is on the order of mm's, and the dimensions of the device's active region is typically a few μm's. When coupling the radiation into a device, a planar antenna is easier to fabricate than waveguide structures. In particuler, waveguide structures are increasingly difficult to make for wavelengths far below 1 mm. The fabrication of an integrated antenna in our process, however, can be accomplished without even introducing an additional mask level. Integration of the antennas into the standard fabrication process also assures precise alignment to the mesoscopic system.

Since the interesting frequency range for the radiation experiments of the quantum effect devices we intended to study was not known, we decided to use planar antennas with a self-complementary geometry. These antennas offer an essentially frequency independent response throughout a wide frequency band that is ideal when performing spectroscopy [44]. Specifically, the impedance of such antennas mounted on a dielectric substrate is given by

$$R_a = \frac{Z_0}{2\sqrt{(\varepsilon_r + 1)/2}}$$

where $Z_0 = (\mu_0/\varepsilon_0)^{1/2} = 377\ \Omega$ is the free space impedance [45]. For GaAs, with a dielectric contant of $\varepsilon_r = 12.5$, the antenna impedance is $R_a = 72.5\ \Omega$, purely resistive

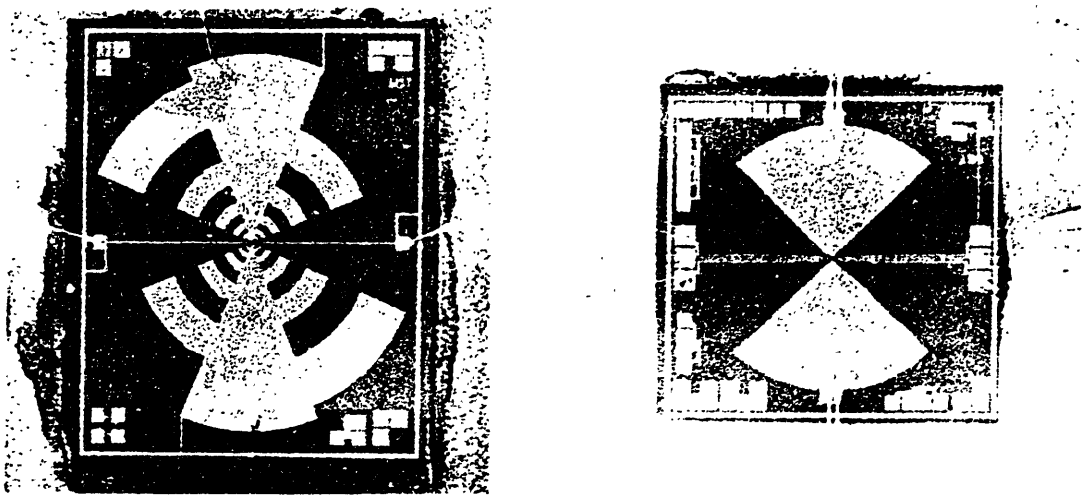

Figure 3-2: Photographs of the two self-complementary antennas; a log-periodic antenna on the left and a bow-tie antenna on the right.

and independent of frequency.

Photographs of the two self-complementary antenna geometries which we used, the log-periodic antenna and the bow-tie antenna, are shown in Fig. 3-2. For the log-periodic antenna, each of the eight sectors subtend an arc of 45° degrees with a ratio of $\tau = 0.5$ for the radii of consecutive teeth. This choice for the angles assures that both antennas are self-complimentary. For the bow-tie antenna, the metal subtends an arc of 90°. A measurement of the antenna pattern for a log-periodic antenna with such narrow teeth, $\tau = 0.5$, on a dielectric substrate with $\varepsilon_r = 4$, showed a 3 dB suppression of the sidelobes at 18° [46]. Figure 3-3 shows the measured antenna beam pattern for a scale model bow-tie antenna on a dielectric surface with $\varepsilon_r = 4$ [47]. The relatively wide antenna beam pattern of a bow-tie antenna is evident in the graph, showing a large sidelobe at 30° degrees. Since the dielectric constant of GaAs is even larger, the difference between the air side and the dielectric side coupling efficiency is even more dramatic. In order to capture the wide antenna beam pattern, we must use

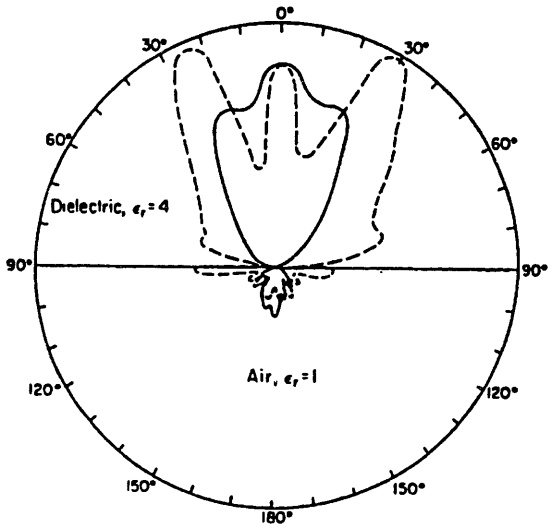

Figure 3-3: Measured bow-tie antenna beam pattern for a 10-GHz model with $\varepsilon = 4$: E-plane (dashed curve) and H-plane (solid curve) [47].

a low /F-number quasi-optical system, the design of which is discussed in section 3.6.

Since the dominant fraction of the antenna beam pattern is directed into the dielectric, it is advantageous for the radiation to reach the device through the GaAs substrate. This requires the use of a semi-insulating GaAs substrate to minimize free carrier absorption. The transmission spectrum of a blank GaAs substrate at room temperature was measured to be 60% (see Fig. 3-4). The periodic peaks, spaced apart by approximately 80 GHz, are caused by standing wave patterns in the GaAs substrate. Such peaks in the transmission spectra are expected every time an integral number of half wavelengths matches the sample thickness ($\sim$500 μm). We expected the measured value of the transmission to increase at 4.2 K, since the free carriers are frozen out.

For bow-tie antennas, the bow-arm length can typically be terminated at twice the longest radiation wavelength (measured in the dielectric) of interest [45]. If the outermost area of the antenna is then used for dc connection, the antenna radiation

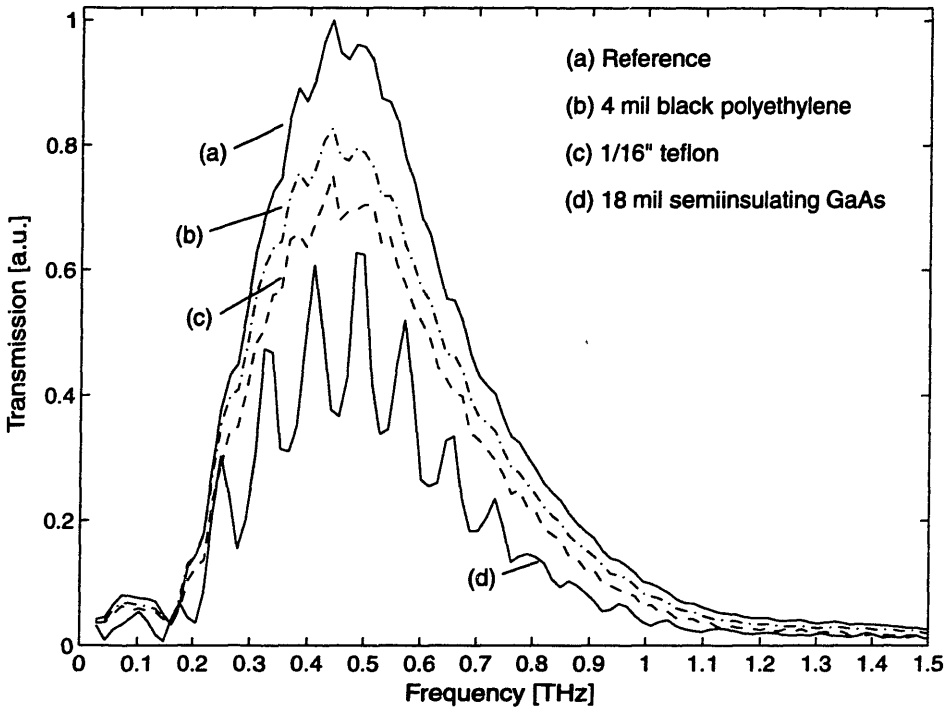

Figure 3-4: Transmission spectra of semi-insulating GaAs substrate measured at room temperature. For comparison, measurements of black polyethylene and a teflon are shown. The spectra are measured using a Fourier transform spectrometer with an InSb bolometer cooled to 4.2 K.

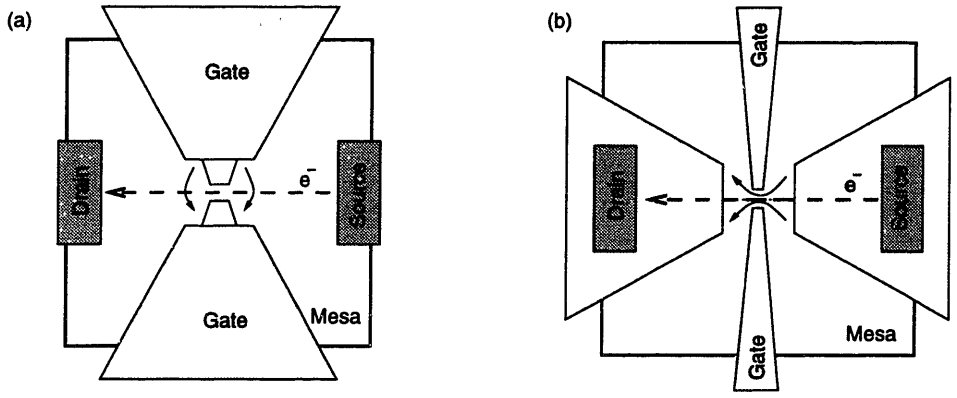

Figure 3-5: Illustration of two possible orientations for the antenna. In (a) the ac voltage produced by the antenna is coupled to the 2DEG transverse to the direction of charge transport, while in (b) it is coupled along the transport direction.

pattern and impedance are not affected. For a frequency of 60 GHz the free-space wavelength λ is 5 mm, and the arm length of the bow-tie antenna is

$$h = 2\lambda_\varepsilon = \frac{2\lambda}{\sqrt{(\varepsilon_r + 1)/2}} \approx 3.8 \text{ mm},$$

where $\varepsilon_r = 12.5$ is the dielectric constant for GaAs and λ_ε is the reduced wavelength used for antennas mounted on a half-space dielectric [45]. This length is about half the diagonal of a 5 mm die, which is the dimension we used for mask design. One drawback in using such a large die size is that only a small number of devices can be made: 15 on a quarter of a 2" wafer. An even greater disadvantage is the inability to mount multiple devices during a single cooling cycle. This slows down device testing, since nonidealities, such as charge screening and the effects of impurities or defects in the channel, only become evident at liquid helium temperatures.

Radiation incident on the planar antennas produces an ac electric field between the terminals at the center of the antenna. This electric field is essentially uniform, and is polarized in the direction along the main axis of the planar antenna. Figure 3-5

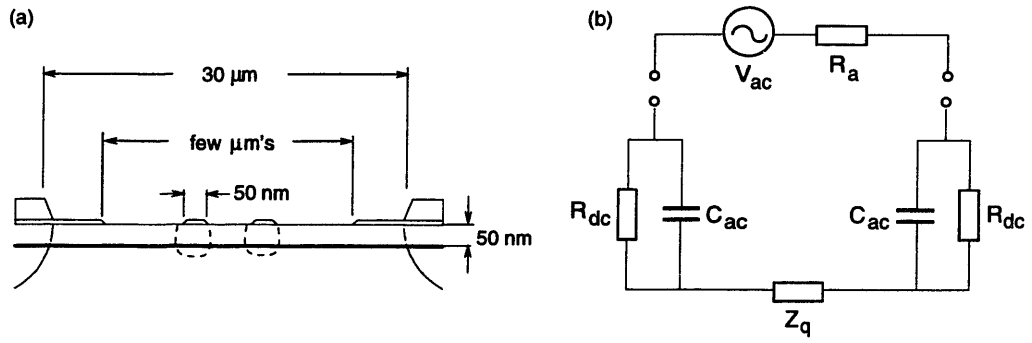

Figure 3-6: (a) Cross-sectional view of antenna terminals and 2DEG. (b) Equivalent rf circuit model for antenna and device.

illustrates how the electric field can be aligned either along (longitudinal coupling) or orthogonal to (transverse coupling) the electron transport direction. In the case of the longitudinal coupling, the antenna serves as a dc connection to the drain and source ohmic contacts. For the transverse coupling, the antenna terminals also define the gate geometry of the quantum-effect devices. This thesis presents measurements of a QPC fabricated with a transverse oriented log-periodic antenna, and a QPC and a lateral dual gate device with a longitudinally oriented bow-tie antenna.

Figure 3-6(a) is a schematic illustration of a dual gate device with a longitudinally oriented planar antenna. The typical antenna terminal separation is a few μm. The ohmic contacts to the drain and source are recessed by 15 μm from the center of the device. The gate length and the 2DEG depth are comparable. In Fig. 3-6(b) an equivalent rf circuit model for the device is shown using lumped circuit elements. The circuit model accounts for the gross behavior of the device - no detailed modeling of the radiation coupling into the 2DEG was attempted. In the circuit model, the radiation field is represented as an ac voltage source of magnitude V_{ac}. The antenna impedance R_a is, as we have showed above, purely real for a self-complementary antenna. The capacitive coupling of the ac field to the 2DEG is represented by by

the capacitance C_{ac}, and the ohmics contact resistance, in series with the 2DEG resistance, is set to R_{dc}. The device's characteristic impedance is Z_q. For our 2DEG structure, the antenna is essentially shorted to the 2DEG at the rf frequencies of interest. The values for the circuit elements Z_q vary as the biasing voltage on the gate of the device changes. If the device is driven into its pinch-off regime, the device's response is purely capacitive. This simplified model, describing the rf response of the quantum-effect devices, is very crude. According to the Drude model the ac conductivity of 2DEG is partially resistive and partially inductive. Also, the screening length of the 2DEG is relatively long compared to the device size [48]. Taking these effects into consideration, the electric field is no longer confined to the barrier region of the device, but spread throughout the length of the 2DEG between the antenna terminals. We investigated the effects of the ac confinement length of the device's response in chapter 2.

3.5 Fabrication

3.5.1 Mask layout

The die dimension on the mask for each device, measuring 5 mm on the side, was fixed by the required antenna size. A major fraction of each die is therefore occupied by the bow-tie antenna, as is evident from the mask design shown in Fig. 3-7. In order to minimize any disturbance to the antenna radiation pattern, no test structures were placed within a bow-arm's length of the center. The mesa is located at the center of the antenna. Six metal lines run horizontally from bonding pads to the center. They are oriented perpendicular to the rf electric field lines to avoid inducing rf currents along the leads. The ohmic contact pads are located on opposite sides of the mesa.

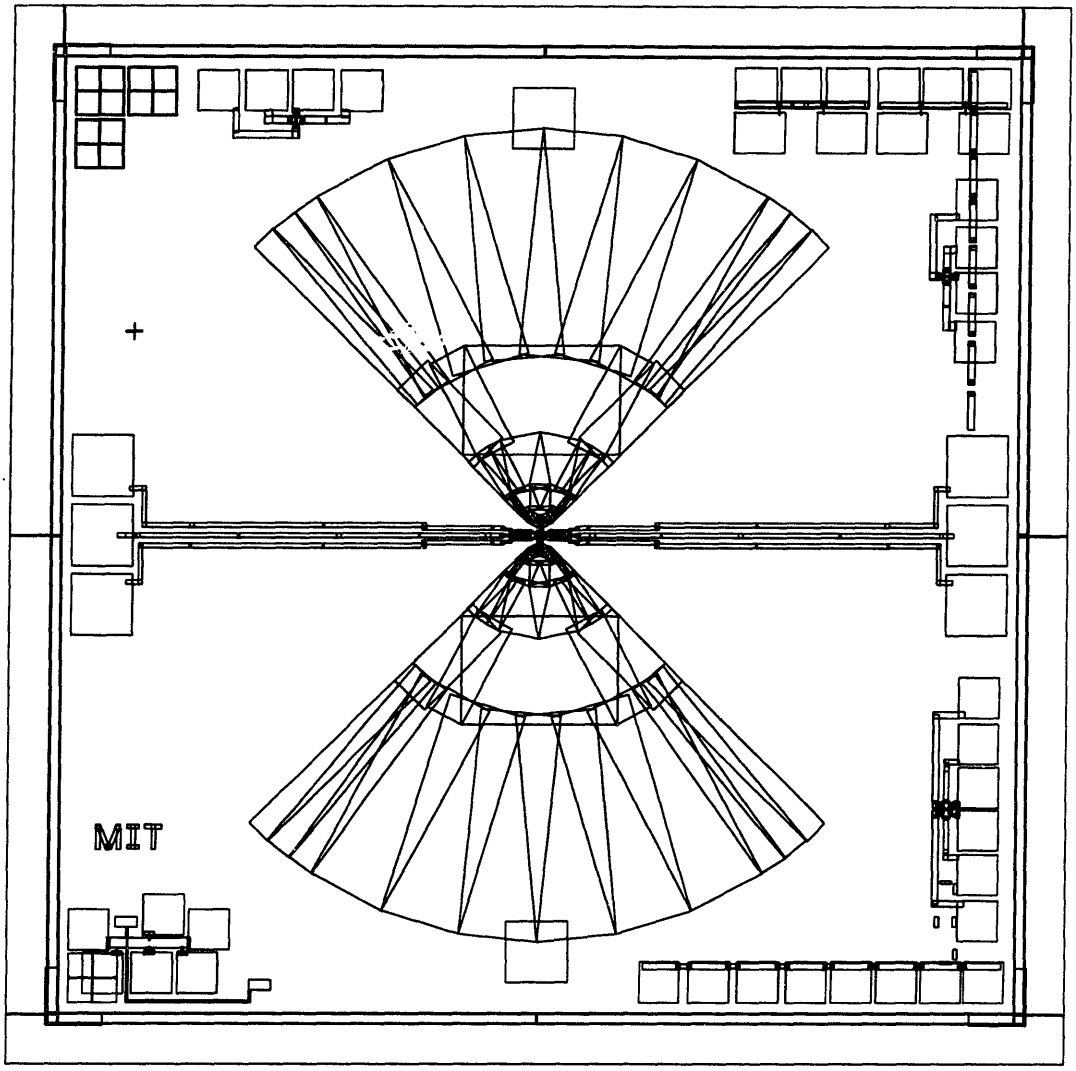

Figure 3-7: Mask drawing for complete die. The quantum effect devices are located at the center of the bowtie antenna.

Table 3.2: Process lithography sequence.

Mesa isolation
Ohmic contacts
First-level metal
Electron-beam lithography
Second-level metal

By rotating the diffusion mask (which defines the ohmic contact pads) 90 degrees, the ohmic contacts can be placed either horizontally or vertically with respect to the ohmic contacts. Therefore, a choice about fabrication of longitudinal or transverse coupled devices can be made during a process run. Apart from the ohmic contacts, the entire mesa is available for device design. Since the fine features of the devices are made using an electron-beam lithography process, which lends itself perfectly to rapid realization of various designs, we were able to fabricate many different designs. The test structures, consisting of a Hall bar, a transmission-line-method (TLM) structure and a 1 μm and 3 μm FET, are all located along the periphery of the layout. The alignment cross for the electron-beam lithography process is in the upper left quadrant of the design. Separate alignment markers are used during the photolithography steps; they are located in the upper left corner of the mask.

3.5.2 Optical and electron-beam lithography

The process flow consists of four photolithography mask levels and one electron-beam lithography step; the sequence has been summarized in Table 3.2. A short account of the optical lithography step for the split-gate process is given in this section; detailed recipes for the fabrication process can be found in appendix B. Figure 3-8 illustrates the process sequence of each fabrication step given in Table 3.2. The wafer used is a modulation-doped $Al_{0.3}Ga_{0.7}As/GaAs$ heterostructure grown by molecular-beam

epitaxy (MBE). In (a) mesa isolation is done by wet chemical etching. The etch is performed to a depth beyond the δ-doped Si layers; (b) deposition of ohmic contact metal consisting of an eutectic composition of Au and Ge. After annealing the sample, an ohmic contact is formed to the 2DEG; (c) Cr/Au deposition for test structures, bonding pads electron-beam alignment cross; (d) Au/Pd deposition of electron-beam lithography defined gate and antenna structures; (e) Cr/Au deposition of antenna, gate leads, and bonding pads; (f) top view of a completed lateral dual gate device with antenna oriented parallel to electron transport direction.

Figure 3-9 shows an expanded view of a quantum dot design using an antenna oriented to produce a longitudinal rf electric field. The first-level mask was used to isolate the mesa region defining the extent of the 2DEG. We chose to keep the size of the mesa small to reduce the amount of radiation-induced heating. A mesa size of 40×40 μm provides for a safe 8 μm overlap for both ohmic contacts, and a 12 μm separation to the central device region. The second-level mask is used to pattern the ohmic contacts. The dimensions of the two ohmic contacts were 8 by 30 μm. No second set of contacts was made because of space constraints on the mesa, and the limited number of leads to the mesa. Thus, no 4-point measurement of the device characteristics can be made. The contact resistance to the central mesa must therefore be estimated using values obtained from TLM measurements. The third-level mask is used to pattern contact pads for the test structures and the alignment cross used by the electron-beam machine. This layer does not effect the device. Next, the fine features of the device are patterned using electron-beam lithography. This patterning includes both the definition of the gates and the central region of the antenna terminals. The fourth-level mask is used to pattern the planar antenna and the horizontal leads connecting the gate to the contact pads.

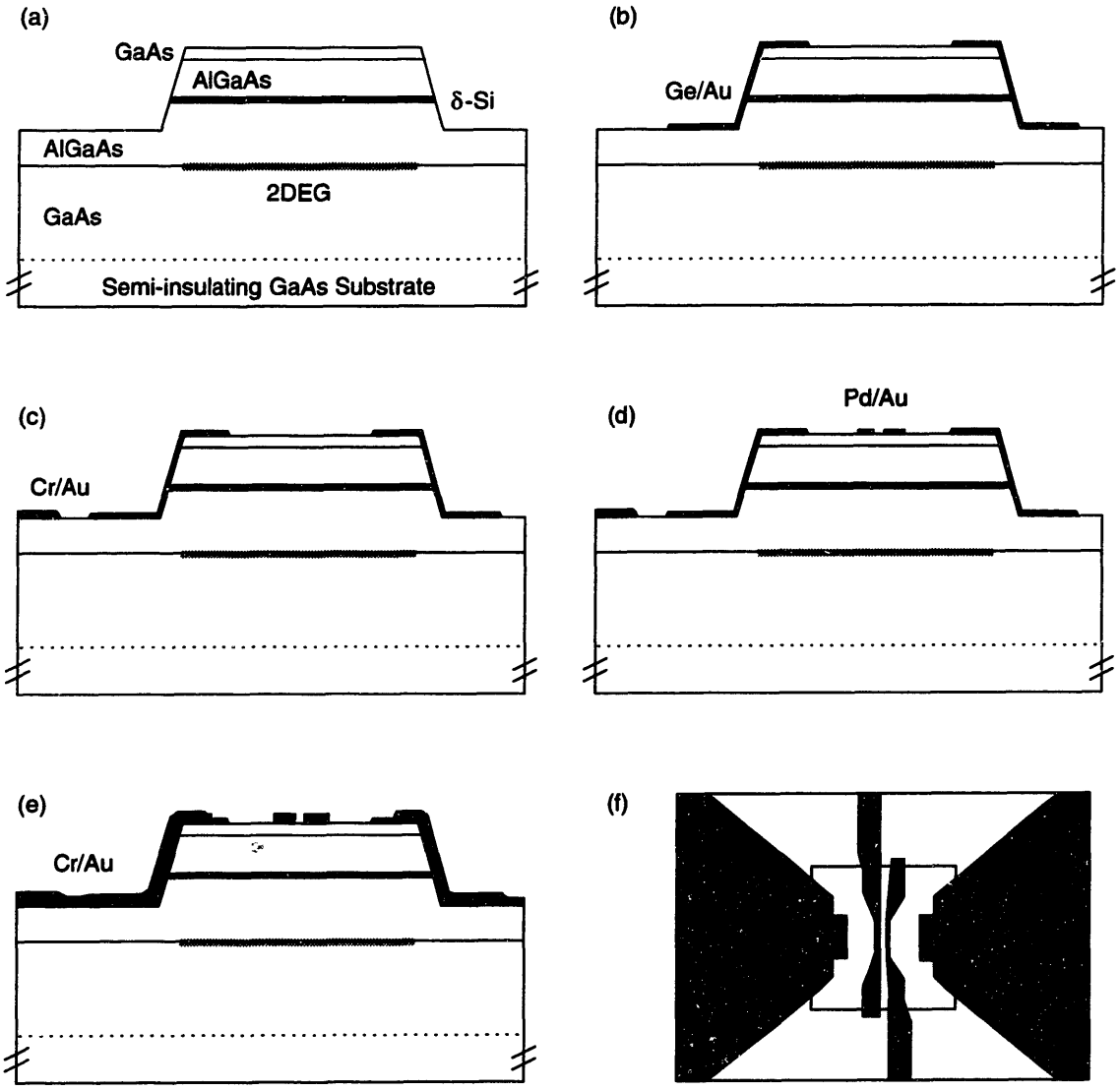

Figure 3-8: Process sequence for antenna-coupled quantum effect devices: (a) wet etch of mesa, (b) deposition and annealing of Ni/Ge/Au/Ni/Au of ohmic contacts using lift-off process, (c) test structure and alignment mark Cr/Au deposition, (d) sub-micron Pb/Au gate deposition defined with electron beam lithography, (e) antenna and bonding pad Cr/Au deposition, (f) top view of completed device.

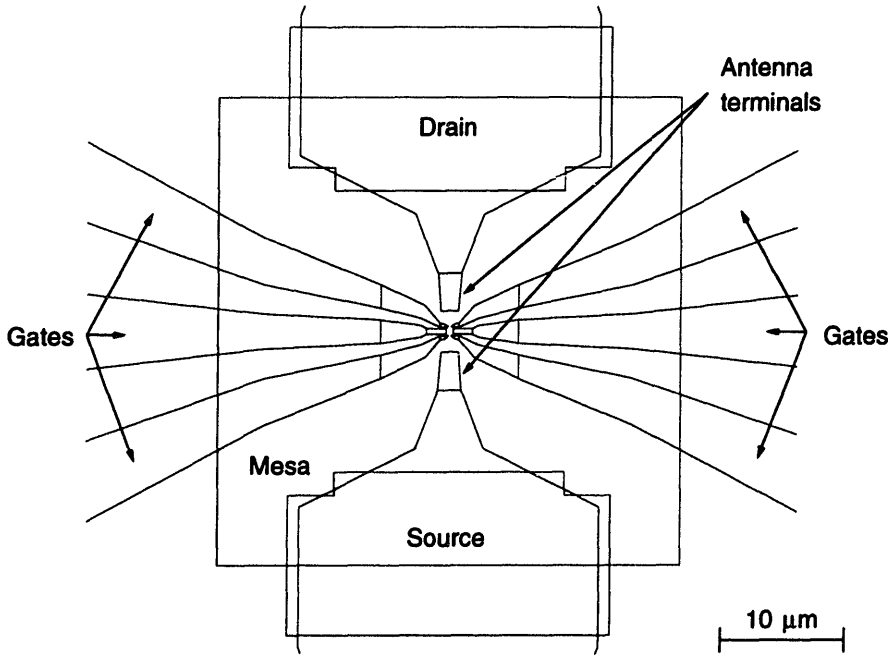

Figure 3-9: Mask drawing of the center region showing mesa, ohmic contacts, gate leads and the antenna terminals.

3.5.3 Test structures

Evaluation of material quality and process characterization requires the use of test structures. A transmission-line-method (TLM) structure is used to determine the contact resistance and the 2DEG sheet resistance. A Hall bar is used to determine the 2DEG carrier density and mobility.

The TLM consists of a 20 μm wide mesa. Ohmic contact pads are separated by incrementally longer gaps. In the mask the separations of 3, 7, 11, 17, 23, 29 and 37 μm have been used. Measurement of the resistance as a function of the gap size yields an approximately linear curve. The slope of this curve multiplied by the width of the TLM mesa yields the 2DEG sheet resistance; the ordinate intercept multiplied again by the width of the TLM mesa yields a value of twice the contact resistance (see Fig. B-1). Typical numbers for the 2DEG sheet resistance are 15 to 20 $\Omega/\square$, and for the contact resistance 0.5 Ω·mm to 1 Ω·mm, at liquid helium temperatures.

The Hall bar consists of a mesa 600 μm long and 200 μm wide, with four 4 μm wide and 20 μm long protrusions placed as voltage probes along the bar (see Fig. 3-7, the lower left corner). Ohmic contacts are patterned on both ends of the bar and at the end of each protrusion. The carrier density of the 2DEG was determined for three MBE films (6128, 6122 and 6167) from the Shubnikov-de Haas oscillations at 4.2 K. The samples were also characterized at 77 K by Dr. A. Förster in KFA Jülich, Germany. Figure 3-10 shows the longitudinal voltage as a function of the inverse magnetic field, applied perpendicularly to the substrate surface. The periodic spacing of the peaks in the longitudinal voltage can be related to the carrier density, n_{2D}, using

$$\Delta\left(\frac{1}{B_\perp}\right) = \frac{e}{h n_{2D}},$$

where e is the electronic charge and h is the Planck constant. From the plots the carrier density was 1.9×10^{11} cm^{-2}, 1.4×10^{11} cm^{-2}, and 1.8×10^{11} cm^{-2}, respectively.

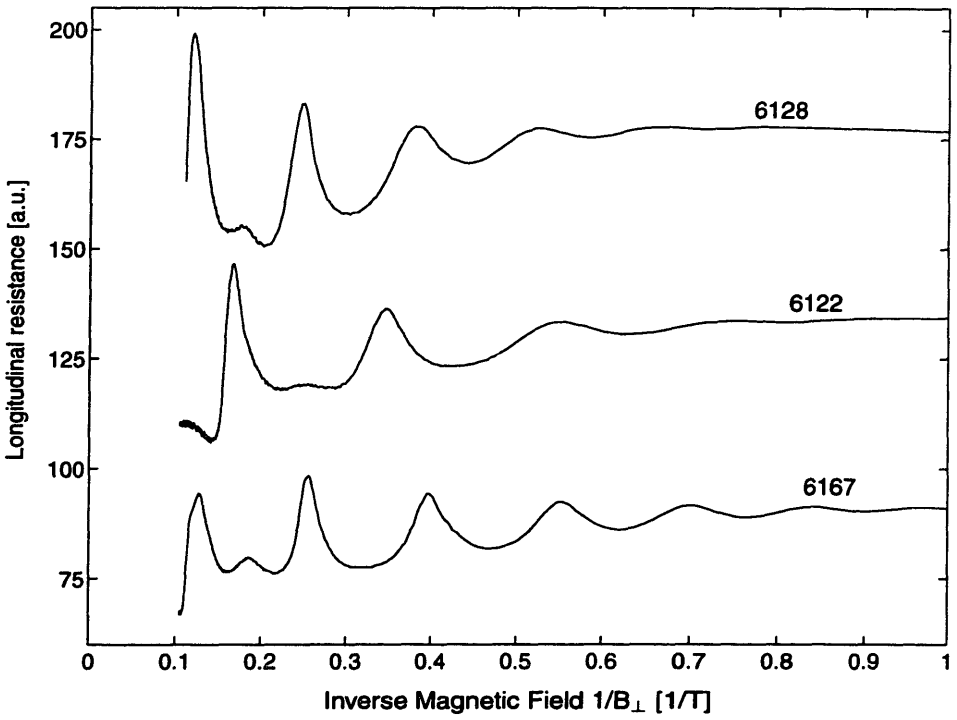

Figure 3-10: SdH measurements of three MBE films listed in Table A.1. Measurements were done at 4.2 K.

These values are low by a factor of about 2.5, compared with values measured at 77 K (see Table 3.1). A probable cause for this discrepancy could be the rapid cooling method used when the device is submerged into liquid helium using a hand-held dewar insert. It has been noticed that both the rate of cooling and the presence of room light affects the carrier density in the 2D channel - conditions which are difficult to control for the dewar used in the measurement [49].

3.5.4 Device structures

We explored a number of different gate structure designs. Scanning electron micrograph (SEM) photographs are shown for two of the designs; one with transverse polarization, and the other with longitudinal polarization. Figure 3-11 shows an SEM

Figure 3-11: SEM micrograph of QPC with transverse radiation coupling.

micrograph of a QPC with transverse radiation coupling. The width of the QPC constriction was 0.15 μm. A log-periodic antenna was used in this design. Figure 3-12 shows an SEM micrograph of an asymmetric dual gate device with a longitudinal radiation coupling. The dimension of the gates were 50 nm and 130 nm, while the separation was 250 nm. The 3 μm wide conduction channel was defined by applying a fixed negative gate voltage to the four gates to deplete the 2DEG. The antenna separation for this device was 1.5 μm. SEM photographs of other device geometries will be shown in the relevant chapter.

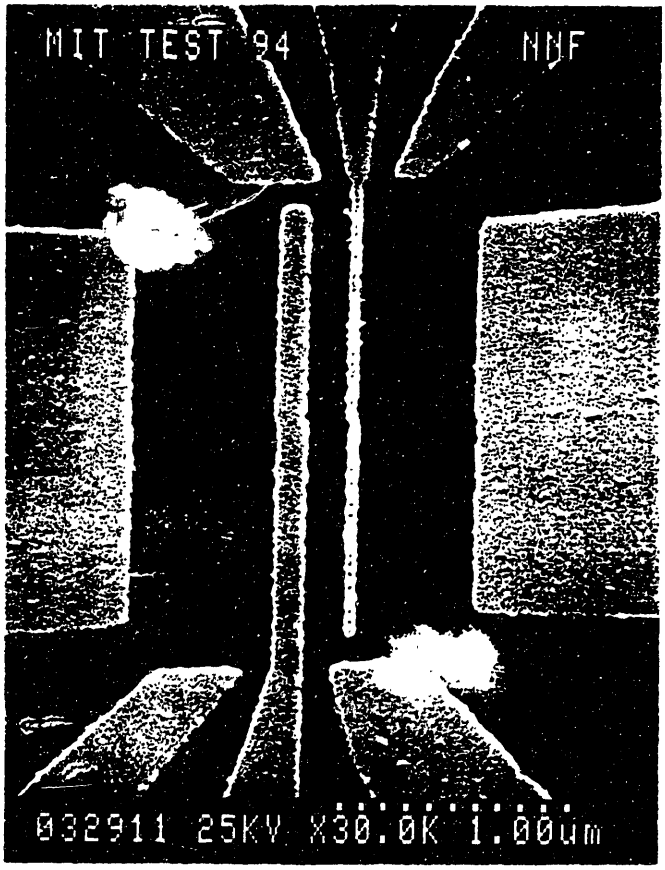

Figure 3-12: SEM micrograph of asymmetric dual gate devices with longitudinal radiation coupling.

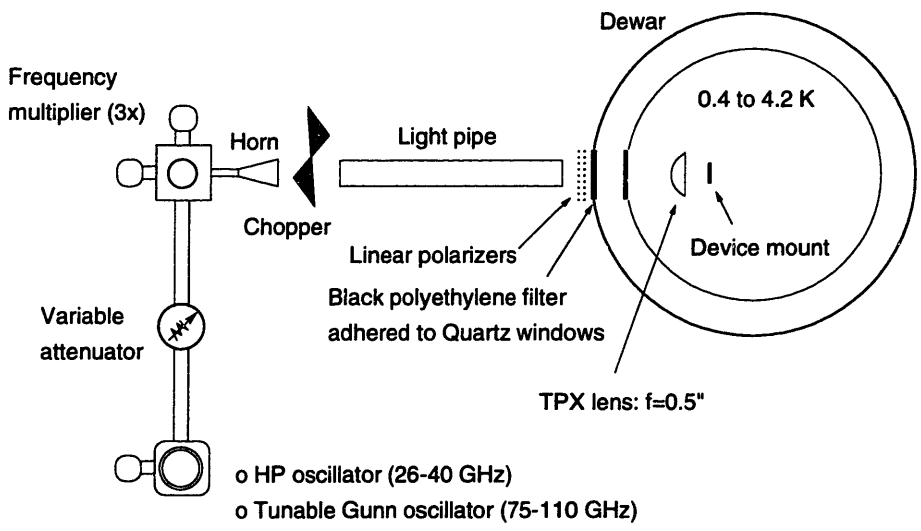

Figure 3-13: Generic measurement system illustrating key components used during photoconductivity measurement.

3.6 Measurement system

Figure 3-13 shows the experimental setup used to measure the photo-response of the devices. The device is mounted in a cryostat with an optical access port. The radiation produced by the external frequency source is then guided by quasi-optical elements into the crystat. For some experiments we also used an oversized circular lightpipe to guide the radiation into the dewar. An attenuator was used to adjust the radiation power level and two wire-grid beamsplitters were used to define the polarization plane of the incident radiation [50]. The relative power level of the radiation could be monitored externally using a pyroelectric detector [51]. The photo-induced currents generated in the device were measured using a standard lock-in technique with the radiation chopped at 17 Hz.

3.6.1 Millimeter and submillimeter wave sources

Several coherent radiation sources were used to measure the photoconductivity of quantum effect devices. In the low frequency band, a Hewlett&Packard sweep oscillator (Model 8690B) was used covering 26-40 GHz. The frequency band 75-110 GHz was reached using a Gunn oscillator [52]. With the help of frequency multipliers, a doubler and trippler diode [53], the bands 160-220 GHz and 225-330 GHz could be accessed. Radiation at higher frequencies was obtained using a CO_2-laser pumped far-infrared laser [54]. Using methanol, the three lines 70.6 μm, 118.8 μm, and 170.6 μm were available [55]. An additional line at 428 μm was obtained using formic acid.

3.6.2 Cryostats

Two cryostats with different quasi-optical systems were used in this thesis. Our first experiments, which concentrated on transport studies of a QPC, were performed using a cryostat in which the device is directly submerged in liquid helium [56]. The radiation, incident on the device side of the substrate, was coupled to the planar antenna using a single TPX lens [57]. This measurement system proved to have two major disadvantages. Firstly, the lowest temperatures achieved in this cryostat were limited to above 1.6 K, achieved by pumping the helium bath. Secondly, the antenna radiation pattern of a planar antenna is predominantly directed into the GaAs substrate. Better radiation coupling can be achieved if the radiation is incident on the device from the substrate side. Taking these two issues into consideration, we used a ^{3}He cryostat [77] with a completely redesigned quasi-optic system in the remainder of the experiments. The design of the redesigned quasi-optic system is discussed in the next section. The lowest temperature achievable with this system was 0.4 K.

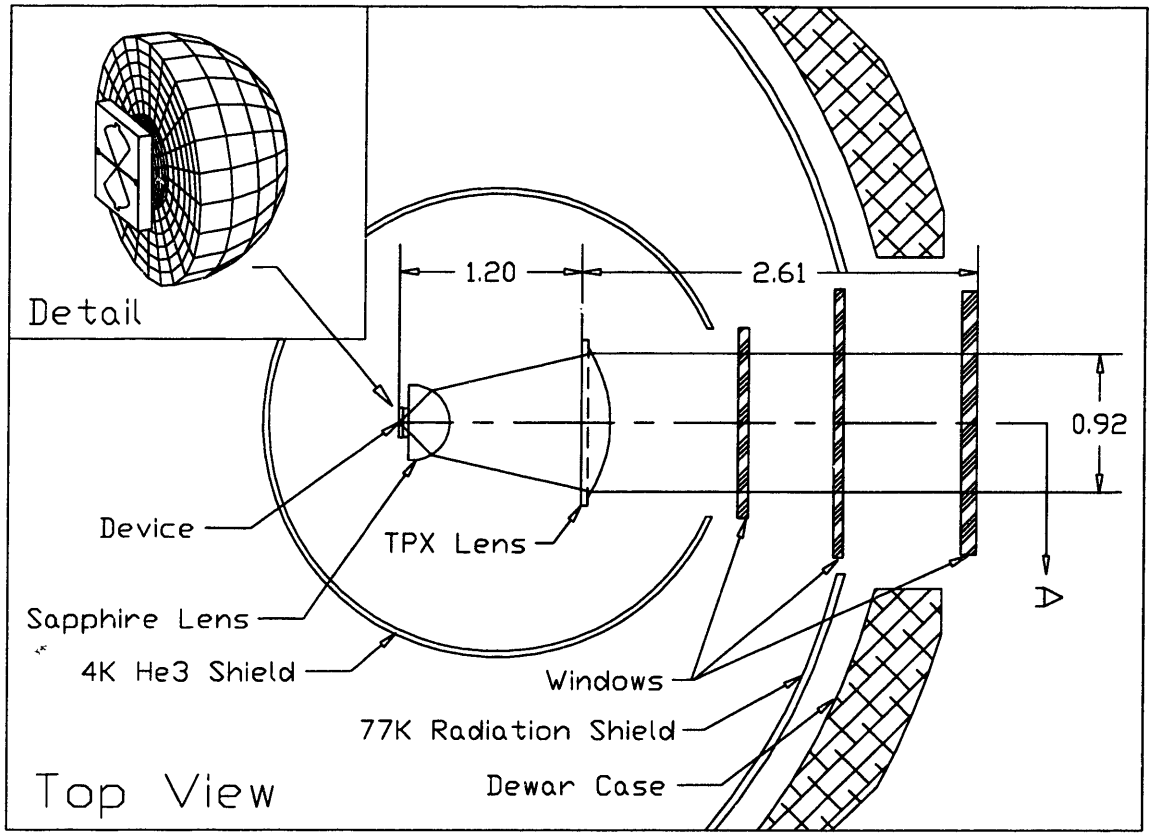

Figure 3-14: Illustration of radiation coupling to the device. All dimensions are in inches.

3.6.3 Quasi-optics

Figure 3-14 shows a top view of the ^{3}He cryostat [77]. The radiation enters the cryostat through an optical access port. A series of low filters are used to prevent radiation in unwanted frequency bands from reaching the device. The power from these frequency bands only presents an additional heat load to the ^{3}He stage and would reduce the hold time of the ^{3}He stage significantly. The first filter is flange mounted to the outside case, the second to the 77 K shield, and the last to the 4 K ^{3}He shield. All three heat filters are identical. They are 1.5 mm thick Z-cut single crystal quartz windows; one side covered with a 4 mil black polyethylene film and the other with 40-60 μm-sized diamond particles. Crystal quartz absorbs efficiently in the near-infrared region (10-30 μm), black polyethylene absorbs visible and some infrared radiation (up to 3 μm), while the diamond particles effectively reject incident radiation in the frequency range from the near-infrared to 70 μm. The remaining radiation is focussed using a TPX (polyolefin polymer based on poly-4 methyl pentene-1) lens and a Z-cut hyperhemispherical single crystal sapphire lens (Al_2O_3) [57]. The inset in Fig. 3-14 shows how the radiation reaches the device from the substrate side. A planar self-complementary antenna was used to focus the rf electric field into the active region of the device. The antenna was oriented to couple a vertically polarized electric field efficiently. The horizontal lines indicate the gate bias leads. In this redesigned setup, the device was mounted in a chip carrier in a vacuum. Cooling of the device was accomplished via physical contact of the substrate backside to the sapphire lens which, in turn, is heat sunk to the copper stand mounted on the He3 cold plate.

The dimensions of the optics layout are shown in Fig. 3-15. The limiting aperture size was set to 0.920". The /F number of the objective lens (TPX) was kept small to capture a large fraction of the planar antenna radiation beam pattern and to avoid significant geometrical aberrations [58]. A focal length $f = 2$" was chosen as a

compromise between low aberration and a small optics system length. This length was further reduced by using a hyperhemispherical sapphire lens which achieved additional focussing of the incident radiation beam.

The optics system was designed for a frequency of 300 GHz, which was in the middle of the frequency band of interest. Since the index of refraction of both the TPX and sapphire varies slowly in this frequency range, the quasi-optical system is broadband. The index of refraction of TPX at this frequency is $n_t = 1.4583$ [59], and that of sapphire is $n_s = 3.0635$ [60]. Using these values, the layout of the optical system can be calculated. For a plano-convex TPX lens, the radius of curvature R_t of the spherical surface is related to the focal length as follows [61]:

$$R_t = (n_t - 1)f = 0.917''.$$

Using a reasonable on-axis thickness of $d = 0.191''$ for this lens, the principal plane is located at

$$h = -\frac{f(n_t - 1)d}{R_t n_t} = -0.131'',$$

where the distance h is measured from the plane side of the lens. An expression for the focussing power of a hyperhemispherical lens is given by Rutledge *et al.* [45] (see Fig. 3-15). For a sapphire lens radius of $R_s = 0.25$" the distance b between the two elements is

$$b = f - h - n_s R_s + \frac{R_s}{n_s} = 1.185''.$$

The small difference in index of refraction between the GaAs substrate and the sapphire lens has been neglected since the substrate thickness is only 0.018".

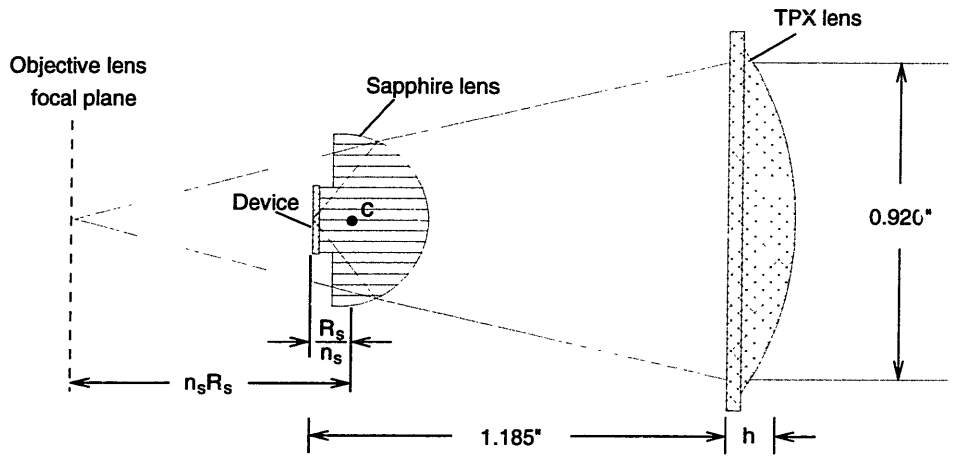

Figure 3-15: Optics elements focussing the radiation. A hyperhemispherical lens combined with an objective lens was used to form an imaging system.

3.6.4 Electronics

An electronic biasing circuit was designed especially for the measurement of the quantum-effect devices. The circuit needed to meet the following requirements: (1) the circuit had to be capable of displaying a real-time device response on an oscilloscope. Such a direct display was necessary during alignment of the radiation with the cryostat optic axis. This ruled out the use of standard lock-in measurement techniques during this alignment procedure. Great care was taken in the circuit layout to avoid 60 Hz contributions due to ground loops; twisted pair wires were used in all signal carrying cables; (2) all wires entering the cryostat were low-pass filtered to prevent radio-frequencies from influencing the device behavior; (3) the circuit had to enable measurements of conductance and transconductance; (4) during the cryostat cooling cycle, it must be possible to short all wires connected to the device to circuit ground. This prevents buildup of static charge which could cause an electrical discharge between the gates of the device. Such a discharge could permanently damage the device.

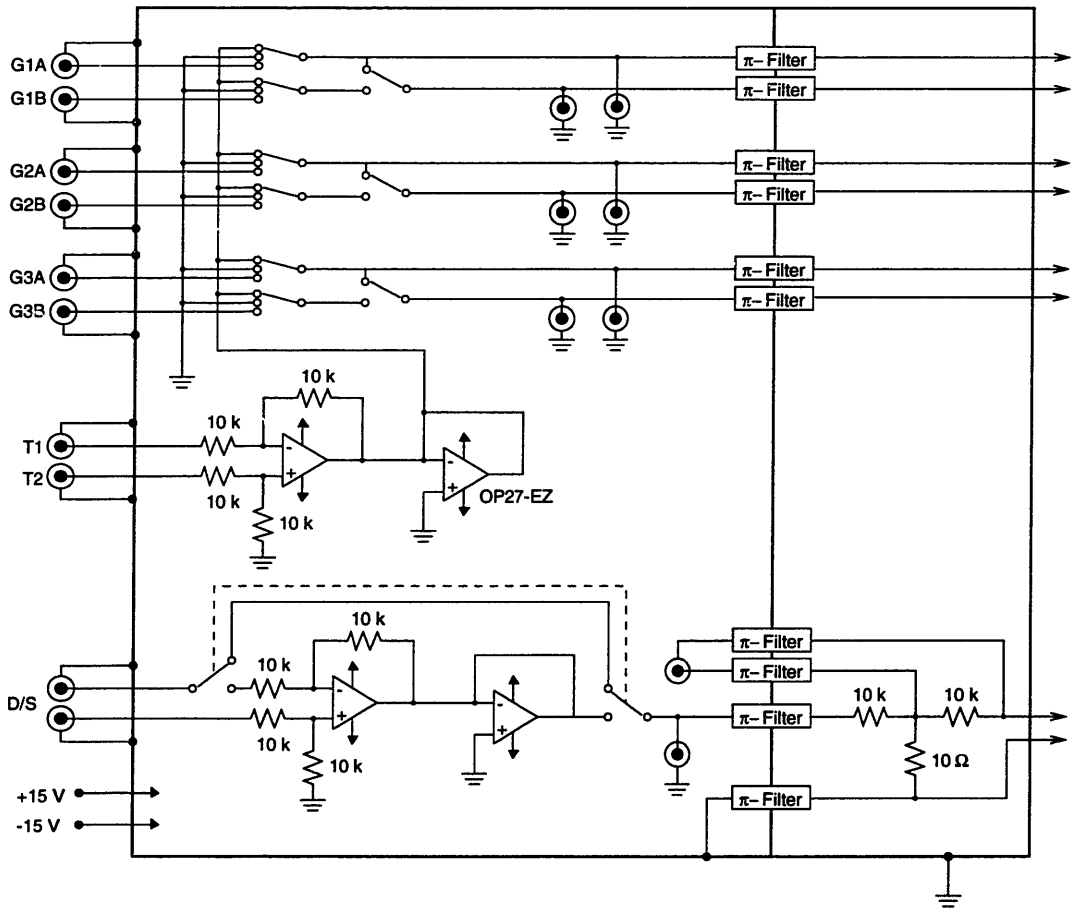

Figure 3-16: Measuring circuit offering maximum flexibility in biasing the 6 Schottky gates of the quantum devices. Inputs G(1,2,3)A/B are for the six gates; T(1,2) are for the transconductance measurement; and D/S are for drain/source bias.

Figure 3-16 shows the final design that satisfies all the requirements. The operational amplifier OP27-EZ was chosen for the adder circuit. This is an ultralow noise precision operational amplifier made by PMI [62]. The low-pass filters are multisection EMI/RFI π-filters made by Murrate-Erie [63]. They achieve an insertion loss of about 65 dB at 100 MHz. The current through the device was found by measuring the voltage drop across the 10 kΩ load resistor. This voltage was amplified using the battery operated Model 113 low noise preamplifier from Princeton Applied Research (PAR). With this amplifier, it was also possible to reject unwanted frequency bands. During the dc measurements, we typically chose a signal bandwidth from dc to 3 Hz. During radiation measurements when a lock-in amplifier was used, the upper cutoff frequency of the PAR 113 amplifier was increased to 300 Hz. All resistors in the circuit were 1% metal film resistors for minimum temperature coefficient. Fig. 3-17 shows a photograph of a real-time scope display of a QPC's drain/source current characteristics as a function of the voltage applied to the split-gate. The drain/source bias voltage was 200 μV, and a Hewlett&Packard pulse/function generator (Model 8661A) was used to sweep the gate voltage at 10 Hz.

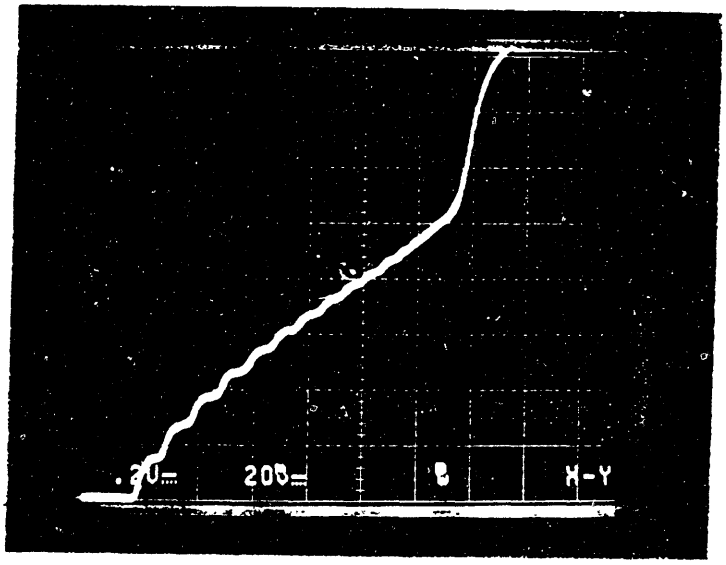

Figure 3-17: Real-time scope display of the drain/source current as a function of the gate voltage for a QPC. The horizontal scale was 0.2 V/div, and the vertical scale was 20 nA/div. A dc drain/source bias voltage of 200 μV was applied across the QPC and a source resistor of 1 kΩ. The liquid helium bath temperature was 1.6 K.

Chapter 4

Quantum point contact

4.1 Introduction

This chapter discusses the dc transport characteristics of a quantum point contact. Section 4.2 shows an $I_{ds} - V_{gs}$ characteristic of a quantum point contact (QPC), defined using a split-gate geometry. The distinction between one-dimensional and two-dimensional transport regimes are made. The signature feature of the one-dimensional transport regime are conduction steps, the heights of which are derived in section 4.3. Section 4.4 introduces a simple model of the electrostatic potential at the maximum constriction of a QPC. This model was used to analyze the effects of finite temperature in section 4.5, the transconductance in section 4.6, and one-dimensional subband depopulation by perpendicular magnetic fields in section 4.7. As a result of the analysis, we were able to estimate the one-dimensional subband energy spacing.

4.2 Transport regimes

Figure 4-1 shows an SEM micrograph of the QPC design we used. The raised square region in the center of the photograph was the mesa defining the extent of the two-

dimensional electron gas (2DEG). The 2DEG was connected to an external bias circuit via the two horizontal leads. The vertically oriented log-periodic antenna served simultaneously to focus the radiation field and to define the split-gate quantum point contact constriction. In this orientation, the antenna generated an ac voltage transverse to the electron transport direction.

The transport characteristic of a QPC is shown in Fig. 4-2. A bias voltage of $V_b = 100\ \mu$V in series with a $R_l = 1$ kΩ load resistor was used to measure the device at a temperature of $T = 1.6$ K. The plot shows the current I_{ds}, flowing through the load resistor and the QPC, as a function of the voltage V_{gs} applied to the split-gates. The split-gate QPC behavior in Fig. 4-2 can be divided into two regimes. At zero gate voltage, current flowed throughout the entire mesa between the drain and source ohmic contacts. As the gate voltage is decreased, the 2DEG directly under the split-gates becomes depleted. Between 0 to -0.5 V, this manifested itself as a gradual decrease of the total current. The current dropped rapidly between -0.5 V and -0.7 V because the 2DEG directly under the gates becomes fully depleted. At lower gate voltages, the current flowed through a narrow conductive channel between the split-gates. This current decreased approximately linearly with gate voltage. At about -0.85 V, small ripples started to appear which resemble a staircase-like behavior. The current was seen to remain approximately constant for a gate voltage interval and then to drop and reach a new constant level. These current plateaus became more visible as the device's pinch-off voltage was approached. Experimental evidence of this novel staircase-like behavior, indicative of one-dimensional ballistic transport, was first reported in 1988 by van Wees *et al.* [1] and Wharam *et al.* [2]. The explanation of this surprising behavior of a narrow channel split-gate device will be the topic of the next section.

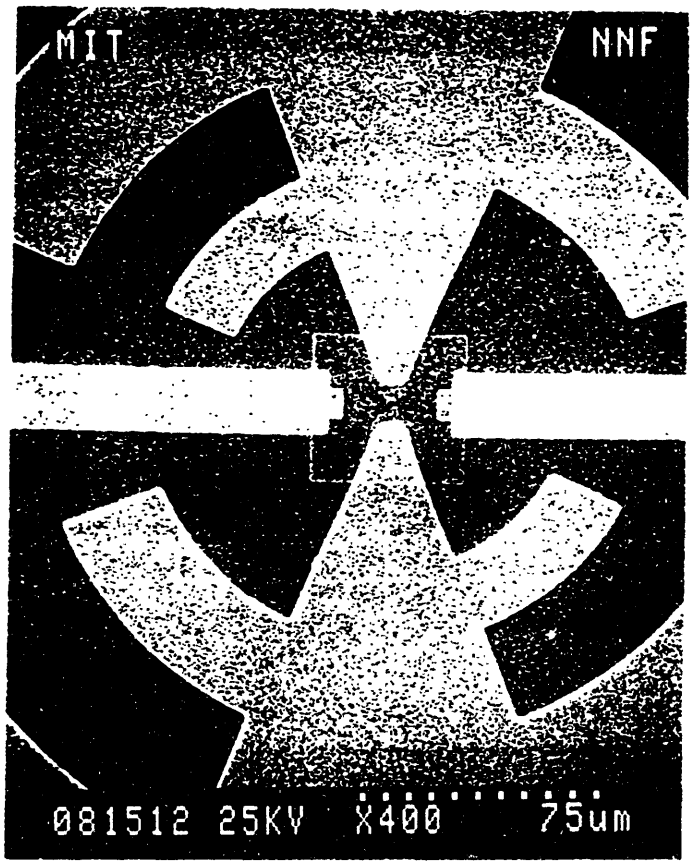

Figure 4-1: Scanning electron micrograph (SEM) of a quantum point contact with transverse radiation coupling. The horizontal leads are the drain and the source contacts to the 2DEG. The two ohmic contacts were placed at the edge of the 50×50 μm^2 mesa. The log-periodic antenna used in this design focussed the ac voltage transverse to the electron transport direction. The gap of the quantum point contact constriction was 0.15 μm. The vertical dimensions appear shorter because the substrate was mounted at a 45 degree inclination.

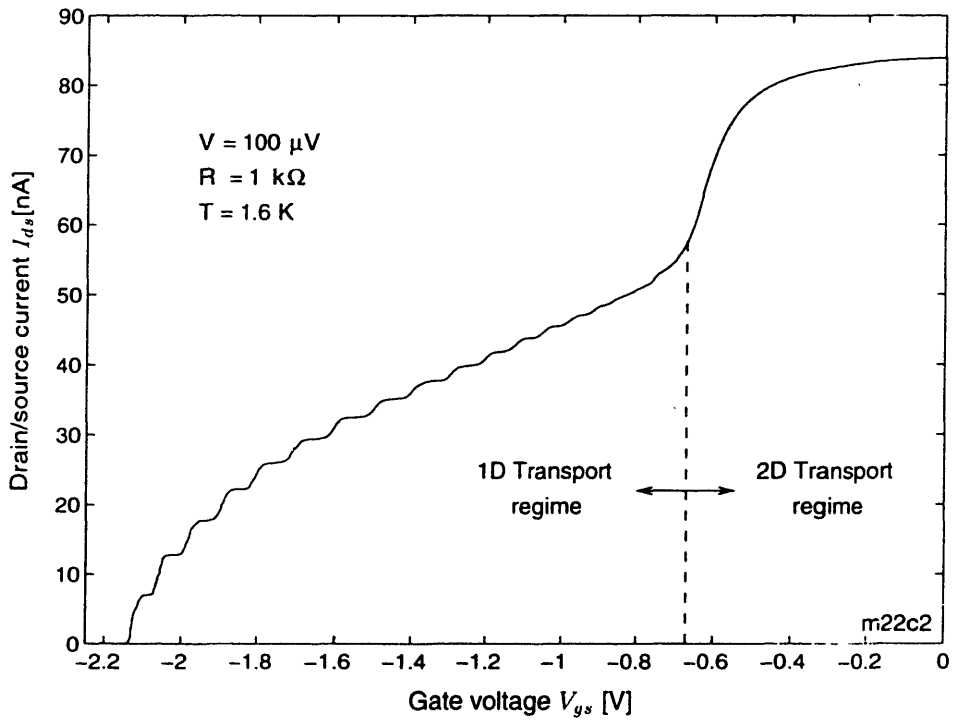

Figure 4-2: Drain/source current I_{ds} as a function of gate voltage V_{gs}. The separation between the one-dimensional and two-dimensional transport regime is indicated by the vertical division.

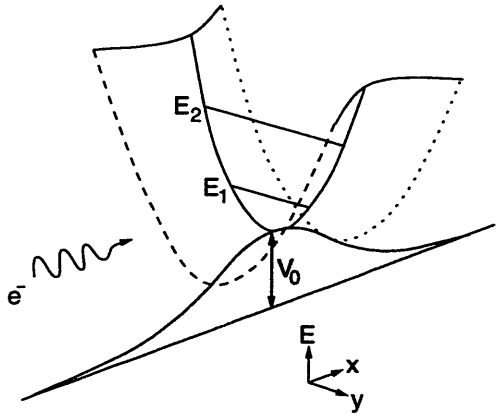

Figure 4-3: Schematic illustration of electrostatic potential induced in the 2DEG upon application of a negative gate voltage, resulting in lateral confinement in the y-direction and a potential barrier in the x-direction.

4.3 Quantized conductance

As the one-dimensional transport regime is entered, the width of the conduction channel between the split-gates becomes comparable to the wavelength associated with the electrons close to the Fermi level. In the presence of such a strong transverse confinement, the conduction through the channel is governed by quantum mechanics. To a very good approximation, we can describe this transverse confinement in the y-direction by using an harmonic oscillator potential

$$V(y) = V_0 + \tfrac{1}{2}m^*\omega_y^2 y^2,$$

where V_0 is the electrostatic potential at the constriction, m^* is the electron effective mass, and ω_y is the curvature of the potential expressed in angular frequency. The definition of the coordinate system with respect to the quadratic confining potential for the model QPC is shown in Fig. 4-3. Our current discussion is valid at position $x = 0$; we will later generalize the results to the full saddle-point potential. Discrete levels form due to the transverse confinement at energies $E_n = V_0 + \hbar\omega_y(n - \frac{1}{2})$, where $n = 1, 2, \ldots$ is the subband number. For an electron to propagate through subband n of the constriction its total energy must exceed E_n. The energy dispersion of the

electron is given by

$$E = \frac{\hbar^2 k_x^2}{2m^*} + E_n, \tag{4.1}$$

where the x-direction is defined along the channel. The binding energy of the two-dimensional electron gas due to vertical confinement at the AlGaAs/GaAs heterointerface, which is much greater than $\hbar\omega_y$, has no effect on conduction and was left out. As is evident from Eq. 4.1, the transverse confinement causes the formation of discrete subbands. The bottom energy of the energy dispersion relation for subband n starts at E_n and varies quadratically with the longitudinal wavevector k_x. These subbands, frequently referred to as propagation modes, are analogous to the modes of electromagnetic radiation that propagate through waveguides.

The current through a single subband can be calculated using the energy dispersion of Eq. 4.1. The density of states for subband n, accounting for the two-fold degeneracy of the electron spin, is

$$g_{1D,n}(E) = \frac{1}{\pi}\sqrt{\frac{2m^*}{\hbar^2(E - E_n)}}, \tag{4.2}$$

where the incident electron energy E must satisfy $E \geq E_n$. The velocity of an electron at this injection energy is given by

$$v_n(E) = \sqrt{\frac{2(E - E_n)}{m^*}}. \tag{4.3}$$

By combining Eq. 4.2 and Eq. 4.3, the contribution to the total current by propagating electrons in an energy interval $\Delta\mu$ in subband n can be found:

$$\frac{\Delta I}{\Delta\mu} = -\tfrac{1}{2}\, e\, g_{1D,n}(E)\, v_n(E) = -\frac{2e}{h}, \tag{4.4}$$

where a factor of $\frac{1}{2}$ is needed to count only the electrons which travel towards the

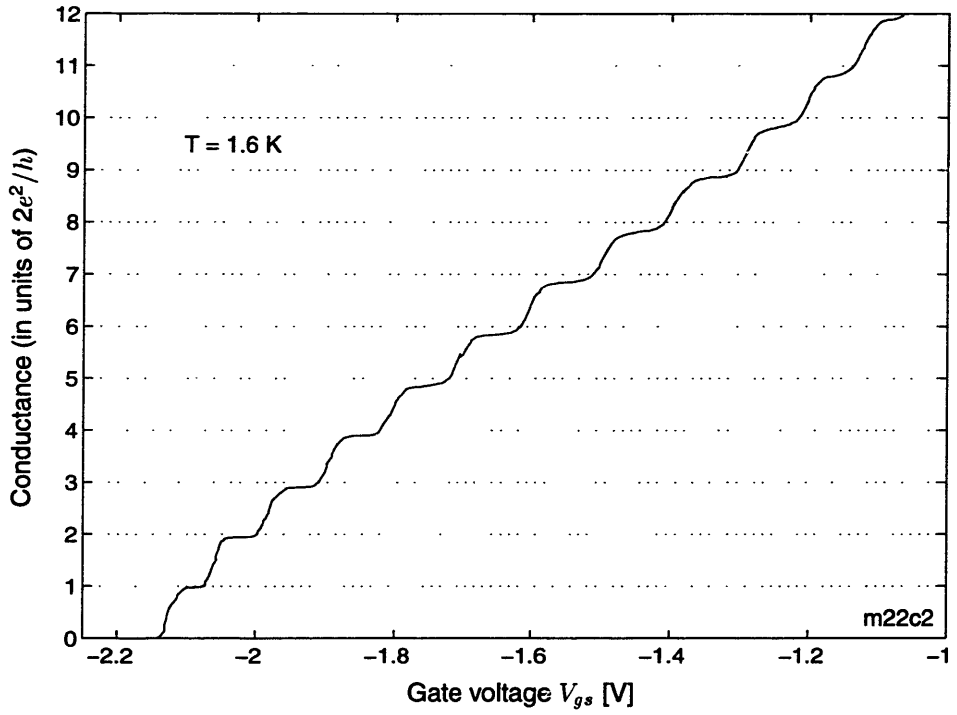

Figure 4-4: First eleven conductance steps of device m22c2 measured at 1.6 K. Data is obtained by performing a two-terminal measurement. The 1 kΩ load resistor and an estimated total contact resistance of 200 Ω have been taken into account (The resistance of an 8 μm wide ohmic contact is typically 0.8 Ω·mm/8 μm = 100 Ω.).

constriction. The energy interval $\Delta\mu$ is the difference in chemical potential between the drain and the source sides of the constriction. This difference in chemical potential is equal to the external voltage source $-e\Delta V$ connected between the drain and the source. Upon substituting of $\Delta\mu = -e\Delta V$ into Eq. 4.4 we find

$$\frac{\Delta I}{\Delta V} = \frac{2e^2}{h}, \tag{4.5}$$

which is the quantized conductance from a single subband. Remarkably, this value is independent of the Fermi energy and material parameters and only depends on universal constants.

We have confirmed the staircase nature of current conduction through a one-dimensional channel predicted by Eq. 4.5 by computing the conductance from the $I_{ds} - V_{gs}$ data displayed in Fig. 4-2. Figure 4-4 shows the first 11 conductance steps plotted in units of $2e^2/h$. The height of each plateau approximately coincides with the predicted step height for one-dimensional conduction behavior after the data has been corrected for the effects of the load resistor and the ohmic contact resistance. For higher subband steps the plateaus fall slightly below integer values. Imperfections in the constriction cause the reduction of the transmission probability from 1. Denoting this transmission probability as t_n, the conductivity of a quantum point contact described with a parabolic transverse potential is given by

$$G = \frac{2e^2}{h} \sum_n t_n \theta(E_F - E_{y,n}), \tag{4.6}$$

where $\theta(E)$ is the unit step function.

4.4 Split-gate model

The origin of the quantized conductance step has been explained above. However, in order to qualitatively understand the QPC behavior, a model is needed to describe the conduction onset of a subband. Such a model can be used to analyze transconductance and magnetic field measurements of QPC.

For a split-gate QPC design, the electrostatic potential close to the constriction is expected to vary slowly on the scale of a Fermi wavelength. If we approximate the electrostatic potential at the constriction by a polynomial expansion of second order, we have

$$V(x,y) = V_0 - \tfrac{1}{2} m^* \omega_x^2 x^2 + \tfrac{1}{2} m^* \omega_y^2 y^2. \tag{4.7}$$

Here, the electrostatic potential at the center is V_0, the effective mass of the electron

is m^*, and the curvatures of the potential along the coordinate directions x and y are ω_x and ω_y, respectively. The definition of the coordinate system is illustrated in Fig. 4-3. The quadratic potential in the y-direction, identical to the previously discussed parabolic potential, results in uniformly spaced quantized energy levels. The Hamiltonian for this system is

$$H = \frac{1}{2m^*}\mathbf{p}^2 + V(x,y). \tag{4.8}$$

In the absence of quantum mechanical tunneling through the barrier, the threshold energies for subbands $n = 1, 2, \ldots$ at the saddle point are given by

$$E_n = V_0 + \hbar\omega_y(n - \tfrac{1}{2}). \tag{4.9}$$

At zero temperature, subbands with threshold energies lower than E_F are activated, while subbands with threshold energies above E_F are closed.

The transmission coefficient through a saddle-point potential have been calculated by Fertig and Halperin [64]. For each subband n, it can be expressed in an analytical form

$$T_n = \frac{1}{1 + e^{-2\pi\varepsilon_n(E)}} \tag{4.10}$$

using the variable

$$\varepsilon_n(E) = \left[E - V_0 - \hbar\omega_y(n - \tfrac{1}{2})\right]/\hbar\omega_x, \tag{4.11}$$

where $E = E_x + E_y$ is the total energy of an electron incident on the constriction. The transmission coefficient given by Eq. 4.10 produces a smooth step with a rise width we can quantify. In the limit of $\omega_x = 0$, the transmission coefficient reduces to $\theta(E - E_n)$.

Using the results from the saddle-point potential, a description of the conduc-

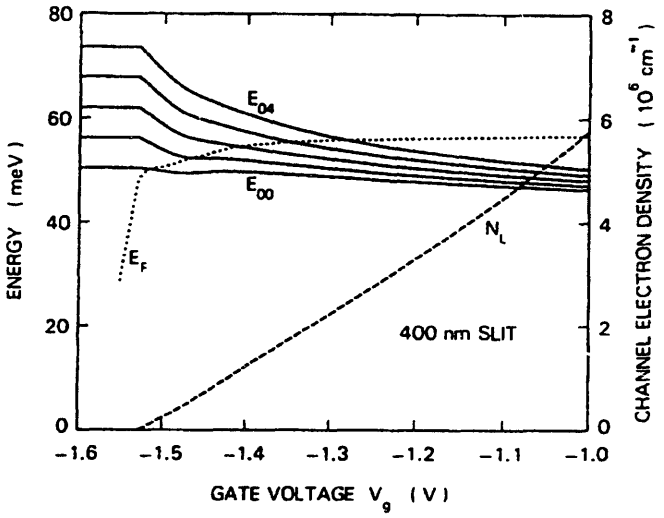

Figure 4-5: Self-consistent simulation of a split-gate device with a gate opening of 0.4 μm and a 2DEG located 70 nm below the surface [65]. The five lowest subband energies, the Fermi energy E_F (dotted curve), and the integrated charge per unit length in the channel (dashed curve), are shown versus the gate voltage.

tance of a QPC has been obtained as a function of the energy of an incident electron. One additional step is required to complete the model and obtain a description as a function of the split-gate voltage V_{gs}. By limiting our interest to an explanation of maximum slope of the conduction steps (peak transconductance), a model is required only in the vicinity of the conduction threshold for each subband. Self-consistent simulations for a split-gate geometry, reproduced in Fig. 4-5, have shown that the subband energy spacing and the Fermi energy E_F varies slowly at the onset of conduction for each subband [65]. We propose to describe this behavior of the electrostatic potential as a function of gate voltage as follows: at the threshold of conduction for subband p, we let the curvatures be $\omega_{x,p}$ and $\omega_{y,p}$. A dependence of the curvatures on V_{gs} has therefore been included by allowing for different values at each conduction threshold. The value of the curvatures is assumed to remain approximately constant in the vicinity of each threshold. In addition, the electrostatic potential at the saddle, V_0,

is assumed to vary linearly with V_{gs}. From the data shown in Fig. 4-4, it is apparent that the gate voltage difference between adjacent conductance steps is approximately constant. Denoting this voltage difference by ΔV_s, and the threshold voltage of the first subband by V_t, we introduce the dimensionless parameter

$$\nu_{gs} \equiv \frac{V_{gs} - V_t}{\Delta V_s} + 1,$$

which takes on integer values each time the gate voltage reaches the onset of a subband. The electrostatic potential at the center, V_0, can now be expressed as

$$V_0 = E_F - \hbar\omega_{y,p}(\nu_{gs} - \tfrac{1}{2}) \tag{4.12}$$

when the gate bias voltage corresponds to the threshold voltage of subband p. Substitution of Eq. 4.12 into Eq. 4.11 gives

$$\varepsilon_n(E) = \left[E - E_F - \hbar\omega_{y,p}(n - \nu_{gs})\right] / \hbar\omega_{x,p}, \tag{4.13}$$

where the gate voltage dependence of the curvature has been added. The variable ε_n is now a function of the gate voltage V_{gs}. Based on our assumptions, this expression is only valid in the vicinity of a conductance step when $\nu_{gs} \approx p$. The conductance is found by substituting the transmission coefficient from Eq. 4.10 into Eq. 4.6:

$$G = \frac{2e^2}{h} \sum_n \frac{t_n}{1 + e^{-2\pi\varepsilon_n(E_F)}}, \tag{4.14}$$

where t_n is the maximum transmission probability of channel n, and ε_n is given by Eq. 4.13. In the absence of any imperfection in the conduction channel, t_n is equal to 1. For a real system, the value tends to be slightly smaller. Section 4.5 discusses the generalization of Eq. 4.14 to finite temperatures.

Numerical estimates for the curvatures describing the saddle-point potential can be found from experimental data by the following method. Let us define the voltage ΔV_w as the width between adjacent transmission plateaus in which the step height goes from 10% to 90%. Using Eq. 4.14, we find this width is related to the curvatures $\omega_{x,p}$ and $\omega_{y,p}$ as follows:

$$\frac{\omega_{y,p}}{\omega_{x,p}} = \frac{2\ln 3}{\pi}\left(\frac{\Delta V_s}{\Delta V_w}\right). \tag{4.15}$$

It is interesting to note that for a QPC with well-quantized steps, the value of $\Delta V_s/\Delta V_w$ is approximately constant. This means that the curvatures ω_x and ω_y of the saddle-point potential have a similar gate voltage dependence. For the conductance steps of device m22c2 shown in Fig. 4-4, with $\Delta V_s = 68$ mV and $\Delta V_w = 27$ mV, the ratio of the curvatures is 1.8 for the first conductance step (see Table 4.1). The ratio of the two curvatures in Eqn. 4.15 has also been used as a measure of the quality of a quantum point contact [66]. The higher the value of the ratio, the more visible are the conductance steps.

A large value for $\omega_{y,p}$ is obtained by strong confinement in the y-direction. A small value for $\omega_{x,p}$ is obtained by using a gradual tapering of the channel along the x-direction. Hence, a closely-spaced, smoothly-varying split-gate geometry should be used to form the conduction channel. The importance of proper design for the split-gate geometry is illustrated in Fig. 4-7. Identical layouts for the split-gates have been used for the three QPCs, but the separation has been varied from 0.15 μm to 0.25 μm. The depth of the 2DEG for these device was 55 nm. Varying the gap width affects both the threshold voltage V_t and the step quality of the QPC. For the 0.15 μm gap, the steps are visible, but ΔV_s is too small. For the 0.20 μm gap, the step definition is satisfactory, with a sufficiently large ΔV_s. For the 0.25 μm gap, additional oscillatory features appear on the first quantized conductance step. A plausible explanation for this feature is the existence of resonant levels above the conduction threshold

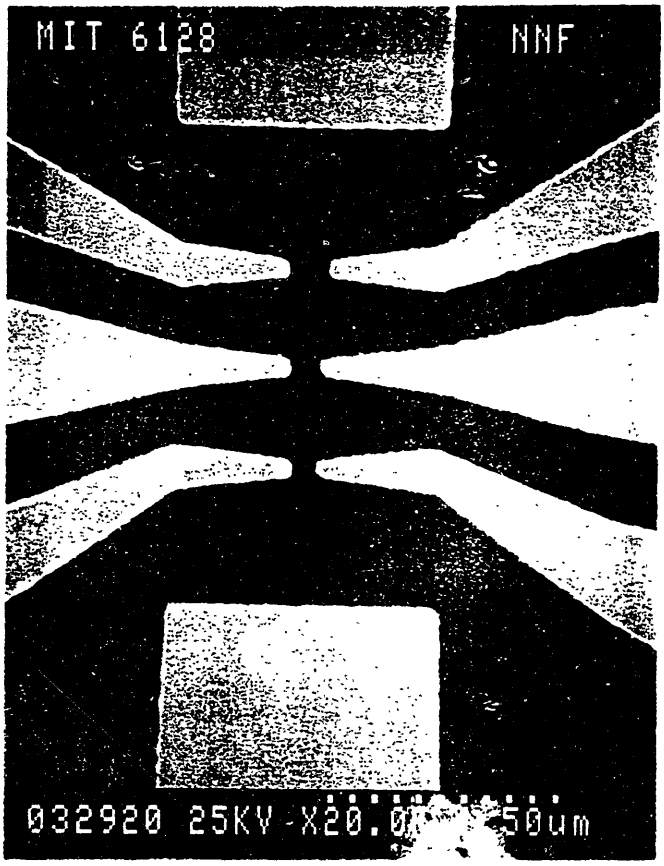

Figure 4-6: SEM photograph of three QPCs with a longitudinal radiation coupling. The width of the constriction was 0.15 μm, 0.2 μm, and 0.25 μm. The antennna terminal separation was 8 μm.

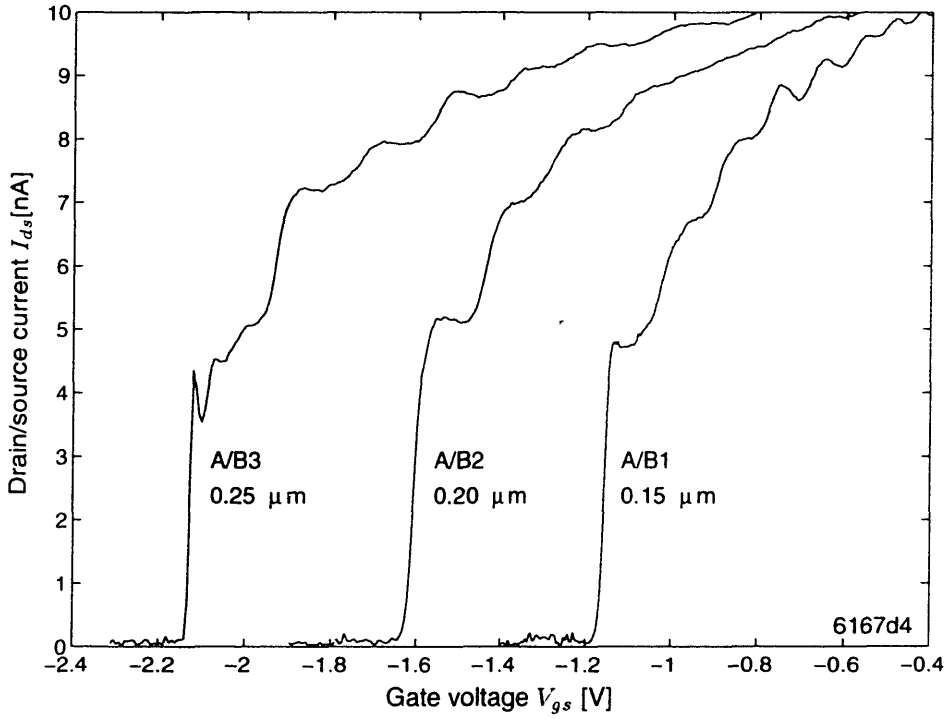

Figure 4-7: Pinch-off voltage variation as a function of QPC gap. Separation of gate pairs A/B1, A/B2, and A/B3 are 0.15 μm, 0.20 μm and 0.25 μm, respectively. Measurement conditions were $V_b = 100$ μV, $R_l = 10$ kΩ and T = 1.6 K.

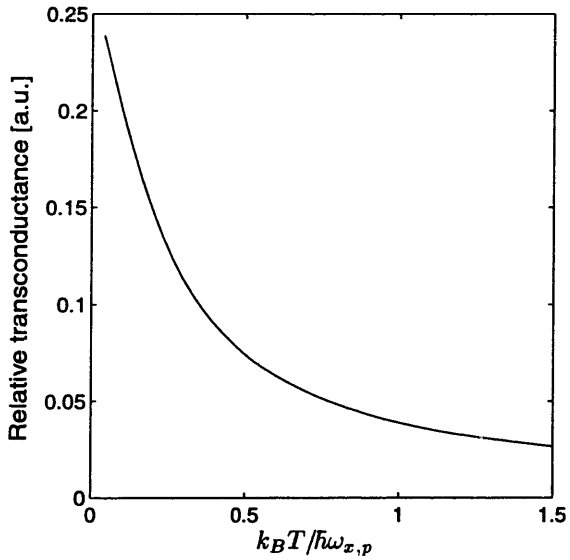

Figure 4-8: Maximum transconductance at threshold of subband p as function of the ratio $k_BT/\hbar\omega_{x,p}$.

for the first subband [67, 68]. These resonant levels are possible for long uniform one-dimensional channels. In conclusion, the best quantized conduction steps have been observed when the gap separation was about four times greater than the 2DEG depth.

4.5 Finite temperatures

At finite temperatures, a fraction of the electrons in the drain and the source are thermally excited from below to above the Fermi level E_F. This rearrangement of electrons is described by the tail of the Fermi-Dirac distribution function. Mathematically, the effect of finite temperature on the conductance can be taken into account using the convolution method developed by Bagwell and Orlando [69]. For a one-dimensional system at finite temperatures, the conductance is given by

$$G = \frac{2e^2}{h} \sum_n \frac{t_n}{1 + e^{-2\pi\epsilon_n}} \otimes \left(-\frac{\partial f}{\partial E} \right), \tag{4.16}$$

where $f = 1/[1 + \exp[(E - E_F)/k_BT]]$ is the Fermi-Dirac distribution function, and

$\otimes$ is used to signify the convolution operation. At finite temperatures, both the width of the plateau region and the slope between the conductance steps decrease. In Fig. 4-8, the slope at the onset of subband p is shown as a function of $\omega_{x,p}$ and temperature T. This slope is proportional to the transconductance of the quantum point contact. The slope decreases rapidly with increasing temperature, followed by an approximately linear decrease when $k_BT/\hbar\omega_{x,p}$ is larger than 0.5. For a quality ratio of $\omega_y/\omega_x = 3$ and a subband spacing of $\hbar\omega_y = 5$ meV, this transition occurs at about 20 K. Measurements of quantum-effect devices are typically made at and below 4.2 K. In this temperature range $k_BT/\hbar\omega_{x,p} \ll 1$ and we expect to operate in the left-most region of the curve. In conclusion, the finite width between quantized conductance steps observed at very low temperatures is predominantly a result of the potential profile at the constriction. Thermal broadening of the step plays a secondary role. As will be shown in section 4.6, a measurement of transconductance as a function of temperature can be used to determine the longitudinal curvature $\omega_{x,p}$.

4.6 Transconductance

In this section, an expression for the transconductance at the conduction threshold of subband p is derived. In particular, we are interested in determining $\omega_{x,p}$ by monitoring the decrease of the transconductance as a function of temperature.

The $I_{ds} - V_{gs}$ characteristics of a quantum point contact were measured using a fixed bias voltage V_b and a load resistor R_l. The resistance of a quantum point contact at the onset of conductance step p is $R_q/(p - \frac{1}{2})$, where R_q is defined as $h/2e^2$. The transconductance at zero temperature is given by

$$g_m \equiv \frac{\partial I_{ds}}{\partial V_{gs}} = \frac{R_q V_b}{\left[R_q + R_l(p - \frac{1}{2})\right]^2} \left(\frac{\partial T_p}{\partial V_{gs}}\right), \tag{4.17}$$

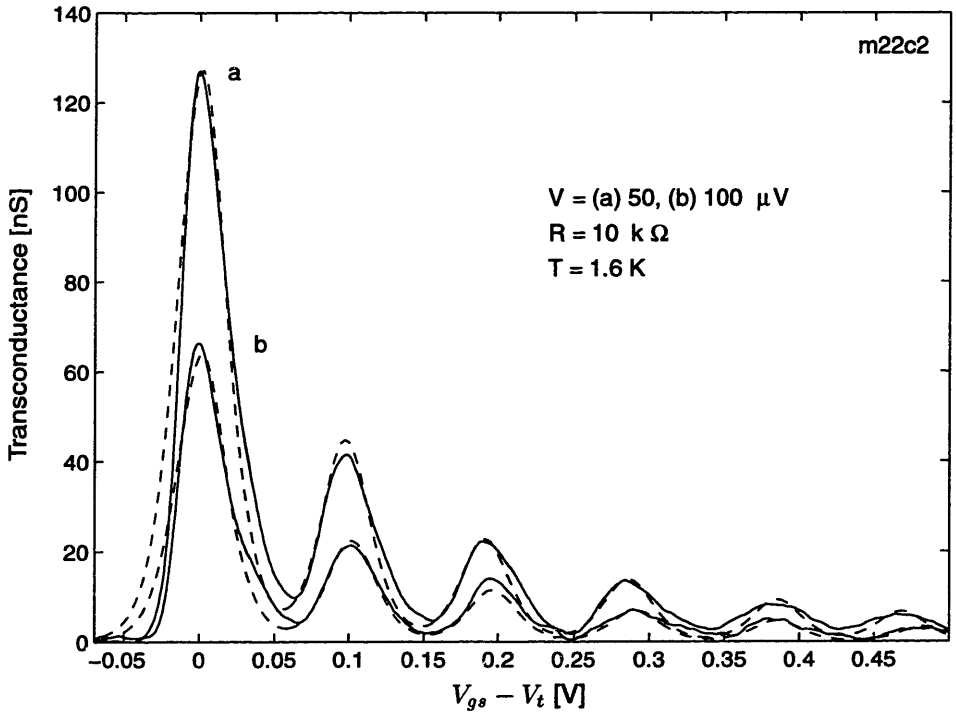

Figure 4-9: Comparison of measured (solid line) and calculated (dashed line) transconductance for device m22c2. The dc bias voltage V_b was (a) 100 μV and (b) 50 μV, the load resistor $R_l = 10$ kΩ, and the bath temperature $T = 1.6$ K. Simulation parameters were $\Delta V_s = 95$ mV, $\omega_y/\omega_x = 1.9$ and $t = 1$. The experimentally determined Fermi energy for the 2DEG was $E_F = 10.0$ meV.

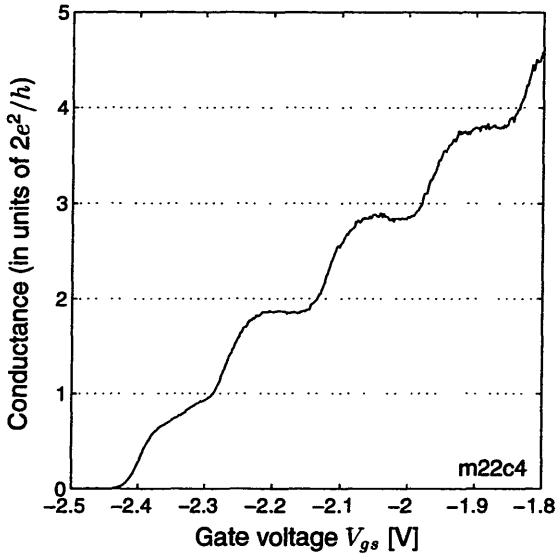

Figure 4-10: Conductance step of QPC m22c4 measured at 1.6 K.

provided V_b remains constant. Here, T_p is the transmission coefficient at conduction threshold for subband p. Evaluating the derivative of the transmission coefficient with respect to the gate voltage we find

$$\frac{\partial T_p}{\partial V_{gs}} = \frac{\pi t_p}{2\Delta V_s}\left(\frac{\omega_{y,p}}{\omega_{x,p}}\right), \tag{4.18}$$

where t_p is the maximum transmission probability of channel p. Figure 4-9 shows a measured transconductance and the prediction based on Eq. 4.17. Since the simulation was done numerically, the finite temperature has been taken into account and a continuous curve for the transconductance has been calculated. A good fit for all the peak heights was obtained using constant values for $\omega_y/\omega_x = 1.9$, and $t = 1$ for all subbands. This estimate of the ratio seems reasonable since the device shows well-defined steps. The ratio of 1.9 compares well with the value obtained from the dc $I_{ds} - V_{gs}$ curve for the same device, see Table 4.1.

Next, we investigated the temperature dependence of the transconductance. A different device was used in this set of measurements. The distinction between results obtained for the two different devices is clearly made in Table 4.1. The quantized

conductance step of QPC m22c4 is shown in Fig. 4-10. Apart from the rounding of the first step, the conductance plateaus are well defined. The transconductance of this device has been measured as a function of temperature. In Fig. 4-11, the peak height reduction of g_m is shown for the first three subbands. As the temperature was varied from 1.6 to 5.6 K, a decrease of 8%, 33% and 44% was observed for subbands 1, 2 and 3, respectively. Based on the relationship between $\omega_{x,p}$ and T, shown in Fig. 4-8, we obtained the following estimates: $\hbar\omega_{x,p} = 12.3$, 2.6 and 1.7 meV for $p = 1$,2 and 3. Even the smallest energy, 1.7 meV, corresponds to a temperature of about 1.7 meV/$k_B \approx 20$ K. We are therefore operating in a regime where $k_BT/\hbar\omega_{x,p} \ll 1$ since $T \leq 5.6$ K in the measurement.

Using Eq. 4.17 we can solve for $\omega_{y,p}$. The experimental parameters were $V_b = 100$ μV and $R_l = 10$ kΩ. The transmission coefficients and subband threshold separation are found in Fig. 4-10 (compiled in Table 4.1). The peak transconductance for the first three subbands was 67.8 nS, 29.6 nS, 16.5 nS at 1.6 K. The resulting values for the ratio $\omega_{y,p}/\omega_{x,p}$ for the subbands were: 1.7, 1.9 and 1.8, respectively. The deduced energy level separation of the QPC $\hbar\omega_{y,p}$ were found to be 20.9 meV, 4.8 meV and 3.1 meV for the first three subbands, respectively. The value for $\omega_{y,1}$ seems to be too large. A probable cause for this large value may be the rapid movement of the Fermi energy with respect to the bottom energy of the lowest subband below E_1, as shown in Fig. 4-5. The remaining values seem reasonable when compared to simulation results [65]. An independent estimate for $\omega_{y,p}/\omega_{x,p}$ can be found using Eq. 4.15. The discrepancy between the values is found to be less than 25%. This agreement is quite good when we consider the simplicity of the model.

An alternative method to estimate the subband spacing of a QPC was presented by Kouwenhoven *et al.* [3]. Measurement of the nonlinear conductance of a QPC resulted in a prediction of 3.5 meV for the first subband separation. This value was

obtained when the QPC was biased at the center of the first conductance plateau. We expect, based on the simulation results shown in Fig. 4-5, that the separation at the conduction threshold for the first subband is larger than this value. If we take the Fermi energy in our device to be 13 meV, we find, using Eq. 4.12, that the rise of the conduction band at the center of the QPC is $V_0 = 2.55$ meV. Similarly, for the second and third subband we get $V_0 = 5.8$ meV and 5.25 meV, respectively. Since the rise in the conduction at the conduction threshold of the first subband must be largest the above estimates are contradictory. This convincingly shows that the subband spacing we found at the conduction threshold of the first subband is too large. In conclusion, we argue that even though our technique of the subband separation at the conduction onset predicts too large a value for the first subband, the technique has unique advantages. Measurement of the temperature dependence of the transconductance allows estimation of the longitudinal curvatures and subband separations at the conduction onset of any subband, in contrast to a nonlinear conductance measurement which only works for the first subband. In section 4.7 we will discuss still another technique, using a perpendicular magnetic field, to obtain an estimate for the subband energy level spacing $\omega_{y,p}$.

Values for the subband energy spacing have been calculated using a two-dimensional Poisson solver [34]. The parameters for the device geometry used in the simulation were as follows: the split-gate separation was 150 nm (corresponding to the gap of device m22c4) and 195 nm, the heterointerface was located 55 nm below the surface, and the 2DEG carrier density was 3.6×10^{11} cm^2. The Fermi energy E_F, at the surface between the gates, was pinned to an energy corresponding at mid-gap of the GaAs cap layer. For the two gate separations, the resulting subband energy spacing was 2.4 meV and 1.5 meV, respectively. The value of 2.4 meV is slightly smaller when compared to the inferred values from the experimental results. This

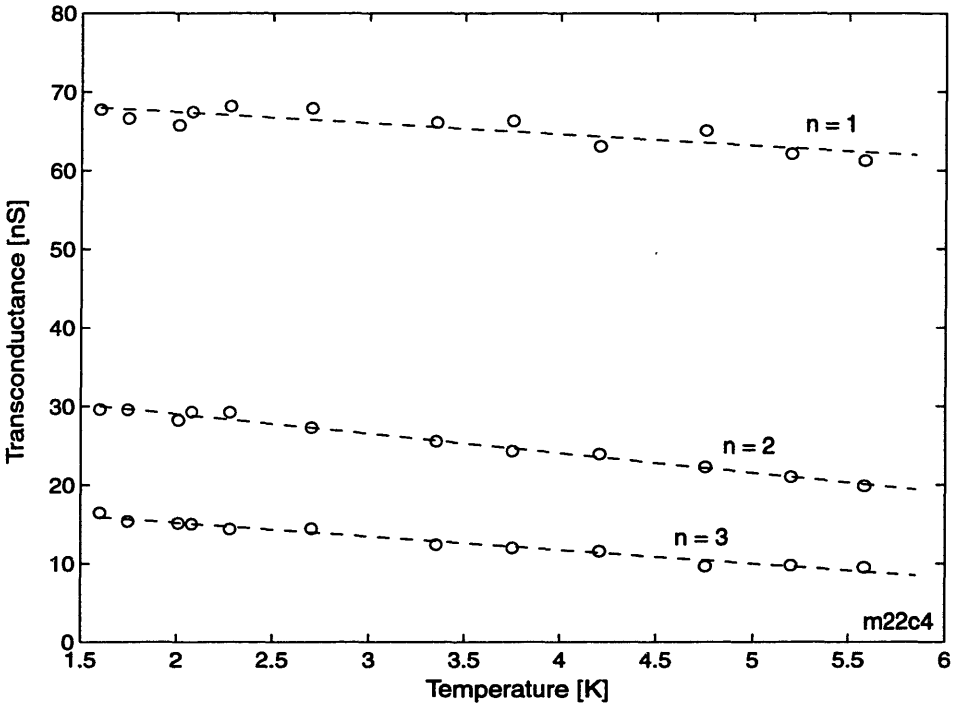

Figure 4-11: Peak values of transconductance for the first three subbands of device m22c4 measured as function of temperature. Only a small decrease is observed. We conclude that the width of the quantum conductance step width is intrinsically broader than the bath temperature in the measurement.

Table 4.1: Device characteristics summary. The quantities right of the double division line are derived quantities. Values for ratio $\omega_{y,p}/\omega_{x,p}$ are found from $I_{ds} - V_{gs}$ and g_m measurements. The following definitions have been used: $E_{x,p} \equiv \hbar\omega_{x,p}$ and $E_{y,p} \equiv \hbar\omega_{y,p}$.

Device	p	t_p	ΔV_s [mV]	ΔV_w [mV]	g_m [nS]	$\omega_{y,p}/\omega_{x,p}$ $I_{ds} - V_{gs}$	g_m	$E_{x,p}$ [meV]	$E_{y,p}$ [meV]
[a]m22c2	1	0.97	68	27		1.76			
	2	0.97	75	23		2.28			
	3	0.97	88	36		1.71			
	4	0.99	90	35		1.80			
[b]m22c2	1	0.97	89	33	127.1	1.89	1.84		
	2	1.00	90	41	41.5	1.54	1.44		
	3	0.70	93	29	22.2	2.24	2.09		
	4	0.83	93	42	13.6	1.55	1.73		
[c]m22c4	1	0.92	146	63	67.8	1.63	1.70	12.3	20.9
	2	0.93	151	46	29.6	2.32	1.85	2.6	4.8
	3	0.98	154	59	16.5	1.82	1.84	1.7	3.1
	4	0.96	143	56		1.81			

Values used in table were obtained from [a]Fig. 4-4, [b]Fig. 4-9, [c]Fig. 4-10 and [c]Fig. 4-11.

difference is not surprising, because in the simulation the Fermi energy between the gap is pinned to the Fermi energy of the 2DEG. This boundary condition means that electrons must move from the 2DEG to the surface to keep the potential constant as V_{gs} decreases. This movement of charge is unlikely at low temperatures. It is expected that the Fermi energy for the surface close to the gates is affected by the gate and a tighter confinement for the one-dimensional results. Such an increase in confinement is obtained when using the more realistic frozen surface charge density [33].

4.7 Magnetic field

An alternative method to determine the quantum point contact curvatures is to use perpendicular magnetic fields to introduce an external confinement mechanism. Experimental observation of the resulting subband depopulation was first reported by van Wees *et al.* [5]. By modeling the constriction using a saddle-point potential, the new transmission coefficient in the presence of magnetic fields can be calculated using a tunneling Hamiltonian approach [64]. In this section we will briefly review the result and analyze our experimental data.

The Hamiltonian for an electron in a saddle-point potential can be written as

$$H = \frac{1}{2m^*}(\mathbf{p} - e\mathbf{A})^2 - \mu_B \boldsymbol{\sigma} \cdot \mathbf{B} + V(x, y), \tag{4.19}$$

where $\mu_B = e\hbar/2m$ is the Bohr magneton, m^* is the electron effective mass, $\boldsymbol{\sigma}$ are the Pauli spin matrices for the spin-$\frac{1}{2}$ electron, and $\mathbf{B}$ is the magnetic field. For a magnetic field directed along the z-direction, $\mathbf{B} = B_\perp \hat{z}$, the vector potential in the symmetric gauge is $\mathbf{A} = \nabla \times \mathbf{B} = \frac{1}{2}B_\perp(-y\hat{x} + x\hat{y})$ and the spin contribution of the Hamiltonian is $\boldsymbol{\sigma} \cdot \mathbf{B} = B_\perp \hat{\sigma}_z$. In terms of the cyclotron frequency of the electron, $\omega_c = eB_\perp/m^*$, and defining $\Omega^2 \equiv \omega_c^2 + \omega_y^2 - \omega_x^2$, the following frequencies govern the transmission and reflection through the saddle-point potential:

$$\gamma_1 = \frac{1}{\sqrt{2}}\left[\left(\Omega^4 + 4\,\omega_x^2\omega_y^2\right)^{1/2} - \Omega^2\right]^{1/2} \tag{4.20}$$

and

$$\gamma_2 = \frac{1}{\sqrt{2}}\left[\left(\Omega^4 + 4\,\omega_x^2\omega_y^2\right)^{1/2} + \Omega^2\right]^{1/2}. \tag{4.21}$$

The functional form of the transmission probability is identical to Eq. 4.10 but now

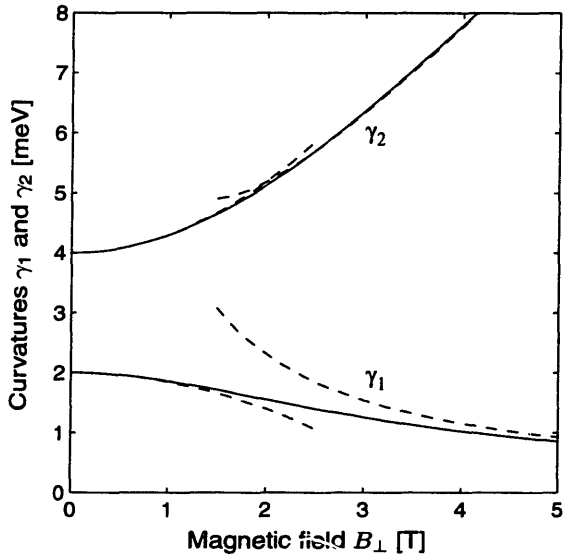

Figure 4-12: Saddle-point potential curvatures γ_1 and γ_2 plotted as function of normal magnetic field strength $B_\perp$. Low and high field approximations are shown by the dashed lines. Values for the curvatures of the potential were $\omega_x = 2$ meV and $\omega_y = 4$ meV.

includes a magnetic field dependence

$$T_n = \frac{1}{1 + e^{-2\pi\varepsilon_n}},$$

with the modified variable

$$\varepsilon_n = \left[E - V_0 + \mu_B B_\perp \hat{\sigma}_z - \hbar\gamma_2(n - \tfrac{1}{2})\right] / \hbar\gamma_1. \tag{4.22}$$

The new frequencies γ_1 and γ_2 take the position of the curvatures ω_x and ω_y in the presence of a perpendicular magnetic field. In GaAs, with $m^*/m = 0.067$, the energy separation between adjacent Landau levels is $\Delta E_L/B_\perp = 2\mu_B m/m^* = 1.73$ meV/T. Hence the magnetically induced energy scale is on the order of a few meV, which is comparable in magnitude to values shown in Table 4.1. The energy splitting associated with the spin-up and spin-down electrons is $\Delta E_\sigma/B_\perp = 2\mu_B = 0.116$ meV/T.

In Fig. 4-12 we have plotted the frequencies γ_1 and γ_2 as a function of the magnetic field $B_\perp$ (solid lines). We set the zero field values $\gamma_1 = \omega_x$ and $\gamma_2 = \omega_y$, equal to 2 meV and 4 meV, respectively. A ratio of $\omega_y/\omega_x = 2$ is typical for our quantum

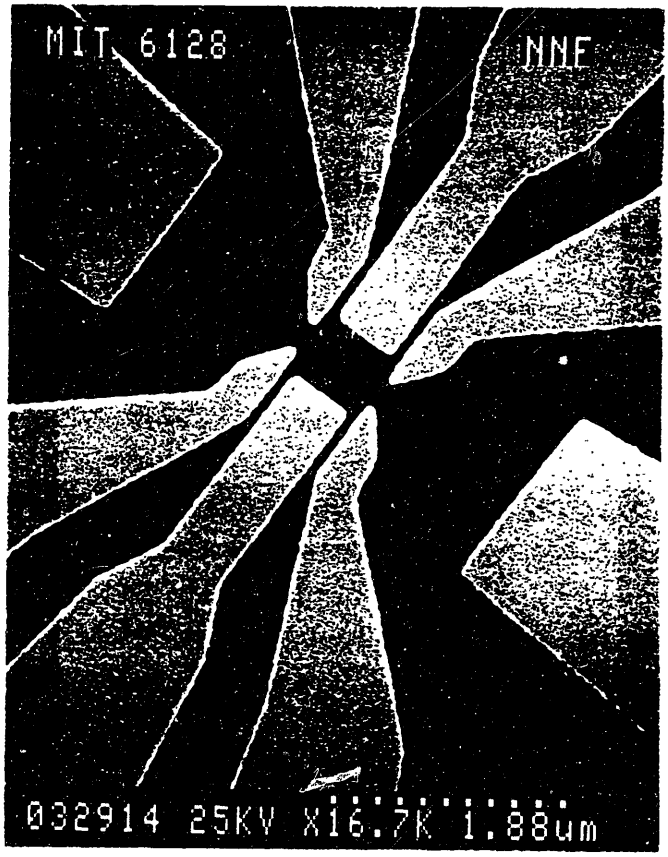

Figure 4-13: SEM photograph of quantum dot. Current transport takes place along a direction from top to bottom. The width of both constrictions was 0.22 μm. Square center region is 0.78 μm long and 0.54 μm wide. By convention, the opposite gate pairs are called A and B and numbered sequentially from top to bottom. All six gates can be biased independently but usually the A/B pairs are ties together.

point contacts. We find that variations in γ_1 are small for magnetic field values up to 5 T. On the contrary, the value of γ_2 increases rapidly for magnetic field values larger than about 2 T. We therefore expect that the complicated expressions for γ_1 and γ_2 simplify for small and large values of the magnetic field. Such limiting expressions will help facilitate the analysis of data. For small magnetic field we found

$$\gamma_1^{\text{low}} \approx \omega_x \left[1 - \frac{\omega_c^2}{2(\omega_x^2 + \omega_y^2)}\right] \tag{4.23.a}$$

$$\gamma_2^{\text{low}} \approx \omega_y \left[1 + \frac{\omega_c^2}{2(\omega_x^2 + \omega_y^2)}\right], \tag{4.23.b}$$

and for large magnetic fields:

$$\gamma_1^{\text{high}} \approx \frac{\omega_x \omega_y}{\omega_c} \tag{4.24.a}$$

$$\gamma_2^{\text{high}} \approx \omega_c \left[1 + \frac{\omega_y^2 - \omega_x^2}{2\omega_c^2}\right]. \tag{4.24.b}$$

We find that at high magnetic fields the transverse confinement of the saddle-point potential become unimportant compared to the magnetic confinement energy. The energy level structure in the constriction is therefore determined by only the magnetic field. The transmission coefficient is likewise determined by only the magnetic field. Plots of these limiting expressions for γ_1 and γ_2 are shown in Fig. 4-12 (dashed lines). With an understanding of the behavior of the transmission coefficient as a function of the magnetic field, we are now ready to do experiments.

The split-gate design we used in the magnetic field experiments are shown in the SEM micrograph Fig. 4-13. The design includes two narrow short constrictions and one long wide constrictions. Figure 4-14 and Fig. 4-15 show the quantum point contact behavior as function of the magnetic field. In the first plot the magnetic field varies from zero to 2 T in steps of 0.3 T. At zero field the data is relatively noisy and the stair-case structure is barely visible. For increasing values of the magnetic field,

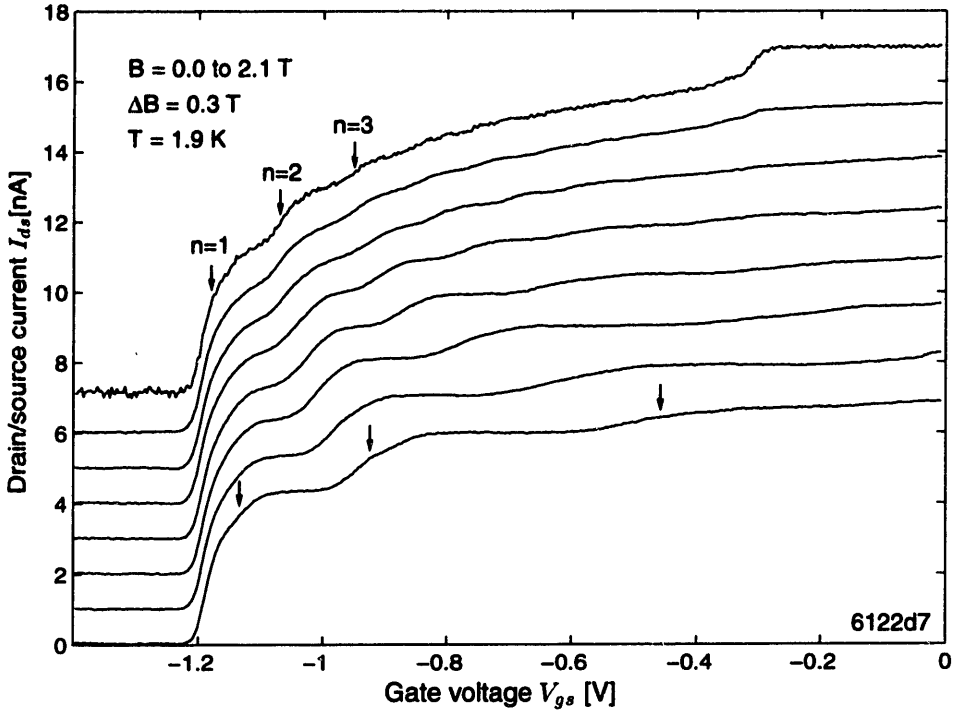

Figure 4-14: Drain/source current I_{ds} as a function of the gate voltage V_{gs} for QPC device 6122d7 (A/B3). Plot covers magnetic field values from zero to 2.1 T in steps of 0.3 T starting with the lowest field measurement from the top. The first three subbands are marked with arrows for the lowest and highest field scan. Large shifts in the subband onsets are observed as the magnetic field is increased. Contribution to conduction from spin-up electrons are indicated with $\uparrow$ and spin-down electrons with $\downarrow$. The noise on the curve is due the absence of low-pass filtering during data acquisition. Curves are vertically offset by 1 nA for clarity.

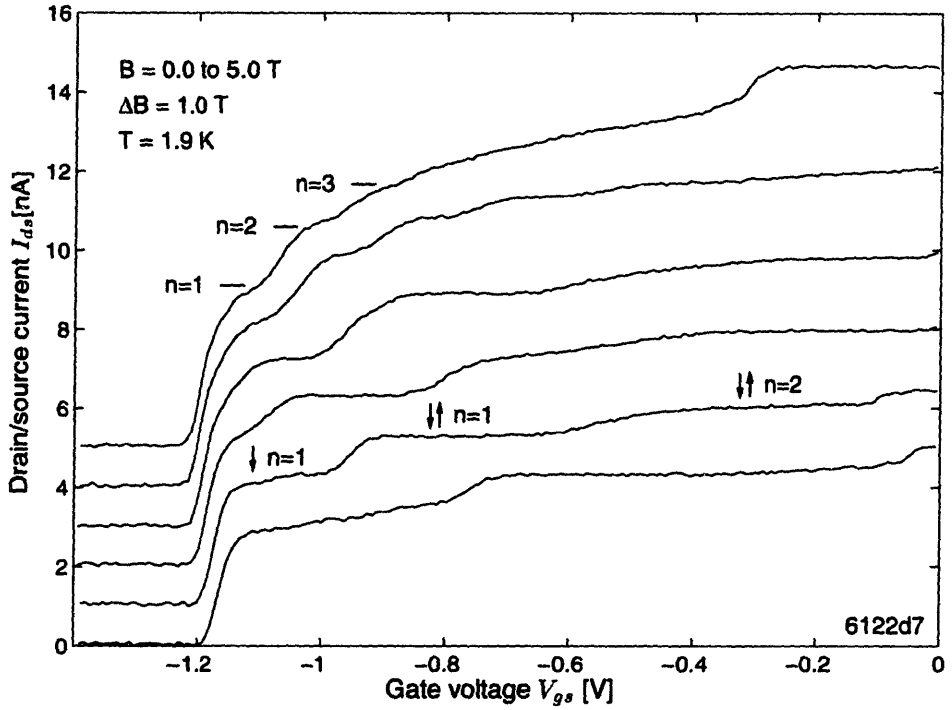

Figure 4-15: Drain/source current I_{ds} as function of gate voltage V_{gs} for QPC device 6122d7 (A/B3). Plot covers magnetic field values from zero to 5 Tesla in steps of 1 T starting with the lowest field measurement from the top. Subband splitting due to electron spin is indicated; electrons with their spin oriented antiparallel to the applied magnetic field start to contribute to the current at lower values of the gate voltage. Curves are vertically offset by 1 nA for clarity.

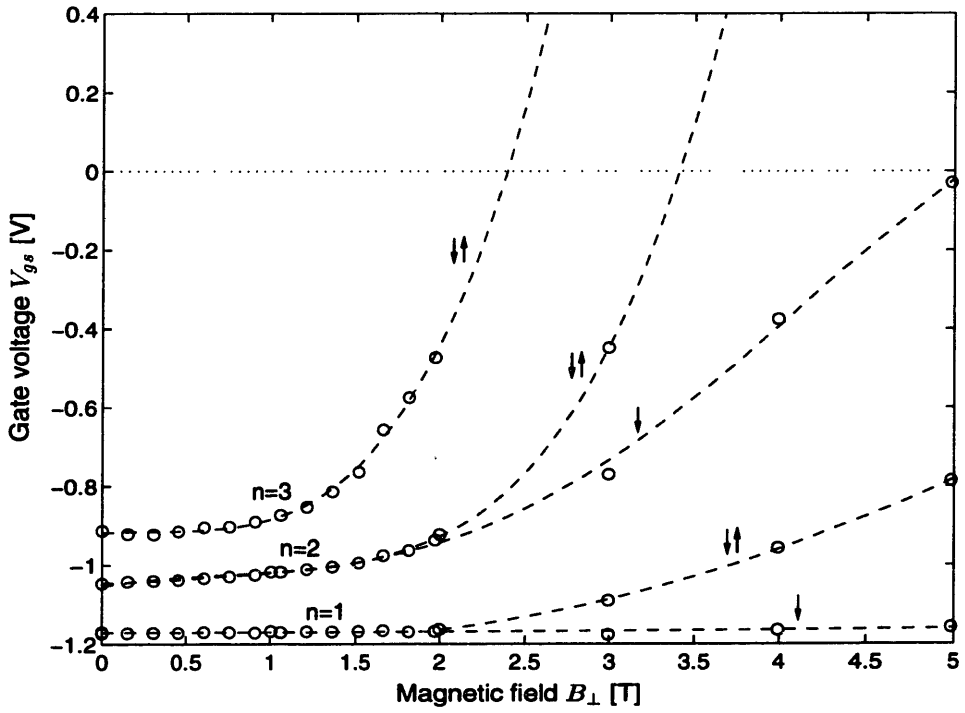

Figure 4-16: Subband threshold position in gate voltage for spin-up and spin-down electrons as function of perpendicular magnetic field $B_\perp$. Data extracted from Fig. 4-14 and Fig. 4-15 (circles). Interpolated movement of subband threshold positions indicated by the dashed lines.

we notice a movement of the subband onset threshold voltage. This is a consequence of the increase in the effective transverse confinement because of the magnetic field. This increased confinement increases the subband energy spacing since the value of γ_2 becomes greater. In the second plot, the magnetic field varies from zero to 5 T in steps of 1 T. A split is observed in the conductance steps of the first two subband for magnetic field values in excess of ~3 T. This separation is caused by the lifting of the spin degeneracy ($\Delta E_\sigma \approx 0.12 \times 3 = 0.36$ meV).

In Fig. 4-16 we have replotted the subband threshold positions in gate voltage as a function of the perpendicular magnetic field $B_\perp$. The plot convincingly illustrates both the shift of the subband thresholds and the split of the subbands due to electron

spin interaction with the magnetic field. The dashed lines are polynomial best fits to the data points and are helpful for guiding the eye. There are two features of the data we are going to discuss in detail: (1) For $n = 1$ a split in the subband due to electron spin interaction is observed, but the threshold voltage for the spin-down electron subband remains constant. Based on Eq. 4.22, we would expect this threshold voltage to increase in proportion to the magnetic field. We propose that this pinning is caused by the rapid dependence of the Fermi energy with respect to the bottom of the first subband, see Fig. 4-5. (2) For $n = 2$ and 3 the threshold voltages shift for both spin-down and spin-up electron subbands. The crossover from a constant value to a rapid increase of the threshold voltage occurs at about 1.5 T and 1 T for subbands $n = 2$ and 3, respectively. This means that $\omega_{y,3}$ is smaller than $\omega_{y,2}$ but both are on the order of 2 meV.

Analytical determination of ω_x and ω_y is impossible since no functional relationship can be found between the gate voltage and the energy levels of a quantum point contact as function of the magnetic field. Although Kaplan and Warran [70] suggested an approach which arrives at such a relationship, they had to resort to a mixture of one-dimensional and two-dimensional arguments. We will not attempt to pursue such arguments since self-consistent simulations are required to predict satisfactorily the complicated interrelationship between ω_x, ω_y and V_0 and the gate voltage V_{gs} [65, 71].

4.8 Summary

The quantized conductance of a quantum point contact has been explained by the wave-like behavior of electrons. Electron propagation through narrow constrictions was found to occur through subbands satisfying the transverse boundary conditions imposed by the electrostatic potential. Conduction through these subbands manifests itself as quantized conductance steps. A saddle-point potential model has been

introduced in order to describe the detailed behavior at the threshold of conduction for a subband. Based on reasonable assumptions about the behavior of the saddle-point potential as a function of V_{gs}, a model has been obtained for the QPC relating V_{gs} to the conductance G. With the help of this model, transconductance data has been explained. A figure-of-merit for a QPC has also been introduced, $\omega_{y,p}/\omega_{x,p}$, and related to experimentally measurable quantities. Results of analysis of measured data from two devices are summarized in Table 4.1. In addition, we measured the magnetic field dependence of the subband threshold voltage. Based on the threshold shifts, we estimated the curvature ω_y for subbands $n = 2$ and 3 to be approximately 2 meV. The absence of a shift of the threshold voltage for the first subband was explained by the rapid movement of the Fermi energy versus the gate voltage when the one-dimensional channel was fully depleted.

Chapter 5

Photo-response of quantum point contact

5.1 Introduction

This chapter presents the experimental measurements and analysis of a quantum point contact's (QPC) photo-response. The photovoltaic effect of a QPC has been analyzed by Hekking and Nazarov [72]. In a extensive treatment by Hu and Feng [15, 73], the possibility of energy absorption by ballistic electrons from a time-oscillating QPC potential was explored. They found, for example when a QPC is biased below pinch-off (no propagating modes), the electrons from either electron reservoir separated by the QPC could be excited into the lowest propagating mode through the channel. This propagation leads to a finite current flow in the presence of the radiation field. The onset of this current was predicted to be dependent on the radiation frequency, while higher order photon absorption leads to a characteristic step structure in the device conductance plot [15]. This step structure resembles the response of a superconductor-insulator-superconductor device in the quasi-particle tunneling cur-

rent [32]. These early predictions of the radiation response in a QPC have not yet been observed. Experimental findings of the radiation response of a QPC are presented in this chapter. Section 5.2 describes the experimental system and present measurement results of a QPC with a transverse coupled log-periodic antenna. The analysis of the data based on one-dimensional thermopower generation is presented in section 5.3. The theoretical predictions of the current responsivity are extended to finite bias voltage in section 5.4. A radiation-induced current measurement using a QPC with a longitudinal coupled bow-tie antenna is then discussed. The results of this chapter are summarized in section 5.5.

5.2 QPC with gate coupled antenna

In the first set of experiments a QPC was used in which the ac electric field was oriented transverse to the direction of the electron transport. The split-gates defining the channel constriction were used simultaneously for both depletion of the 2DEG and as antenna terminals. An SEM micrograph of the device geometry is shown in Fig. 4-1.

The measurements were performed in a cryostat in which the device was submerged in liquid helium [56]. In this cryostat, the device was cooled down to 1.6 K by pumping the helium bath. The far-infrared radiation was coupled into the cryostat through an optical access port covered with quartz windows and a low-pass black polyethylene filter. These two elements were used to block both the visible and near-infrared radiation. Blocking the visible light from entering the cryostat was essential to prevent electron-hole generation and hence alter the 2DEG electron concentration during the measurement. We found that stray light entering the cryostat caused erratic results when we were measuring device characteristics. Inside the cryostat, a 0.85 inch focal length TPX was mounted in front of the substrate to focus the radi-

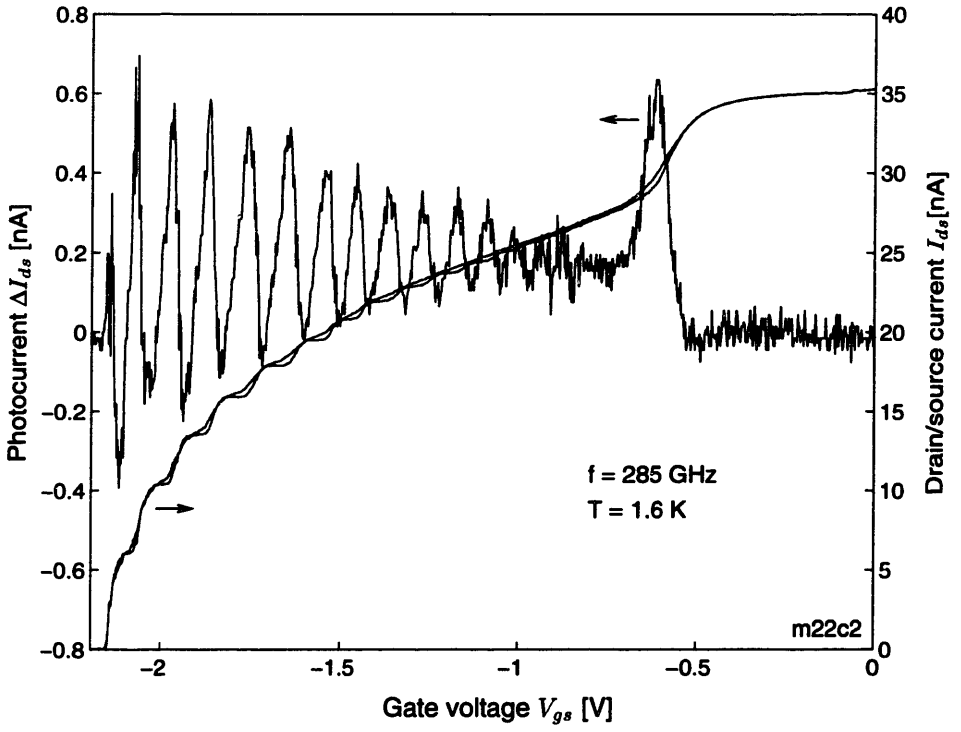

Figure 5-1: Dc drain/source current I_{ds} for quantum point contact m22c2 as a function of the gate voltage V_{gs} (right ordinate). The difference between a pair of measurements with and without the 285 GHz radiation, ΔI_{ds}, is also shown (left ordinate).

ation. The converging radiation was then incident on the substrate from the device side. A log-periodic antenna was used to couple the radiation into the QPC. The coupling efficiency in this arrangement was not optimal since the radiation beam efficiency is low into the air side of a planar antenna mounted on a dielectric substrate. The coherent radiation, polarized in the direction of the axis of the log-periodic antenna, was generated by a Gunn oscillator [52]. This radiation source supplied ample power ($\sim$1 mW) to generate observable signals in the QPC. Higher frequency bands were available when using a frequency trippler [53] or a far-infrared laser [54].

Figure 5-1 shows the result of a radiation experiment at 285 GHz. A QPC was biased with a $V_b = 100$ μV voltage source with a $R_l = 1$ kΩ load resistor. The

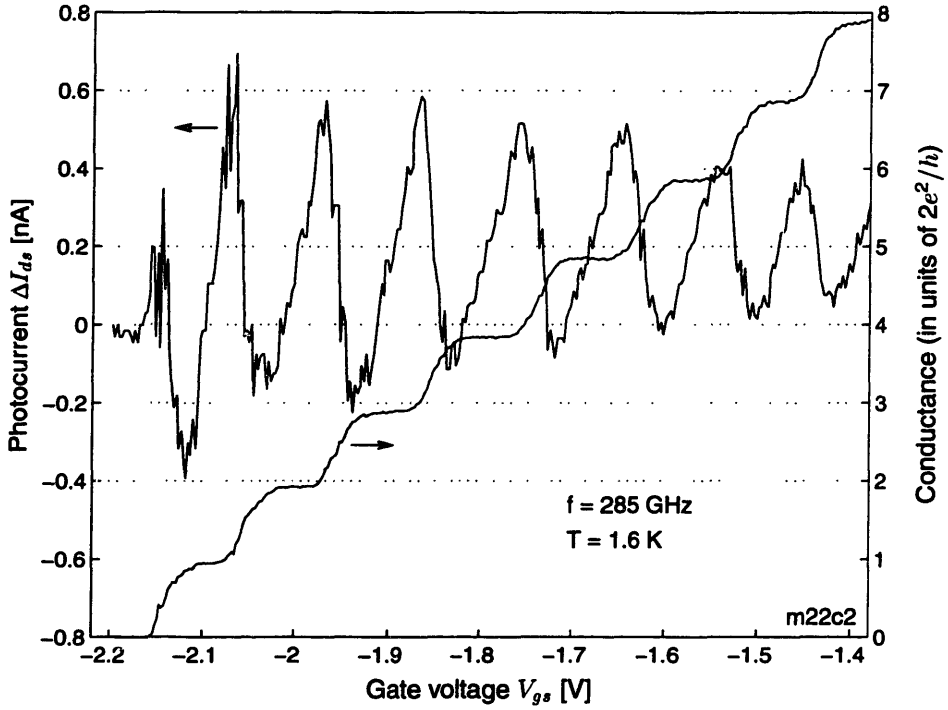

Figure 5-2: Photo-induced current ΔI_{ds} in a gate voltage region where the conductance steps (measured without radiation at 1.6 K) are well defined. The peak-to-peak amplitude of the photoinduced current is about 0.5 nA, and its average value is 0.2 nA.

dc drain/source current I_{ds} was measured while stepping the gate voltage V_{gs} in increments of 3 mV. At each value of V_{gs}, a measurement was performed of I_{ds} with and without radiation. We used a solenoid driven shutter to block the radiation in the vicinity of the optical access port. The radiation predominantly increases I_{ds} and as a result, the sharp step structure of the QPC is rounded. We have numerically calculated the difference between the two measurements, which we define as the radiation-induced current ΔI_{ds}. The difference shows an oscillatory behavior, and the peak appears to coincide with the onset of conduction for the subbands. A large response is also seen in the 2D to 1D transition regime.

In order to look for the predicted radiation-induced ministeps, we replot in Fig. 5-2 an expanded view of ΔI_{ds} and the drain/source conductance G_{ds} as functions of the gate voltage in a range where the conductance steps are well-defined. The ministep structure is expected to be distinctive at 285 GHz. The photon energy is 1.18 meV and the subband energy spacing for the device is on the order of a few meV at the conduction threshold for the lowest steps. The ministeps should have a width of about $\frac{1}{3}$ that of the conductance steps. We find that no ministeps are observed in the measurement. The same experiment was performed at several other frequencies showing a similar response, see Fig. 5-3. The features in the QPC response did not appear to depend on the frequency of the radiation, although the polarity of ΔI_{ds} was reversed when using 118.8 μm radiation.

One likely cause of the observed radiation-induced ΔI_{ds} is the heating of electron gas by far-infrared radiation. The absorbed radiation energy increases the temperature of the electron gas, which broadens the Fermi surface and produces additional drain/source current. To illustrate this mechanism, we have plotted in Fig. 5-4 the difference in the drain/source currents taken at 3.7 K and 1.6 K as a function of the gate voltage. A behavior similar to that shown in Fig.5-1 is observed. We

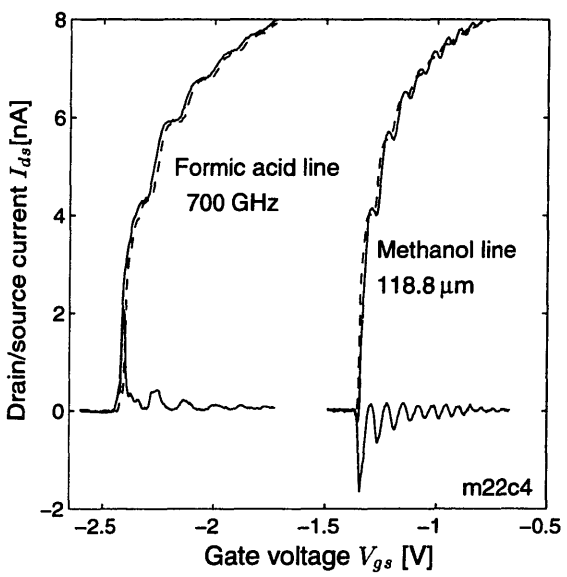

Figure 5-3: Response of QPC m22c4 when irradiated with 700 GHz and 118.8 μm radiation. The numerically calculated difference in I_{ds} measured with (solid line) and without (dashed line) illumination shows an oscillatory behavior. The difference is predominantly positive for the 700 GHz radiation and negative for the 118.8 μm radiation. The device's threshold voltage has shifted almost 1 V, a shift that frequently occurs when the device is thermally cycled. The liquid helium bath temperature in both measurements was 1.6 K.

find that a temperature difference of $\Delta T = 2.1$ K results in an additional current of 5.7 nA at the onset of the first subband. The magnitudes of the observed radiation-induced currents at 285 GHz are approximately 0.5 nA. A temperature rise of $\Delta T = 2.1 \times (0.5/5.7) = 180$ mK would be sufficient to explain the increase in I_{ds}. An increase of the electron temperature on the order of 100 mK because of radiation is plausible based on measurements of the thermal broadening of the Shubnikov-de Haas oscillation peaks [74].

In the following experiments we measured the radiation-induced current when the device biasing voltage was set to zero. At zero bias, the current due to symmetric heating of the electron reservoirs should be zero. In Fig. 5-5(b) we show the radiation-induced current ΔI_{ds} measured with a zero external bias voltage V_b. Using a lightpipe the 285 GHz radiation was guided directly toward the source side of the antenna. Trace (a) shows I_{ds} measured with $V_b = 300$ μV and without radiation. Comparing the curves (a) and (b), it is clear that the peaks in the radiation-induced current coincide with the onsets of the subbands.

In Fig. 5-6 we have measured the photocurrent ΔI_{ds} as the power of the incident

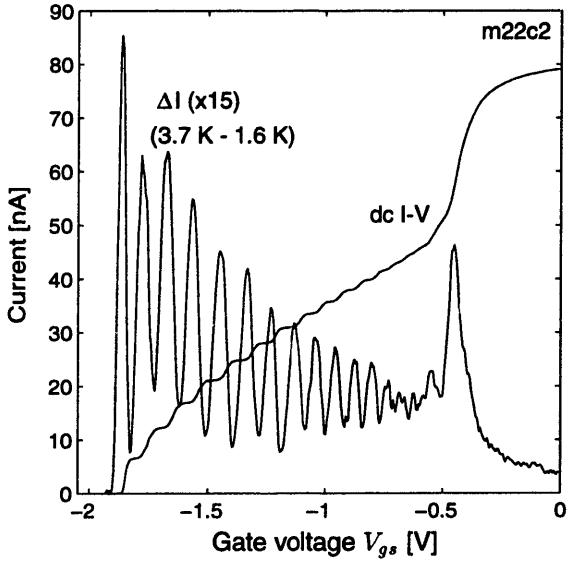

Figure 5-4: Thermally induced drain/source current ΔI_{ds} (shown here as the difference between a measurement at 3.7 K and 1.6 K plotted as a function of the gate voltage. The increase in drain/source current, ΔI_{ds}, has been multiplied by 15× for visibility. For reference the dc I_{ds} measured at a temperature of 1.6 K is also shown.

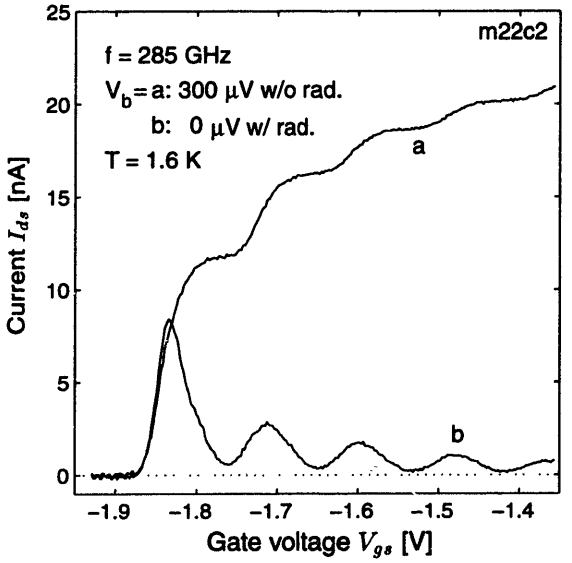

Figure 5-5: (a) Drain/source current I_{ds} of quantum point contact m22c2 with $V_b = 300$ μV and $R_l = 10$ kΩ. (b) Photoinduced current when irradiated with 285 GHz radiation when $V_b = 0$.

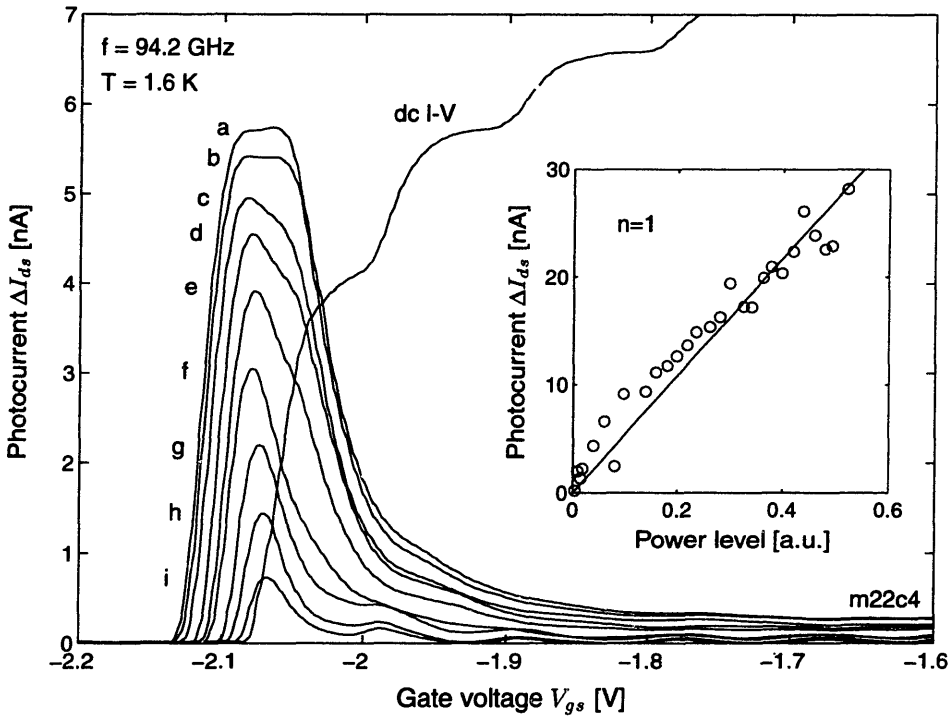

Figure 5-6: Radiation-induced current ΔI_{ds} plotted as a function of power level (arbitrary units) for 94.2 GHz radiation. The relative power levels for measurements (a) through (i) were 0.324, 0.279, 0.235, 0.218, 0.180, 0.096, 0.059, 0.038, and 0.018. The dc $I_{ds} - V_{gs}$ characteristic was measured using a bias voltage of 30 μV and a load resistance of 10 kΩ. The bath temperature was 1.6 K. Inset shows peak photoinduced current $\Delta I_{ds}^{\text{peak}}$ for the first subband as function of radiation power level.

radiation is increased. At low power levels, separate peaks are apparent at each subband conduction onset. For high power levels, the contribution from the first subband dominates and the separate peak structure has disappeared. We reason that when the thermal broadening of the Fermi distribution is on the order of the intersubband spacing, the separate peak structure disappears. The inset show the peak current at the threshold of the first subband. Over a wide range of input power we found the peak height increases linearly with the incident power level. We will estimate the order of magnitude of the absorbed radiation power in section 5.3.

Another important feature was the possibility to reverse the direction of the cur-

rent flow. The radiation was guided with a lightpipe towards the cryostat access window. By small angle rotation of the dewar with respect to the lightpipe, it was possible to selectively couple more radiation into either the drain or the source. Figure 5-7 shows the ΔI_{ds} under different illumination schemes. The top four $\Delta I_{ds} - V_{gs}$ curves were taken at different radiation power levels with $V_b = 0$. The four lower curves were taken under the same conditions, but with the far-infrared beam shifted from the source to the drain by adjusting the lightpipe appropriately. We found that an approximately equal magnitude of ΔI_{ds} could be generated for both polarities for a given power level. As seen earlier, the current also scales linearly with the incident radiation power. In order to compare the spacing of the current peaks, the horizontal axis has been offset by the threshold voltage V_t, defined as the gate voltage at the onset of conduction for the first subband. The lower curves are almost identical to the top ones, but are of opposite polarity. By placing the far-infrared beam in the middle, we can nearly null ΔI_{ds}. The reversibity of its polarity is convincing evidence that the signal is caused by thermopower.

Since the polarity of the radiation-induced current could be reversed by merely controlling the angle of incidence of the radiation we concluded that ΔI_{ds} was caused by imbalanced heating of the electrons in the drain and source reservoirs. This heating was accomplished by the ac voltage produced between the antenna terminals. The strength of this voltage could, in principle, be different on the drain and source sides of the QPC if the antenna terminals themselves allowed a voltage drop due to finite conductivity in the metal layer used to make the antenna. Since the metal thickness of the antenna terminals close to the QPC is only about 180 Å, this finite resistance of the antenna results in nonideal behavior in the region of the mesa. Unequal strength of the ac voltage results in an imbalanced heating of the electron reservoirs.

The next section develops a theoretical framework for the dissipation of radiation

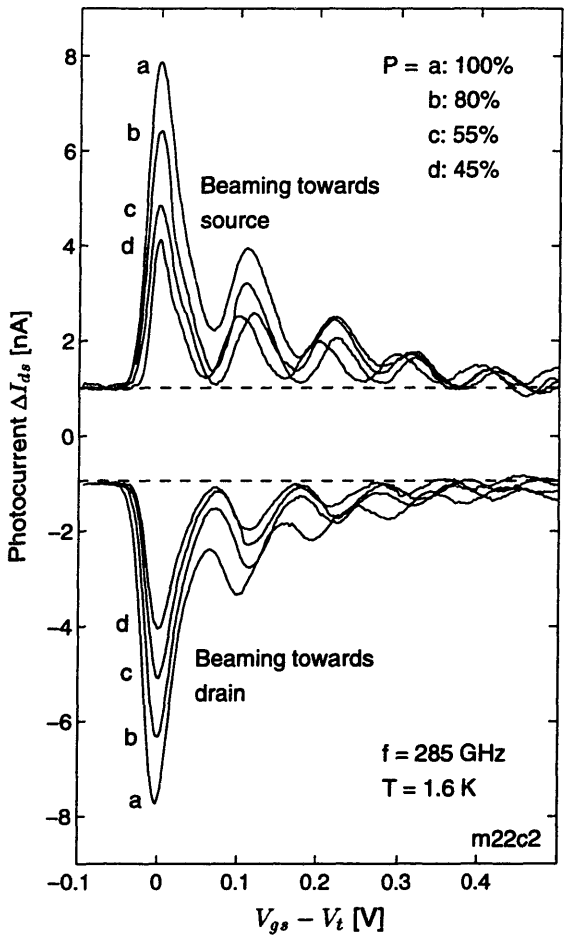

Figure 5-7: Photoinduced current of quantum point contact m22c2 measured at low radiation power levels with zero drain/source bias. The polarity of the current can be reversed by controlling the angle of incidence of the radiation. The signal was positive when the radiation was guided towards the source side, and negative when guided towards the drain side. For visibility the peaks of the first subband for all the measurements have been aligned by subtracting the threshold voltage V_t from the gate voltage. The measurements for the two polarities have been vertically offset by ± 1 nA.

in the QPC. The reasoning of early theoretical work done by [Streda] for estimating the thermopower in a QPC was followed. By comparing this model with our measurements, a good understanding of the radiation absorption in a QPC with a gate coupled antenna was obtained.

5.3 Quantum oscillations of thermopower

In the case of insufficient confinement of the ac electric field the efficiency of the modulation quanta absorption decreases rapidly. Instead, the ac electric field causes heating of the electrons in the 2DEG. Modeling of the thermopower in a QPC has been done by [Streda, van Houten], who calculated the thermal voltage produced across an open-circuited QPC. Measurements establishing this thermopower effect have been observed by [Molenkamp] using a dc current to heat one side of the QPC. Our derivation of the thermopower closely follows these initial treatments, except we included a finite load resistor which is required for the measurement of the thermopower signal. This alteration was important for purposes of modeling the observed data.

Figure 5-8 illustrates the mechanism that generates thermopower signals in a one-dimensional electron system. In this diagram, we have selected a condition in which the electro-chemical potentials are in the vicinity of the conduction threshold of the second subband. Assuming the electron temperature in the drain is higher than the source, a net current will flow from the source to the drain, caused by the excess electrons in the drain above the conduction threshold for the second subband. It is clear from Fig. 5-7 that features in the thermopower signal are due to rapid changes of the transmission coefficient $T(E)$. We should expect a peak in the thermal current at the onset of each subband, where $T(E)$ changes rapidly.

To calculate the total current in our device, we made the following simplifying

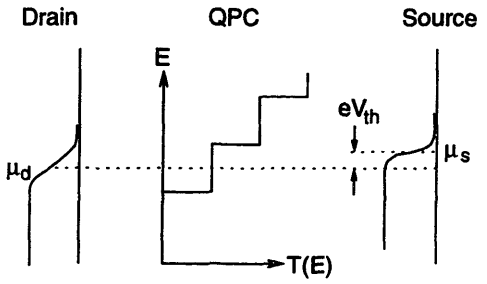

Figure 5-8: Illustration of electrons contributing to thermopower current.

assumptions: (1) temperatures T_d and T_d can be assigned respectively to the electrons in the drain and the source which participate in ballistic transport through the QPC; (2) the total transmission is $t(E) \equiv \sum_n t_n(E)$, where $t_n(E)$, the transmission coefficient for subband n, is taken as the unit step function$\theta(E - E_n)$; and (3) the ratio ω_y/ω_x for the curvature of the QPC remains constant. The current through a QPC is then given by

$$I_{DS} = \frac{V_b - V_{ds}}{R_l + 2R_c} = \frac{1}{eR_q} \sum_n \int_{-\infty}^{\infty} t_n(E) \times [f(E - \mu_s; T_s) - f(E - \mu_d; T_d)]\, dE, \tag{5.1}$$

where $R_q \equiv h/2e^2 \approx 13$ kΩ, R_l is the load resistance, R_c is the resistance for each ohmic contact, $f(E;T) = [1 + \exp(E/k_BT)]^{-1}$ is the Fermi function, and the chemical potentials of the 2DEG are $\mu_s - \mu_d = eV_{ds}$. In order to calculate the current I_{ds} due to a difference between T_d and T_d, Eq. 5.1 must be solved self-consistently, since both sides depend explicitly on V_{ds}. In Fig. 5-9 we have used Eq. 5.1 to calculate the height of the thermopower signal (thermal voltage and thermal current) for a single one-dimensional (1D) subband. In the calculation the temperatures were $T_d =$ 1.6 K and $T_s = 1.61$ K. The curves (b) and (d) correpond to the signals expected at the conduction threshold of the subband. The curves (a) and (c) represent the peak thermal voltage and current generated. This peak occurs below the conduction threshold of the subband and depends on the external resistor (sum of $R_l + 2R_c$).

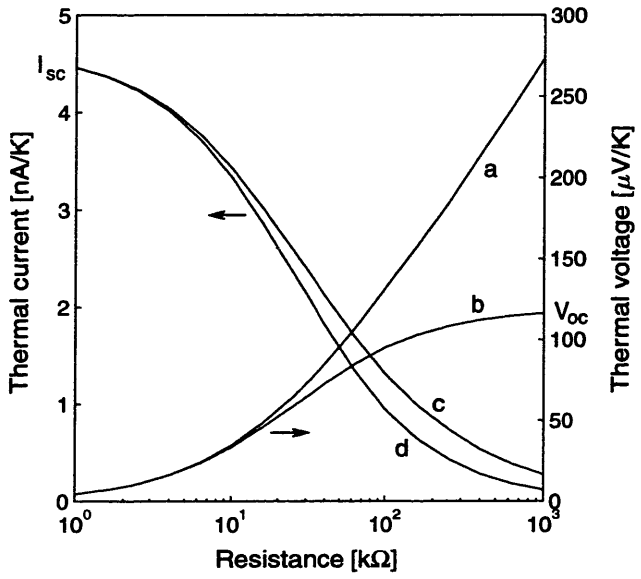

Figure 5-9: Peak thermal response predicted for first subband as function of finite load resistance. (a) and (c) are the peak thermal voltage and current for a 1 K temperature difference between the source and drain. (b) and (d) are the thermal voltage and current at the threshold of the first subband, V_t. Notice that the peak thermal voltage and current does not take place at V_t. I_{sc} is the short-circuit thermal current, 4.5 nA/K, and V_{oc} is the open-circuit thermal voltage, 120 μV/K, at V_t.

The shift of the peak thermal voltage V_{th} to below the subband onset E_t for large external resistances R_{ext} can be illustrated with the following example: let $T_d = 0$ K, T_s remains finite, and fix μ_d at the conduction onset E_t of the 1D subband. For a zero external resistance we have $\mu_s = E_t$ and the current is maximized. As R_{ext} increases, μ_s must decrease such that $V_{\text{th}} = R_{\text{ext}} I_{\text{th}}$ is satified. This decreases μ_d and causes the shift in curve (a) with respect to (b). The difference between the peak thermal voltage and the thermal voltage at the conduction onset of the 1D subband can be significant for large R_{ext}. In our measurements we were using either $R_l = 1$ kΩ or 10 kΩ which corresponds to a domain where the curves are approximately the same.

However, when the differential heating $\delta T_{ds} \equiv T_d - T_d$ is small compared to the intersubband spacing ΔE_n, we can use a linear approximation of Eq. 5.1 [Streda].

(a) Electrical circuit

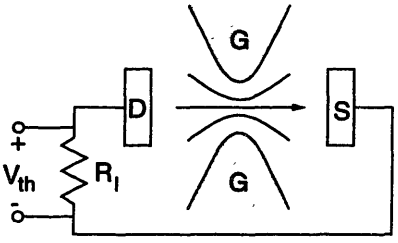

(b) Thermal circuit

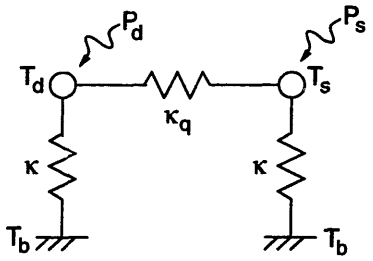

Figure 5-10: (a) Electrical circuit model; (b) thermal circuit model.

The peak currents $I_{ds}^{\text{peak}}(n)$ at the onset of each subband n, with $V_b = 0$, are given by the following expression:

$$I_{ds}^{\text{peak}}(n) = \frac{S_1 \Delta T_{ds}/2}{R_q + (R_l + 2R_c)(n - 1/2)}, \tag{5.2}$$

where $S_1 = 2\ln 2\ k_B/e \approx 120\mu V/K$ [75]. Using Eq. 5.2, we have indicated the envelope of the calculated $I_{ds}^{\text{peak}}(n)$ in Fig. 5-11(a) (dash-dotted curve). To match the peak current at the first subband we used a temperature difference of $\Delta T_{ds} = \pm 2.3$ K. The calculated result clearly shows a slower roll-off of $I_{ds}^{\text{peak}}(n)$ at higher subbands compared to the data.

We propose that the faster decrease in the measured $\Delta I_{ds}^{\text{peak}}(n)$ is caused by a decrease of the temperature difference ΔT_{ds} at higher subbands. Previous investigations revealed that the Wiedemann-Franz law is valid for thermal conduction of electrons through QPCs [Molenkamp2,Houten]. Thus when the differential power dissipation in the drain and source ΔP_{ds} is held constant, the temperature difference ΔT_{ds} should

decrease at higher subbands since the higher electrical conductance results in a higher thermal conductance. Figure 5-10(b) illustrates the three heat flow paths for the electrons in the drain and source reservoirs. Considering the energy balance of the model, the following two equations must be satisfied:

$$P_d = -\kappa_q \Delta T_{ds} + \kappa(T_d - T_b) \tag{5.3.a}$$

$$P_s = -\kappa_q \Delta T_{ds} + \kappa(T_s - T_b) \tag{5.3.b}$$

where the thermal conductance of the QPC, $\kappa_q = L\overline{T}_{ds}(n-1/2)/R_q$, is related to its electrical resistance using the Wiedemann-Franz law; $L = 2.44 \times 10^{-8}$ WΩ/K^2 is the Lorentz number; $n = 1, 2, \ldots$ is the subband number. The average temperature of the drain and source electrons has been identified as $\overline{T}_{ds} = (T_d + T_s)/2$, which is to be independent on n in this linear model; and κ is the thermal conductance between the 2DEG in the drain and the source to the bath. There are two thermal conduction mechanisms to the bath: electron-phonon scattering involving energy transfer and electronic conduction through the ohmic contacts.

Solving Eq. 5.3.b above for the differential temperature of two electron reservoirs at the threshold of the n-th subband results in

$$\Delta T_{ds}(n) = \frac{\Delta P_{ds}}{\kappa + 2L\overline{T}_{ds}(n-1/2)/R_q}. \tag{5.4}$$

We can rewrite Eq. 5.4 to obtain $1/\Delta T_{ds}(n) = A + B(n-1/2)$, where $A = \kappa/\Delta P_{ds}$ and $B = 2L\overline{T}/\Delta P_{ds} R_q$. To establish the validity of the proposed model, we looked for a linear relationship between $1/\Delta T_{ds}$ and n, from which we could deduce numerical values for both the differential power dissipation ΔP_{ds} and the thermal conductance κ. In Fig. 5-11(b) we have plotted this relationship between the inverse differential temperature versus the subband number. $1/\Delta T_{ds}(n)$ is found to increase linearly with

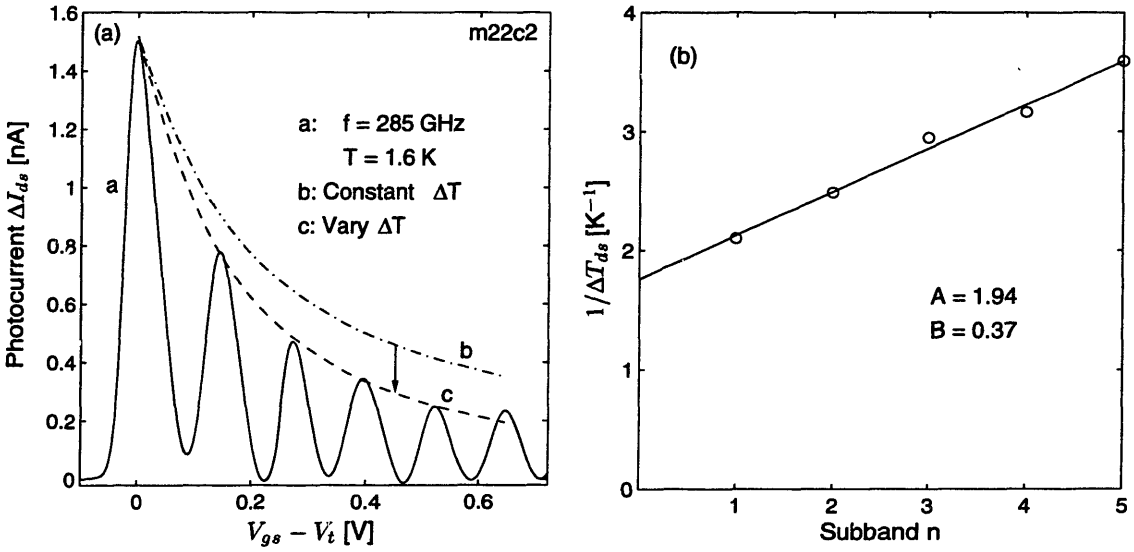

Figure 5-11: (a) Curve a is photo-induced current ΔI_{ds} produced by 285 GHz radiation. Curve b is peak ΔI_{ds} decay envelope predicted by a QPC model assuming a constant difference between the drain and the source electron temperatures. Curve c is peak ΔI_{ds} decay envelope predicted by a QPC model taking account of thermal contact between the drain and the source electron reservoir. (b) The inverse temperature difference ΔT_{ds}^{-1}, calculated using the data shown in (a), is plotted as a function of the subband number n.

respect to n, up to $n = 5$. Deviations from the linear behavior are observed at higher subbands. From the data, $\Delta T_{ds} \approx 0.5$ K at the first subband. From the slope B, the differential power dissipation ΔP_{ds} was 1.9×10^{-11} W for $\overline{T}_{ds} = 1.85$ K. From the value of $A = 1/\Delta T_{ds}(n = 1/2)$, $\kappa = 3.7 \times 10^{-11}$ W/K. Note that this $\overline{T}_{ds}$ corresponds to the extreme case in which $T_s = T_b$, and $T_d = T_b + \Delta T_{ds}$. This case sets the lower limit for ΔP_{ds} and κ.

The thermal conductance per unit area between a 2DEG and a bath due to electron-phonon scattering has been shown to take the form $\kappa_{\text{e-ph}}/\text{area} = 3\alpha n_{2\text{D}} T^2$ at $T \geq 2$ K, where α has been calculated to be 4×10^2 eV/sK^3 for $n_{2\text{D}} = 2.8 \times 10^{11}$ cm^{-2} [76]. Thus $\kappa_{\text{e-ph}}/\text{area} \approx 2 \times 10^{-12}$ W/K $\cdot\mu$m^2 at $T = 2$ K. If our deduced $\kappa = 3.7 \times 10^{-11}$ W/K is mainly due to electron-phonon scattering, the "hot spot's" effective area is approximately 20 μm^2. Its length (4-8 μm depending on mode structures) is comparable to the inelastic scattering length l_ϕ at these temperatures. This coincidence suggests that the hot electrons are located within l_ϕ from the center of the QPC. Because only electrons in this region participate in the ballistic transport through the QPC, the above coincidence justifies the use of a single temperature in the source and the drain in our calculations. Since the hot spot is much smaller than the area of the 2DEG in the drain and source ($\sim$500 μm^2), we conclude that electron-phonon scattering, not electronic conduction through the ohmic contacts, is the dominant heat conduction mechanism.

Finally, we have calculated the envelope of the fitted $\Delta I_{ds} - V_{gs}$ curves using the linear electrical and thermal circuit model. The solid line in Fig. 5-11 shows the result of the calculation, based on the parameters $\kappa = 3.7 \times 10^{-11}$ W/K, $T_s = T_b = 1.6$ K and $T_d = 2.1$ K at the first subband ($n = 1$). A fitting parameter ζ has been used to relate the gate voltage to the energy scale of the QPC: $\zeta = 85$ V/eV. The parameter ζ was chosen such that the peaks of ΔI_{ds} coincided with the predictions for the thermal

current from the model. The agreement between the experimental and calculated sults is excellent, which supports our proposed electric and thermal modeling.

5.4 QPC with drain/source coupled antenna

In the following radiation experiments we used the QPC as a nonlinear device. The results of such measurements using a QPC have recently been published by Arnone *et al.* [74]. Our analysis is analogous to their approach and we have therefore adopted the same notation. In contrast to their work, we have proceeded further in the analysis and used the value of the fitting parameter β to find numerical estimates for the absorbed radiation power.

In the experiment, the QPC was biased such that conduction takes place through only the first subband. The dc radiation-induced current ΔI_{ds}, caused by the ac voltage generated by the radiation field, was then measured. The bow-tie antenna in this device was coupled to the drain/source contacts and the axis was oriented parallel to the direction of electron transport through the constriction. The device was submerged in liquid helium during the measurement [49]. The radiation was guided into the cryostat using a 0.5 inch diameter circular lightpipe and was incident on the device from the substrate side. The 285 GHz coherent radiation was generated by a frequency trippler connected to the output of a Gunn oscillator [52]. The cryostat contained a superconducting magnet coil which we used to generated the perpendicular magnetic field of 0.9 T. The magnetic field reduces the probability of backscattering while an electron propagates from one side of the QPC constriction to the other. As seen from the magnetic field measurements in chapter 4, such a weak magnetic field does not affect the energy level structure of the QPC appreciably.

5.4.1 Rectification

In the presence of an oscillatory voltage across a nonlinear device, such as the QPC, the dc drain/source current I_{ds} through the device changes. We now derive an expression for ΔI_{ds} in terms of the device's conductance G_{ds} and the absorbed power P^{abs}. In section 5.4.2 we present the measured response of a QPC in the presence of a radiation field.

For an antenna oriented along the direction of electron transport, we can write the difference in the electro-chemical potential of the drain and the source contacts as

$$V_{ds}(t) = V_0 + V_1 \cos \omega t, \tag{5.5}$$

where V_0 is the dc drain/source bias voltage, V_1 is the amplitude of the ac voltage generated between the antenna terminals, and ω is the angular frequency of the radiation field. For a small amplitude ac voltage V_1 the nonlinear $I_{ds} - V_{ds}$ of a device can be expanded in a Taylor series in the vicinity of the bias point V_0

$$I_{ds}(V_{ds}(t)) = I_{ds}(V_0) + \frac{dI_{ds}(V_0)}{dV_{ds}} V_1 \cos \omega t + \frac{1}{2} \frac{d^2 I_{ds}(V_0)}{dV_{ds}^2} V_1^2 \cos^2 \omega t. \tag{5.6}$$

Each of the derivatives are evaluated at V_0. When measuring the dc response of the device, only the terms in Eq. 5.6 which does not oscillate make a contribution to the dc drain/source current. After evaluating the time-average of $I_{ds}(t)$ in Eq. 5.6 and after subtraction of $I_{ds}(V_0)$ we find the dc radiation-induced current

$$\Delta I_{ds} = \frac{1}{4} \frac{d^2 I_{ds}}{dV_{ds}^2} V_1^2. \tag{5.7}$$

The magnitude is proportional to the curvature of the $I_{ds} - V_{ds}$ characteristics and the square of the ac voltage V_1. In the measurements we biased the QPC so that

conduction through the first subband is partially activated. The resistance of the QPC was $G_{ds}^{-1} \approx 50$ kΩ. The characteristic impedance of the bow-tie antenna is $R_a \approx 70\ \Omega$ which is much smaller than the device resistance. The absorbed power $P^{\rm abs}$ in the QPC can therefore be approximately written as

$$P^{\rm abs} \approx \tfrac{1}{2} G_{ds} V_1^2. \tag{5.8}$$

By writing the conductance of the device as $G_{ds} = dI_{ds}/dV_{ds}$ and combining Eq. 5.8 and Eq. 5.7 we find from the definition of the current responsivity R_I

$$R_I \equiv \Delta I_{ds}/P^{\rm abs} = \frac{1}{2}\frac{d^2 I_{ds}/dV_{ds}^2}{dI_{ds}/dV_{ds}}. \tag{5.9}$$

Eq. 5.9 is valid when the nonlinearity in $I_{ds} - V_{ds}$ of the device is small on the voltage scale of $\hbar\omega/e$.

5.4.2 Measurement

An SEM micrograph of the device structure we used in the experiment is shown in Fig. 4-13. The pair of gates A/B3 was used to deplete the electron gas and define the constriction, and the remaining gates were connected to the source which defined the ground potential. Figure 5-12 shows a measurement of the conductance G_{ds} as a function of the drain/source bias voltage V_{ds}. Such nonlinear experiments have been performed by Kouwenhoven *et al.* [3] to find the energy spacing between the first and the second subband when the QPC was biased at the center of the first conductance plateau. The inset shows the $I_{ds} - V_{gs}$ characteristics; the bias point corresponding to $V_{gs} = -1.195$ V is indicated by the arrow. The nominal conductance corresponding to the gate voltage we used is $G_{ds} \approx e^2/2h$ which is one quarter of the quantized conductance step height.

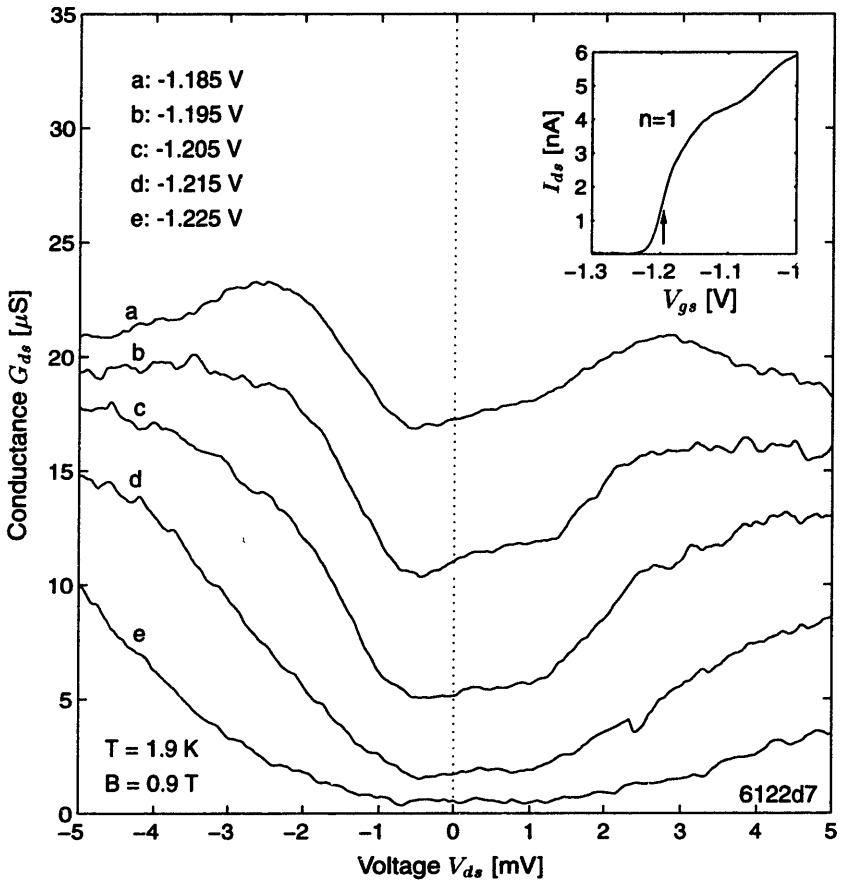

Figure 5-12: Drain/source conductance G_{ds} of QPC 6122d7-A/B3 plotted as a function of the drain/source bias voltage V_{ds}. The curves a through e correspond to the following gate voltages: -1.185 V, -1.195 V, -1.205 V, -1.215 V and -1.225 V, respectively. These gate voltages bias the QPC at the conduction threshold of the first quantized conductance step. The inset shows the $I_{ds} - V_{gs}$ characteristics of the QPC. The arrow indicates bias condition b. The measurements were performed at a temperature of 1.9 K in a perpendicularly oriented magnetic field of 0.9 T.

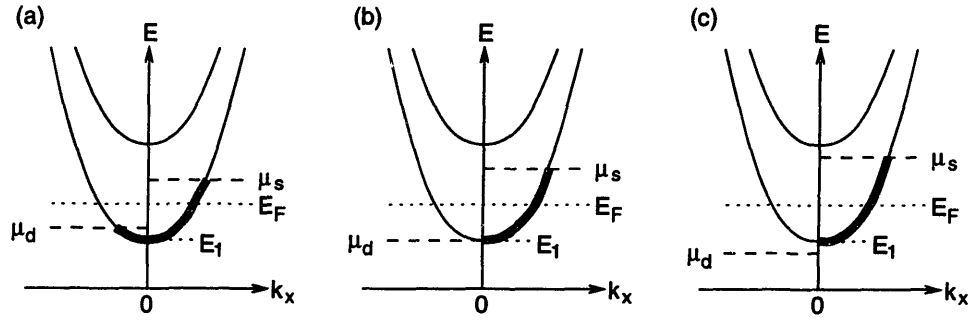

Figure 5-13: Subband occupation at QPC constriction where the conductance is determined. (a) Fermi energy E_F is placed such that conduction through first subband is activated; (b) electro-chemical potential of drain reservoir, μ_d, coincides with threshold energy of first subband, E_1, and the QPC conductance G_{ds} reaches a local maximum; (c) the electrochemical potential μ_d falls below E_1 and G_{ds} starts decreasing.

The behavior of the conductance for the QPC can be understood from the schematic illustration in Fig. 5-13. The relative position of the electro-chemical potentials μ_d and μ_s in the drain and the source reservoirs, respectively, are shown for an increasing value of the applied drain/source voltage; $eV_{ds} = \mu_s - \mu_d$. The Fermi energy E_F is positioned above the threshold energy E_1 for subband $n = 1$. This corresponds to case (a) in Fig. 5-12 when the gate voltage is $V_{gs} = -1.185$ V. In Fig. 5-13(a) the conductance remains approximately constant as V_{ds} increases from zero to about ± 1 mV. The conductance then steadily increases until μ_d approaches E_1 (shown in (b)). Because of the finite longitudinal curvature ω_x of the QPC potential the transmission probability through the constriction in the vicinity of E_1 gradually decreases from unity to zero. This results in the steady increase of the conductance for $|V_{ds}| = 1$ mV to 2.5 mV. The conductance reaches a peak at $|V_{ds}| \approx 2.5$ mV which indicates that the transmission probability for electrons with energy lower than μ_d from the drain to the source is vanishingly small. In (c) the conductance has decreased, because an increase in V_{ds} only results in an increase of μ_s by $V_{ds}/2$.

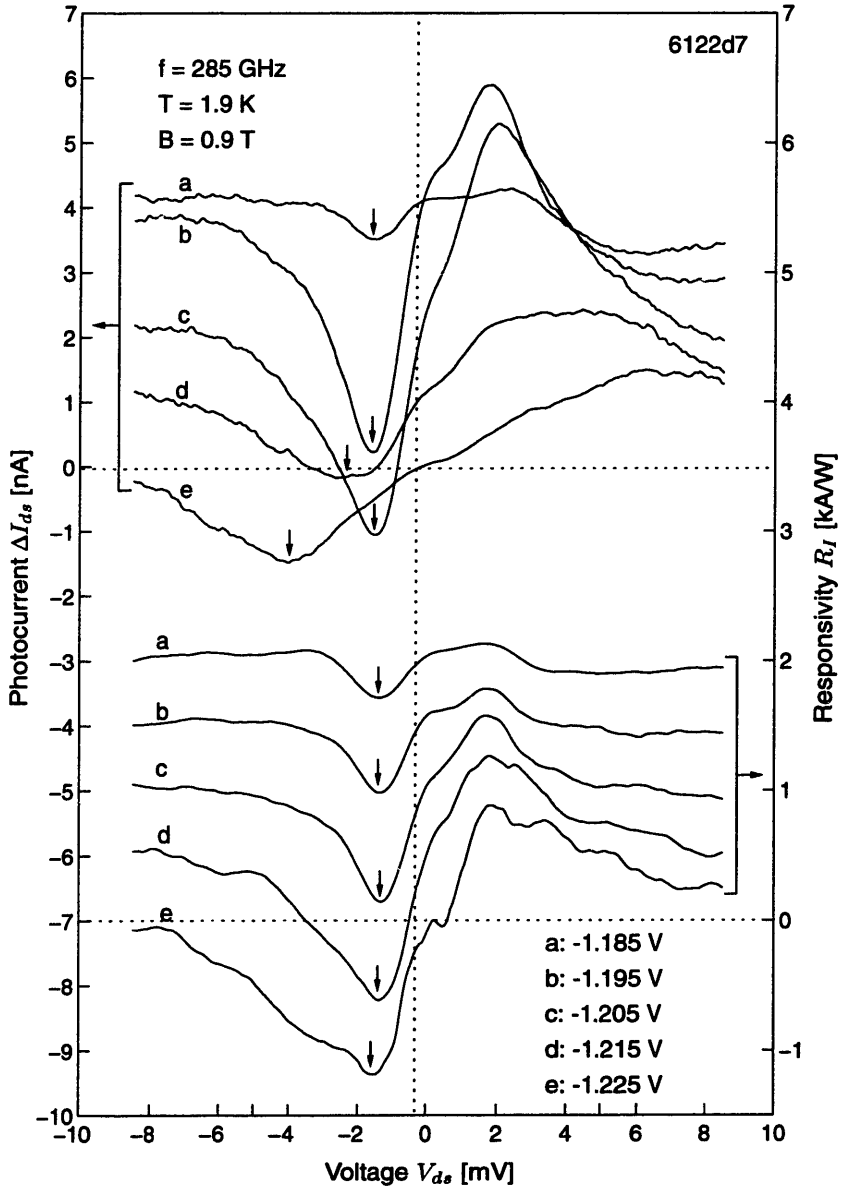

Figure 5-14: Top five curves show the radiation-induced drain/source current ΔI_{ds} as a function of V_{ds}. The radiation frequency was 285 GHz. The lower five curves show the calculated current responsivity R_I as a function of V_{ds}. R_I was calculated using the conductance data shown in Fig. 5-12. The arrows indicate the position of the minima in the valley. A shift is observed in the position minima in the ΔI_{ds} measurement but not in the calculated value for R_I. The measurements were performed at a temperature of 1.9 K in a perpendicularly oriented magnetic field of 0.9 T. ΔI_{ds} curves have been offset by 1 nA and R_I curves by 500 A/W for clarity.

Figure 5-14 shows the radiation-induced ΔI_{ds} plotted as a function of V_{ds} (top five curves). In our discussion we will concentrate on the minima in ΔI_{ds} indicated by the arrow. The position of the minima shifts towards more negative V_{ds} as V_{gs} decreases. For comparison we have calculated R_I from G_{ds} shown in Fig. 5-12 using Eq. 5.9 (lower five curve in Fig. 5-14). We find a minimum in R_I as observed in ΔI_{ds}, but the position of the minima does not shift towards more negative values of V_{ds} as V_{gs} decreases. It follows from Eq. 5.9 that the calculated values for R_I are proportional to ΔI_{ds} only if the absorbed power P^{abs} remains constant as V_{ds} varies, which is not the case in our experiment.

We identified in Eq. 5.8 that P^{abs} is approximately proportional to G_{ds}. This would mean that the value of V_1 is constant, independent of V_{ds}. As Arnone *et al.* [74] suggested, we define the parameter β as

$$\Delta I_{ds} = \beta \frac{d^2 I_{ds}}{dV_{ds}^2} = \beta \frac{dG_{ds}}{dV_{ds}}. \tag{5.10}$$

This parameter is related to V_1 and P^{abs} as follows

$$\beta = \tfrac{1}{4} V_1^2 = \tfrac{1}{2} G_{ds}^{-1} P^{\text{abs}}, \tag{5.11}$$

where G_{ds} is the QPC's small-signal conductance. In Fig. 5-15 we have plotted ΔI_{ds} and $\beta dG_{ds}/dV_{ds}$ as a function of V_{ds}. The derivative of the conductance was numerically calculated from the data shown in Fig. 5-12. The value of β was determined by equating the value of the minima in ΔI_{ds} with $\beta dG_{ds}/dV_{ds}$ at the same value of V_{ds}. We chose the voltage V_{ds} to correspond to the bias condition of the valley. This choice was arbitrary, we might as well have chosen the peak ΔI_{ds} at positive values of V_{ds}. For our choice, deviations are seen in the prediction of the amplitude of ΔI_{ds} at positve V_{ds}. The shape of the ΔI_{ds} curves, however, agrees well with dG_{ds}/dV_{ds}. We

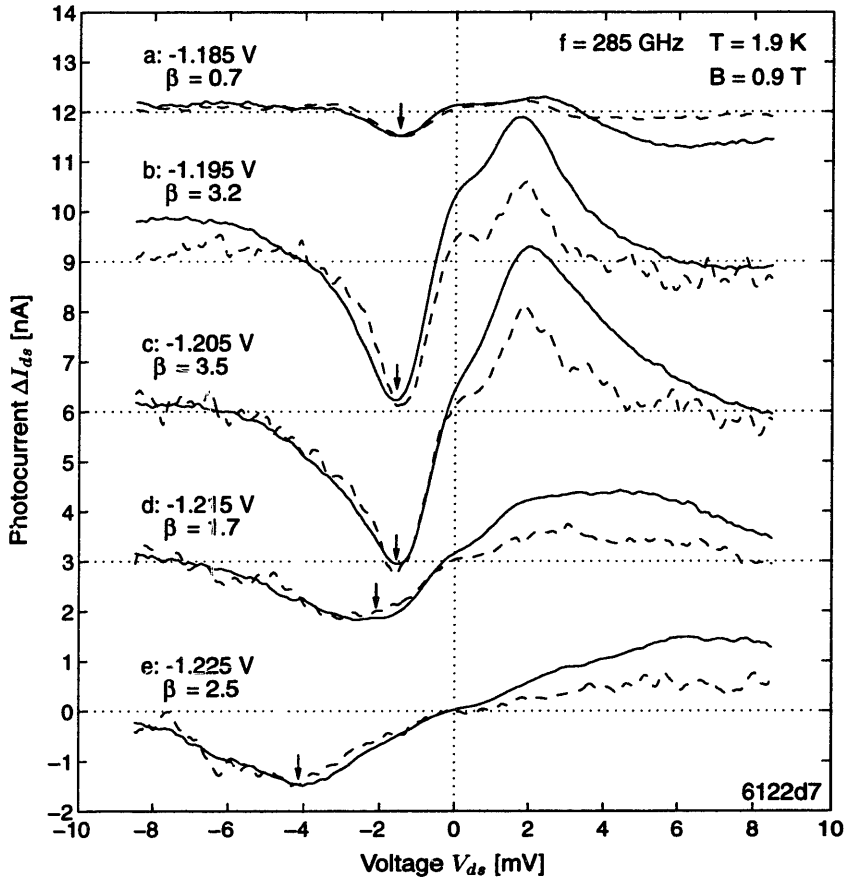

Figure 5-15: Comparison of the radiation-induced drain/source current ΔI_{ds} (solid curve) generated with 285 GHz radiation and the derivative of the dc conductance dG_{ds}/dV_{ds} times β (dashed curve) for a QPC. The arrow indicates the position of the valley minima. Values of β are determined by equating ΔI_{ds} with $\beta dG_{ds}/dV_{ds}$ at this valley minima. The values of β are in units of $\times 10^{-6}$ V^2. The measurements were performed at a temperature of 1.9 K in a perpendicularly oriented magnetic field of 0.9 T. ΔI_{ds} and $\beta dG_{ds}/dV_{ds}$ curves have been offset by 3 nA for clarity.

Table 5.1: Summary of analysis for QPC with drain/source coupled antenna. The values for G_{ds} are taken from Fig. 5-12. The minima for ΔI_{ds} corresponding to the drain/source bias V_{ds} are taken from Fig. 5-15. The parameters β, V_1, P^{abs} and η are derived quantities.

V_{gs} [V]	G_{ds} [μS]	V_{ds} [mV]	ΔI_{ds} [nA]	β [$\times 10^{-6}$ V^2]	V_1 [mV]	P^{abs} [pW]	η [%]
-1.185	20.9	-1.60	-0.49	0.7	1.7	30	1.9
-1.195	15.7	-1.60	-2.77	3.2	3.6	100	3.3
-1.205	12.0	-1.99	-3.06	3.5	3.7	89	4.1
-1.215	6.5	-2.31	-1.17	1.7	2.6	22	6.3
-1.225	6.5	-4.04	-1.46	2.5	3.2	33	5.2

are currently not certain about the origin of these deviations. The value we obtained for the parameter β and consequently for V_1 and P^{abs} using Eq. 5.11 are listed in Table 5.1. We find that the value of $V_1 \approx 3$ mV, which means $\alpha = eV_1/\hbar\omega \approx 2.5$. The efficiency, η, of the QPC response is found by comparing the ratio $\Delta I_{ds}/P^{\text{abs}}$ to the quantum efficiency $e/\hbar\omega$. For the bias point c we have $\Delta I_{ds} = -3.06$ nA and $P^{\text{abs}} = 89$ pW and the efficiency is

$$\eta = \frac{|\Delta I_{ds}|/P^{\text{abs}}}{e/\hbar\omega} \approx 4\%. \tag{5.12}$$

In the last experiment we investigated the response of a QPC to a linearly polarized radiation field; the plane of polarization was oriented either along or transverse to the antenna axis. In this measurement we used the He3 cryostat [77]. This cryostat used the improved quasi-optical system described in section 3.6.2. An SEM micrograph of the device is shown in Fig. 4-6.

The response of the QPC for the polarization plane of the radiation field oriented parallel, at 45 degrees, and orthogonal to the antenna axis is shown in Fig. 5-16. The response was seen to depend on the orientation of the polarization plane. This

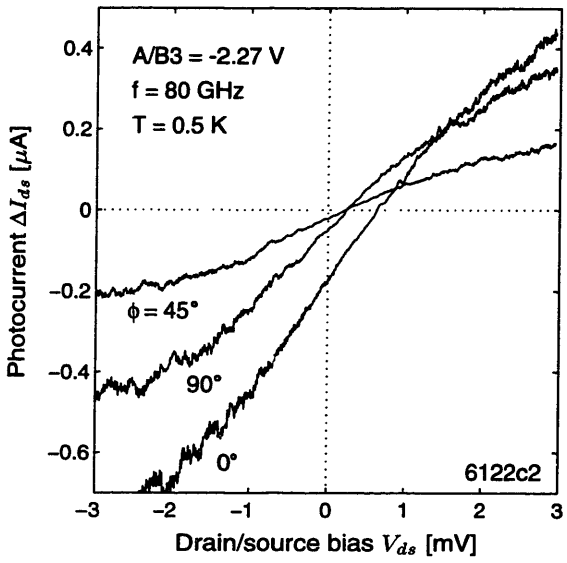

Figure 5-16: Photocurrent ΔI_{ds} of QPC 6122c2-A/B3 using 80 GHz radiation. Polarization plane of incident radiation is oriented either parallel ($\phi = 0°$), at 45 degrees ($\phi = 45°$) or orthogonal ($\phi = 90°$) to the bow-tie axis. Gate voltage was A/B3=-2.27 V (bias point corresponds to the threshold voltage for subband $n = 2$. Measurement was done at 0.5 K.

was encouraging because it means that the antenna was focussing the radiation. The largest signal was observed when the plane of polarization was aligned with the axis of the antenna. The signal observed for the orthogonal polarization was non-zero and could be caused by the gate leads acting as a dipole antenna which would couple radiation into the QPC in a direction orthogonal to the transport. The small signal at 45 degrees was probably caused by a combination of the two mechanism above. At $V_{ds} = 3$ mV the zero-bias corrected radiation-induced current was 0.62 μA for the parallel and 0.40 μA for the orthogonal polarization plane. At 45 degrees ΔI_{ds} was reduced to 0.38 μA. The radiation-induced current for the orthogonal polarization was therefore reduced by 1.6 times compared to the orthogonal polarization. Arnone *et al.* [74] measured an average decrease of 1.8 times for the transverse polarized radiation field. The agreement between our results is good considering the two QPCs used different radiation coupling geometry. We used a drain/source coupled antenna while they uses a gate coupled antenna.

5.5 Summary

Coupling radiation into a quantum effect device will always lead to some degree of free carrier heating of the two-dimensional electron gas. This heating is simple ohmic heating of the electrons confined to the heterointerface between the GaAs and the AlGaAs. We found that the radiation-induced current for a QPC with a gate coupled antenna was predominantly caused by heating of the electron gas in the drain and the source reservoir. Since the two electron reservoirs are weakly coupled via the quantum point contact, the heat exchange between the reservoirs and the 2DEG is limited. If the two electron reservoirs are heated in an imbalanced fashion, this limited heat exchange results in unequal electron temperatures in the two reservoirs. This steady-state thermal gradient across the quantum point contact was studied. Careful modeling of both the electrical characteristics and the thermal circuit resulted in a model which closely described the data measured at low radiation power levels. A model for the thermoelectric effect in the presence of high power levels did not work very well. For very strong heating, current contributions from adjacent conduction channels are not negligible, and the simple linear thermal model breaks down.

The signal observed for the QPC with a drain/source coupled antenna was in part caused by rectification of the ac current induced by the radiation. This conclusion was based on the similar behavior of the radiation-induced current and dG_{ds}/dV_{ds}. In addition, we observed that alignment of the polarization plane of the radiation with the antenna axis resulted in a signal 1.6 times larger than for the orthogonal orientation. This dependence on the orientation of the polarization plane of the incident radiation is believed to be caused by non-thermal processes.

No evidence of sidebands originating from absorption of modulation quanta by ballistic electrons was observed in the device characteristic. We attribute this failure to both insufficient confinement of the ac electric field and operation of the QPC when

subbands are partially activated. When transport through a subband is activated, the wavefunctions do no longer evanescently decay at the constriction and based on the simulation results, the probability of modulation quanta absorption becomes vanishingly small.

The experimental results on the QPC bolometric response and quantum oscillation of thermopower was published in Appl. Phys. Lett. **63**, 1522 (1993); and in Appl. Phys. Lett. **66**, 1144 (1995).

Chapter 6

Lateral dual gate device

6.1 Introduction

This chapter presents the dc transport characteristics of a lateral dual gate device. The work in the present and the next chapter was a collaboration with Dr. Thomas Schäpers and Dr. Simon Verghese in our research group. In section 6.2 an approximate method is presented which can be used to calculate the drain/source current for these devices. Section 6.3 shows the two device geometries we explored. Section 6.4 compares the single gate behavior to predictions of transmission over an inverted parabolic potential. Measurements of the dc transport characteristics of dual gate devices are discussed in section 6.5 and 6.6. Section 6.7 summarizes the experimental findings.

6.2 Two-dimensional transport

Ballistic electron transport between the drain and the source in a dual gate device is two-dimensional; the motion of the electron is constrained only in a direction normal to the 2DEG. The energy dispersion for the electrons in the 2DEG ($x - y$ plane) is

parabolic and can be written as

$$E = E_x + E_y = \frac{\hbar^2}{2m^*}(k_x^2 + k_y^2), \tag{6.1}$$

where m^* is the electron effective mass, and k_x and k_y are the wavevectors along the x and y direction, respectively. The net current I_{ds} flowing from drain to source (x-direction) is found by summing over all activated transverse (y-direction) conduction channels. The potential barriers due to depletion of the 2DEG by the gate structure in an ideal device are only a function of the position along the x-direction. Thus, the transmission coefficient connecting two states at the same energy on opposite sides of the barriers can be written as $T(E_x)$; a function of only the longitudinal energy E_x. The transmission coefficient is taken to be independent of the applied bias voltage V_{ds}, but depends implicitly on the gate voltage through the barrier height. In section 6.6, limitations to this approximation are encountered when applying a large V_{ds}, which causes a significant distortion of the potential profile. The net current is found by evaluating the integral [78]

$$I_{ds} = \frac{2ew}{h^2}\sqrt{2m^*k_BT}\int_0^\infty F_{-1/2}(\eta)\,[T(E_x + eV_{ds}) - T(E_x)]\,dE_x, \tag{6.2}$$

where w is the width of the conduction channel, k_B is the Boltzmann constant, T is the device temperature, $F_{-1/2}(\eta)$ is the Fermi-Dirac integral of order $-\frac{1}{2}$ [79], and $\eta \equiv (E_F - E_x)/k_BT$. No analytic expression can be found for the Fermi-Dirac integral except at zero temperature, where it simplifies to $F_{-1/2}(\eta) = 2\sqrt{\eta}$.

For a small bias voltage V_{ds} at zero temperature, we can further simplify Eq. 6.2. The difference between two transmission coefficients evaluted at energies separated by eV_{ds} can be viewed as a differential operation. Hence, the current I_{ds} can be written in terms of the partial derivative of the transmission coefficient with respect to the

longitudinal energy:

$$I_{ds} = \frac{4e^2 V_{ds} w}{h^2} \sqrt{2m^*} \int_0^{E_F} \sqrt{E_F - E_x} \left(\frac{\partial T}{\partial E_x} \right) dE_x. \tag{6.3}$$

Using Eq. 6.3, the drain/source current can be evaluated in a straightforward fashion if the transmission coefficient is known as a function of the longitudinal energy. In section 6.4 we will consider a model describing the potential profile with a single gate as an inverted parabola. Since an analytical expression can be obtained for the transmission coefficient, the conductance of a single gate device can be found as a function of the gate voltage.

6.3 Device structures

There are several dc biasing methods which can be used to reveal resonant transport of ballistic electrons through a dual gate device. Early studies of the characteristics of these devices have been performed by Ismail *et al.* [11] and Chou *et al.* [10]. In one method, a small voltage V_{ds} is applied between the drain and the source ohmic contacts, and the drain/source current I_{ds} is monitored as a function of the voltages applied to the gates V_{g1} and V_{g2}. When utilizing this method, it is advantageous to use identical gates and to apply the same voltage to both gates. Because of symmetry, the peak transmission for all resonance levels is equal to unity. Unfortunately, the threshold voltages of a pair of nominally identically designed gates are seldom equal when fabricated. A better technique, therefore, is to fix the voltage of one gate near the threshold, and sweep the voltage applied to the second gate. This assures that for at least one gate bias condition, the two potential barriers attain equal height, and sharp resonances should be obtained. With both of these techniques, the transmission coefficient through a double barrier structure is measured at the Fermi energy as a

function of the gate voltages.

The design of such a symmetric device is shown in Fig. 6-1 (left-most pair of gates). The gate lengths are 50 nm, the smallest dimension we achieved using a single pass exposure with an electron-beam system (JEOL 5DII), and they are separated by 130 nm. The antenna terminals, with a gap of 8 μm, are not visible on the micrograph because only the center area, measuring 7.2×13.2 μm, is shown.

In the second method, the $I_{ds} - V_{ds}$ characteristics of the device are measured while the two gate voltages are fixed. Since the two potential barriers represent high resistance domains, we expect the voltage V_{ds} to drop predominantely across the two potential barriers. Using this method, significant distortions of the potential barriers are expected when compared to the small bias condition. In fact, a V_{ds} of only a few mV's, which would already be on the order of the Fermi energy, would suffice to significantly perturb the top of the barriers. The important resonant levels near the top of the barrier which we intend to utilize would then be destroyed. This problem is expected to most severely affect transport in a device with equal length gates, since V_{ds} would drop symmetrically across each barrier. This non-ideality is avoided by using a design with gates of different lengths. For such an asymmetric design, the largest fraction of V_{ds} should appear across the longest gate. We expect that at least for one polarity of V_{ds}, the resonant levels will not be destroyed for a useful range of V_{ds}.

The first asymmetric gate design is shown in Fig. 6-1 (right-most pair of gates). The gate length are 50 nm and 130 nm, separated by 250 nm. The second design of an asymmetric dual gate structure is shown in Fig. 6-2. The photograph shows the center area measuring 2.9×4.9 μm. The gate dimensions are identical, but the antenna terminal gap has been reduced to 1.5 μm. Four gates have been added to define the 3 μm wide channel. During operation, a large negative voltage (-2 V) is applied to

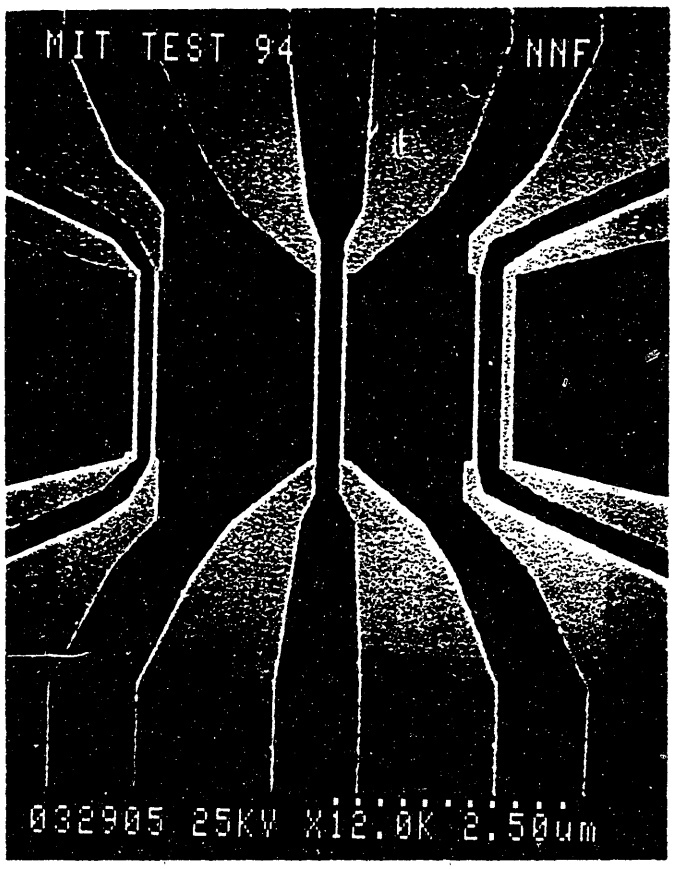

Figure 6-1: Scanning electron micrograph of tripple dual gate structure. Measurement results using the symmetric structure on the left and the asymmetric structure on the right are shown in this chapter. For the symmetric structure, the gate lengths are 50 nm, spaced apart by 130 nm. For the asymmetric structure, the gate lengths are 50 nm and 130 nm, spaced apart by 250 nm. The channel width is 3 μm and the antenna terminal gap is 8 μm. The vertical dimensions appear shorter because the substrate was mounted at a 45 degree inclination while photographed.

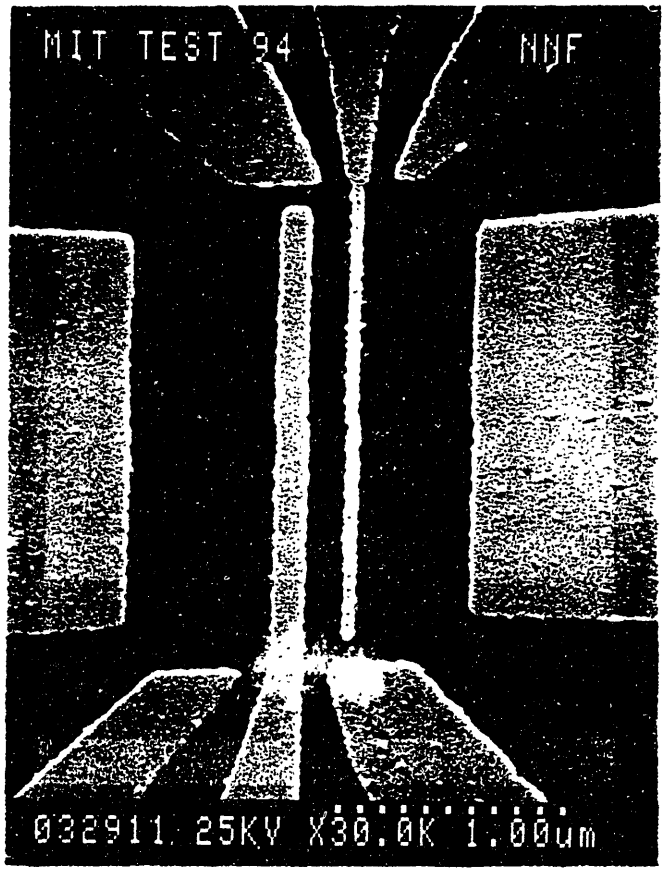

Figure 6-2: Scanning electron micrograph of an asymmetric dual gate structure. The gate lengths are 50 nm and 130 nm, the gate separation is 250 nm, the channel width is 3 μm and the antenna terminal gap is 1.5 μm. The vertical dimensions appear shorter because the substrate was mounted at a 45 degree inclination while photographed.

these channel defining gates. This voltage is sufficiently large to fully deplete the two-dimensional electron gas directly under and close to the channel-defining gates.

6.4 Single gate device behavior

We will first analyze the behavior of a lateral dual gate device when only one gate is used. From simulations performed in chapter 2, we found that V_0 varies approximately linearly with the gate voltage V_{gs}. Similar to the saddle-point potential approximation for the QPC the electrostatic potential created by a single gate can be approximated by an inverted parabolic profile

$$V(x) = V_0 - \tfrac{1}{2}m^*\omega_x^2 x^2 \tag{6.4}$$

by expanding the Gaussian potential profile presented in chapter 2 at $x = 0$. The value of the potential at the center of the gate is V_0, the electron effective mass is m^*, and the curvature along the transport direction is ω_x. If we denote the threshold voltage for conduction by V_t and the Fermi level by E_F, then

$$V_0 = E_F\left(\frac{V_{gs}}{V_t}\right). \tag{6.5}$$

Connor [80] found that the transmission coefficient through a potential profile given by Eq. 6.4 can be written in the form

$$T = \frac{1}{1+e^{-2\pi\varepsilon}}, \tag{6.6}$$

where the dimensionless parameter ε is defined as

$$\varepsilon = \frac{E_x - V_0}{\hbar\omega_x},$$

and E_x is the electron injection energy in the x-direction.

The two-dimensional conductance G of a single-gate device at zero temperature can be calculated using Eq. 6.3. Thermal broadening of the Fermi surface at finite temperatures can be taken into account by the convolution method [69]. The partial derivative of the transmission coefficient given in Eq. 6.6 is

$$\frac{\partial T}{\partial E_x} = \frac{\pi}{2\hbar\omega_x} \cosh^{-2}(\pi\varepsilon). \tag{6.7}$$

In the limit where the curvature ω_x approaches zero, the partial derivative of the transmission coefficient with respect to the energy reduces to the delta-function, $\delta(E_x - V_0)$. The conductance is obtained by evaluating the integral in Eq. 6.3

$$G = G_q \frac{2w}{\lambda_F} \left(1 - \frac{V_{gs}}{V_t}\right)^{1/2}, \tag{6.8}$$

where λ_F is the Fermi wavelength and $G_q \equiv 2e^2/h$ is the conductance of a one-dimensional channel. For a Fermi energy of 12.9 meV and a channel width of 3 μm, the ratio $2w/\lambda_F \approx 150$ signifies the maximum number of activated transverse channels. At zero gate voltage, the resistance is 90 Ω.

In chapter 2, the Gaussian potential profile predicts a curvature ω_x at the conduction threshold of 3 meV and 2.1 meV for gate lengths of 50 nm and 130 nm, respectively. When the curvatures are finite, Eq. 6.7 must be used. However, the effects of finite temperatures can be neglected below 1.6 K since $T \ll \hbar\omega_x/2\pi k_B$. The curvature of the potential barrier can thus be found by substitution of Eq. 6.7 into Eq. 6.3.

Figure 6-3 shows the drain/source current I_{ds} as a function of the voltage applied in turn to the 50 nm and 130 nm gates. The threshold voltage for the short gate is -217 mV and for the long gate is 4 mV. These threshold voltages are anomalously

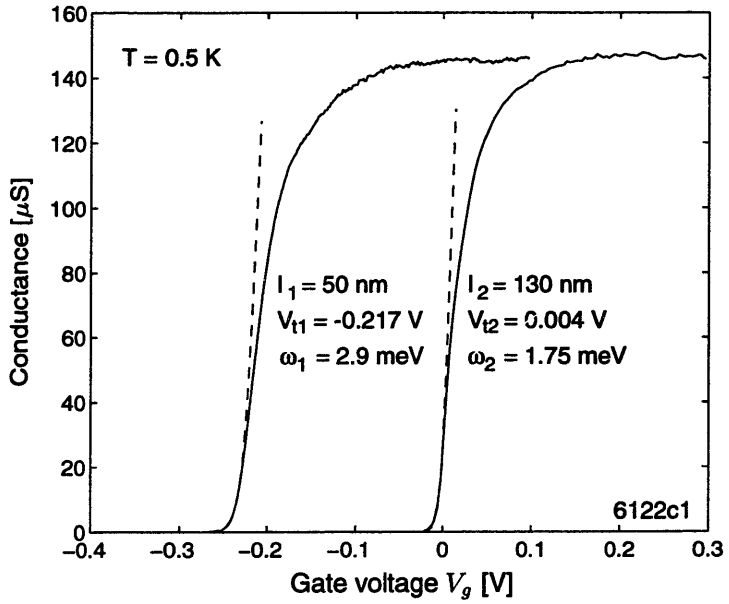

Figure 6-3: Conductance of individually biased gates with length 50 nm and 130 nm plotted as a function of the gate voltage (device structure in Fig. 6-2 was used). Dashed lines indicate the best visual fit of the data at the conduction threshold to Eq. 6.3. The zero gate voltage resistance is 6.9 kΩ.

high, probably because of charge trapping. Based on simulation we expected the threshold voltage to be -0.7 V for the short gate and -0.4 V for the long gate. The dashed lines indicate the best visual fit to the data at the conduction threshold. We found that the curvature at the conduction pinch-off is well-described by the inverted parabolic potential approximation to the Gassian potential model. The values for the curvature ω_x were 2.9 meV and 1.75 meV for gate lengths of 50 nm and 130 nm, respectively. Deviation from ideal behavior was observed when the conductance exceeded 40 μS. The observed saturation was caused by additional series resistance presented by the ohmic contacts, the two-dimensional electron gas and the measurement leads.

The values obtained for the curvatures when fitting the data correspond well with the values obtained by simulating the device structure using a two-dimensional Poisson solver. This agreement is fortunate, since we have to rely heavily on comparisons to simulation results when analyzing data from dual barrier experiments.

6.5 Device characteristics at the Fermi level

In this section we will analyze results of dual barrier measurements when using a small drain/source bias voltage. Two techniques are explored: (1) the voltages applied to the two gates are tuned to achieve comparable potential barriers; and (2) the voltage of one gate is fixed while the voltage of the other gate is varied continuously.

In Fig. 6-4 using the first technique the calculated transmission coefficient is shown as a function of electron injection energy and gate voltage. The same voltage is applied to both gates; $V_{g1} = V_{g2}$. The gate lengths are 50 nm and they are separated by 130 nm. The simulation uses the Gaussian potential profile description derived in chapter 2 which expresses the barrier height as a function of the gate voltage. The plot shows the evolution of the three resonant levels near the top of the barriers.

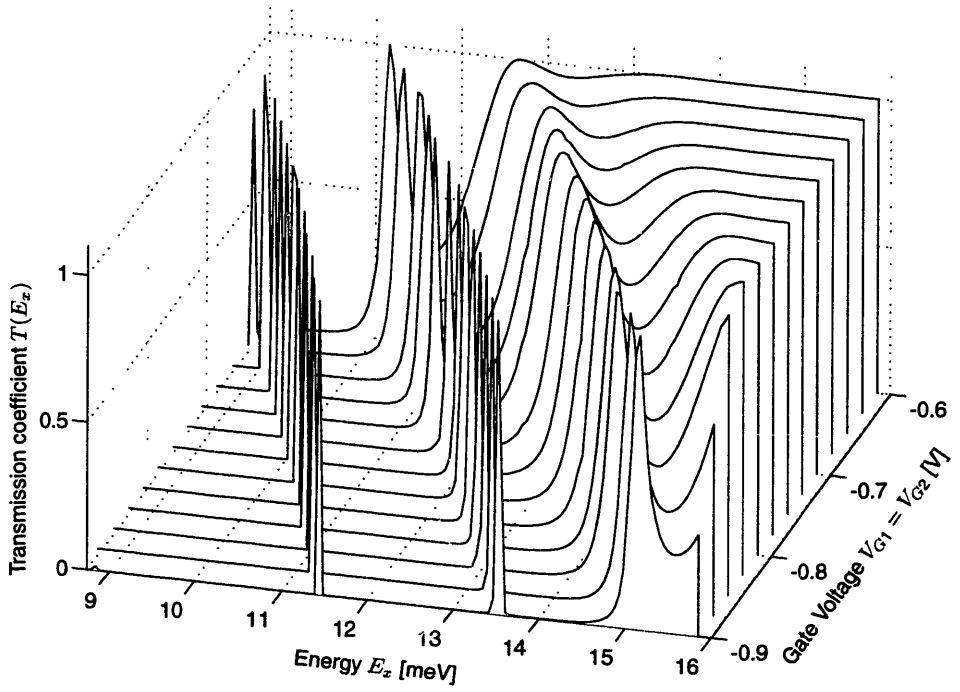

Figure 6-4: Theoretically calculated transmission coefficient through a dual gate structure as a function of electron injection energy and gate voltage. The length of the two gates is 50 nm and they are separated by 130 nm. In this simulation, the same voltage is applied to both gates.

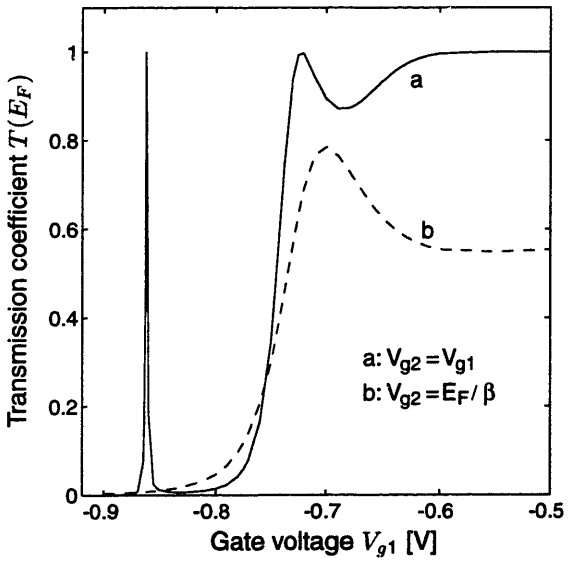

Figure 6-5: Transmission coefficient at the Fermi level as a function of the voltage on gate 1. For case a (solid line) the voltage on gate 2 is $V_{g2} = V_{g1}$. For case b (dashed line) the voltage on gate 2 is kept fixed at $V_{g2} = E_F/\beta$. This makes the top of barrier 2 coincide with E_F. The value of β depends on the barrier length and is equal to 17.1 meV/V for a 50 nm long gate. The Fermi energy is set to 12.86 meV. The length of both gates is 50 nm and they are separated by 130 nm.

As the confinement of the region between the gates is increased (larger negative gate voltages), the resonant levels are seen to move towards higher energy. This movement of the levels is partly caused by an increase of the barrier length and partly by an increase in the overlap between the barriers of the two gates. When the gate voltage reaches -0.9 V, an additional resonant level is added between the barriers. From the plot in Fig. 6-4 it is clear that the gate voltage is not linearly related to the electron longitudinal energy E_x near the top of the barrier. As an additional state is added between the barriers, the transmission coefficient changes dramatically. For the lower lying resonant levels however, a change in the gate voltage is equivalent to a proportional change in E_x.

The transmission coefficient at the Fermi energy, set to $E_F = 12.9$ meV in this example, is shown by curve (a) in Fig. 6-5. At a low gate voltage, $V_g > -0.5\ V$, the transmission coefficient is close to unity because the top of the barriers are far below the Fermi energy. As the gate voltage is decreased, the transmission coefficient dips to 0.88, but recovers to unity when $V_g = -0.725$ V. The transmission coefficient then rapidly decreases to zero. When the gate voltage reaches $V_g = -0.86$ V, the next lower resonant level coincides with the Fermi energy and a second peak occurs in the transmission coefficient of the Fermi level. This second peak, however, is very narrow, and will be significantly broadened even at temperatures as low as 0.5 K. Curve (b) in Fig. 6-5 shows the development of the transmission coefficient using the second technique. The voltage of one gate, V_{g1}, is varied, while the voltage on the other gate, V_{g2}, is kept fixed at a value where the top of the barrier coincides with the Fermi energy. If the voltage V_{g1} is zero, the transmission coefficient no longer reaches unity, but is $\frac{1}{2}$ due to the alignment of the second barrier with E_F. As V_{g1} decreases, a single peak develops when $V_{g1} = -0.7$ V. We note that the maxima of this peak is shifted by 25 mV in gate voltage when compared to the previous peak. Hence, this

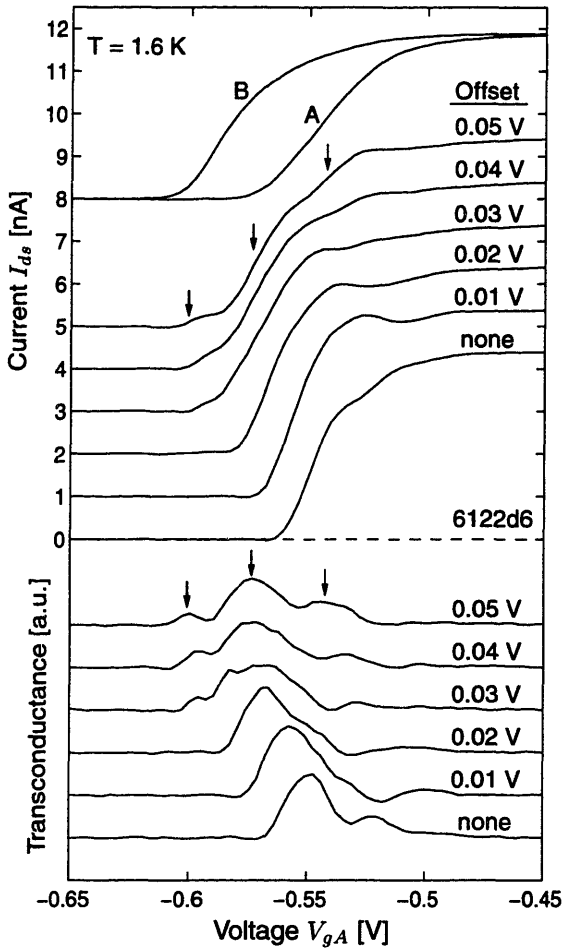

Figure 6-6: The top two curves show the drain/source current of individually biased 50 nm gates A and B as a function of applied voltage (left-most structure in Fig. 6-1). For the group of six curves below, the voltage on gate A equals the voltage on gate B plus the offset indicated. The offset is added to compensate for the difference in threshold voltage. Each trace has been spaced by 1 nA for visibility. The bottom group of six curves shows the transconductance for each offset voltage. The arrows mark three peaks in the transconductance. For $V_{gA} = V_{gB}+50$ mV, the spacing between peaks is approximately 28 mV. Measurement conditions were $V_b = 50$ μV, $R_l = 10$ kΩ and T = 1.6 K.

peak does not occur when the two barriers attain an equal height.

Figure 6-6 shows experimental results using the first biasing techniques. Curves A and B show the single gate characteristics using a bias voltage of 50 μV. The threshold voltage difference for these two 50 nm long gates is 35 mV which is small compared to the nominal threshold voltage of -590 mV. We then added an offset voltage to gate A to compensate for the small difference in the threshold. The offset voltage was incremented in steps of 10 mV from zero to 50 mV. Additional features, marked by the arrows, appeared as the barrier height difference was compensated. Since the left-most two peaks are present only when the barrier heights are carefully tuned, we believe these to be caused by resonance levels. Two such resonance peaks

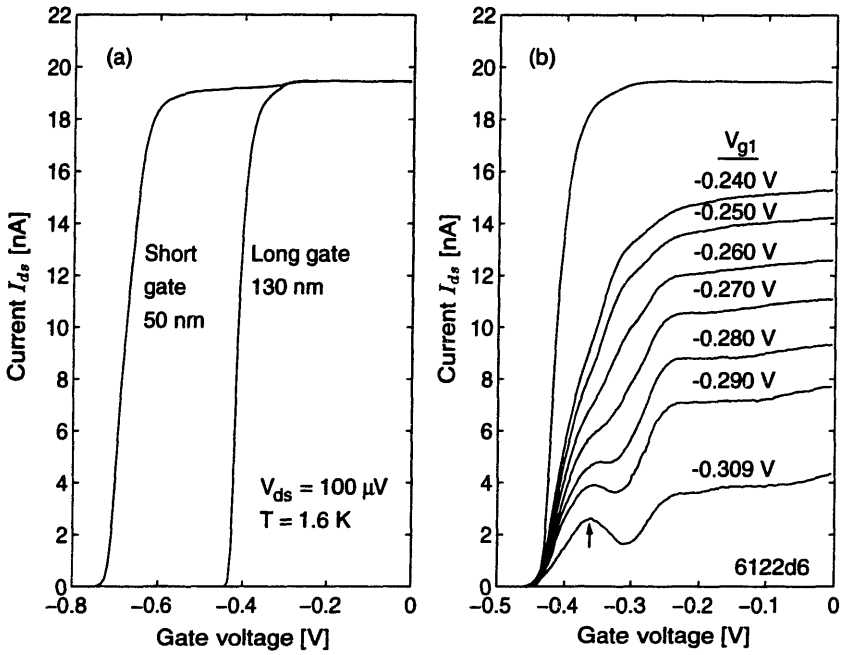

Figure 6-7: (a) Drain/source current as a function of gate voltage for individual biasing of 50 nm and 130 nm gates (right-most structure in Fig. 6-1). The threshold voltages compare well with theoretical predictions. (b) Drain/source current for a symmmetric gate pair (left-most structure in in Fig. 6-1) for various combinations of voltage V_{g1} and V_{g2} applied to the two gates. In the plot, V_{g1} is incremented in steps of 10 mV while V_{g2} is scanned. An arrow marks a peak which developed because of a resonant level. For reference, the single gate characteristics of gate 2 is shown by the top curve. The measurements were performed using a 100 μV drain/source bias at a temperature of 1.6 K.

are predicted by simulation as shown by curve (a) in Fig. 6-5. The right-most peak, causing even a negative differential transconductance when the offset voltage is 10 mV and 20 mV, is most likely not because of a resonant level. Such negative differential conductance has been predicted when in the presence of nonuniformities and disorder at the heterointerface [81]. The shoulder present in the trace of gate B could possibly originate from these non-idealities.

Figure 6-7(a) shows I_{ds} when 50 nm and 130 nm gates are inividually biased as a function of the voltage applied to the gate. The measurement of this device was

performed during the first thermal cycling [56]. The threshold voltages for both gates correspond well with the theoretically predicted values. The top-most curve in Fig. 6-7(b) is a repeat measurement of the same 50 nm gates after a refill of liquid helium was performed. During this refill the device temperature rose above 4.2 K for a short period of time. We noticed that the threshold voltage increased by 0.3 V. This positive shift was found to occur after the devices were kept at low temperatures for several days. We attributed this shift to a loss of carriers in the 2DEG. The remaining curves show experimental results when using two 50 nm gates while executing the second biasing techniques. In this dual gate experiment, the voltage applied to gate 1 was incremented from -0.24 V to -0.309 V in steps of 10 mV. The voltage applied to gate 2 was varied continuously. The arrow marks the single peak which developed for an appropriate choice of the voltage applied to gate 1. The development of a single peak is consistent with the prediction shown by curve (b) in Fig. 6-5.

The signature of resonant transport through a dual barrier structure has been observed. Experimental evidence for two different gate bias methods is consistent with theoretical predictions. In the first method, one relies on creating similar potential barriers by careful tuning of the gate voltages. When successful, two peaks in the transconductance because of resonant levels can be observed. In the second method, which is much easier to realize, only one peak can be obtained near the Fermi energy. One advantage of this technique, however, is that the peak is observable even when an asymmetric gate pair is used.

6.6 Device characteristics at finite bias

Up to this point, we have studied the transport characteristics of the dual gate device in the small drain/source bias regime. The barrier distortions due to V_{ds} were negligible and the transmission coefficent did not change compared to the zero bias

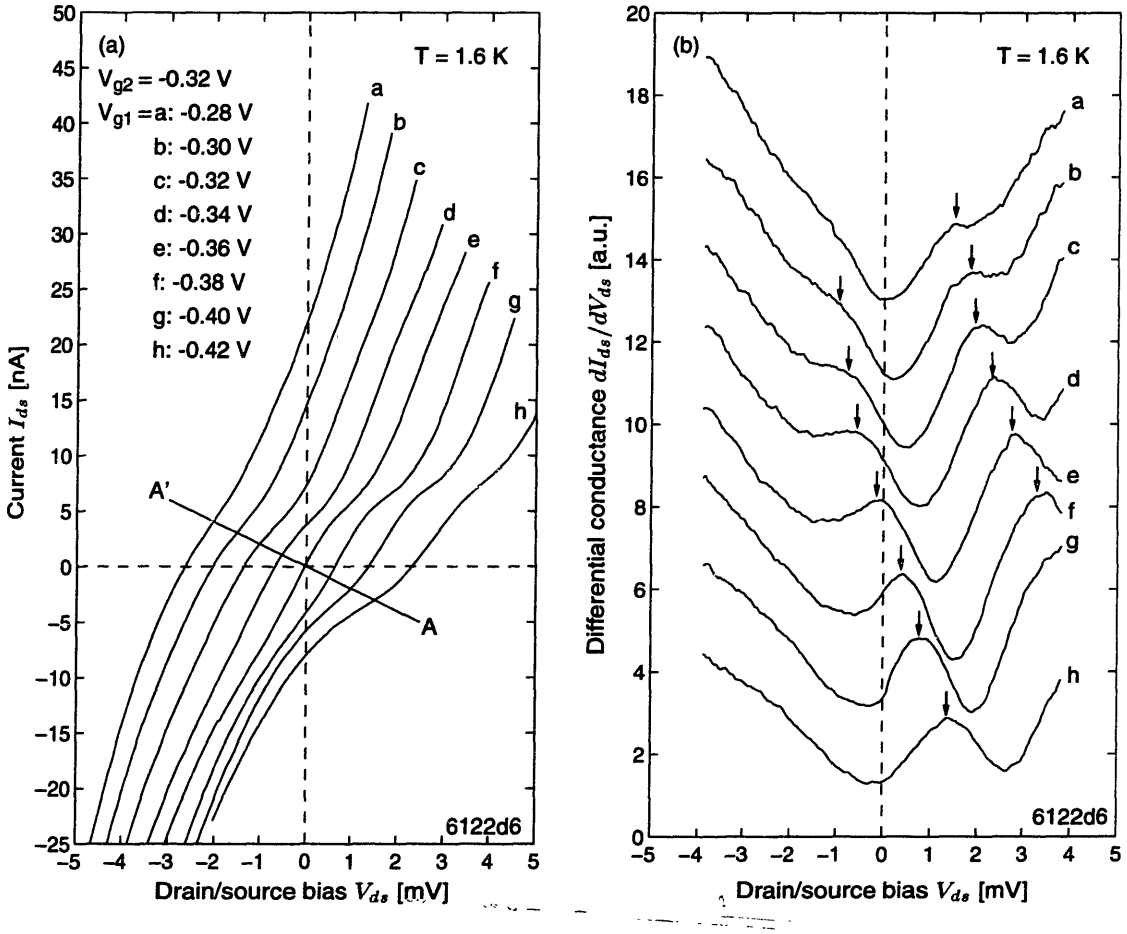

Figure 6-8: (a) Drain/source current as a function of drain/source voltage for left-most symmetric gate pair shown in Fig. 6-1. The voltage applied to gate 2, V_{g2}, is kept fixed at -0.32 V, while the voltage on gate 1, V_{g1}, is varied from -0.28 V to -0.42 V in increments of 0.02 V. The curves are shifted both horizontally and vertically for visibility; the line $A - A'$ crosses the zero bias position of each curve. (b) Differential conductance for the bias conditions shown in (a). The movement of two peaks, indicating the position of transmission resonance levels, are marked by arrows.

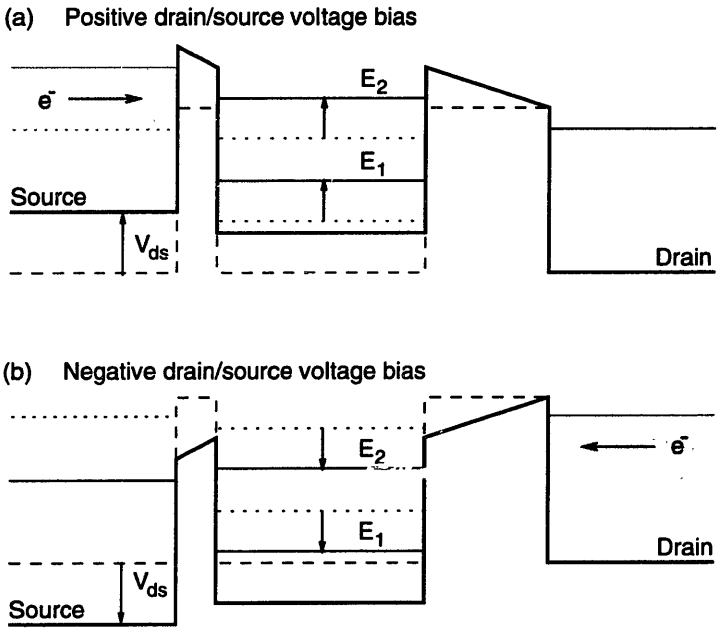

Figure 6-9: Schematic illustration of double barrier distortion caused by the drain/source voltage. The voltage drop is divided between the two barriers in proportion to the relative gate length.

case. However, when a large V_{ds} was applied across the device, the barrier distortion was no longer negligible. This section will explore the extent to which the zero bias transmission coefficient is applicable for large V_{ds}.

Figure 6-8 (a) shows the dc $I_{ds} - V_{ds}$ characteristics of a symmetric dual gate device. The gate lengths are 50 nm, separated by 130 nm. The voltage of gate 2 is fixed at -0.32 V while the voltage on gate 1 is varied from -0.28 V to -0.42 V in increments of 20 mV. A weak undulation is visible in each curve. A measurement of the derivative dI_{ds}/dV_{ds} clearly shows two peaks, see Fig. 6-8 (b). The data shows three key features: (1) each trace is asymmetric with respect to V_{ds}; (2) the distance in V_{ds} between the peaks is approximately constant; and (3) the location of the two peaks varies linearly with V_{g1}.

The potential profile of a symmetric dual gate device when applying a large V_{ds} is

schematically illustrated in Fig. 6-9. The difference in gate length, which is expected in a real device due to fabrication variability, has been exaggerated in the diagram. In (a) the source is biased negative with respect to the drain side, while (b) shows the opposite. In the illustration, we limited the voltage drop V_{ds} to the two barrier regions, divided in proportion to the barrier length. As shown, the well region is not distorted significantly in case (a), apart from the lifting of the bottom in the well. The resonant levels between the double barrier are hence lifted proportionately with the applied V_{ds}. The predominant current contribution is due to electrons in the energy interval marked by the grey regions. In case (a), the electrons can propagate through the top resonant level E_2. When the height of the shorter barrier is increased by applying a larger gate voltage, the resonant levels also shift to a higher energy due to the stronger confinement. This corresponds to the positive V_{ds} region for the curves in Fig. 6-8(b). In case (b) the resonant levels shift down in energy. Electrons in the marked energy interval cannot propagate through a resonant level, since they are inaccessible. Hence no evidence of resonant levels is observable in the I_{ds}. This corresponds to the negative V_{ds} region in Fig. 6-8. Based on this illustration, we have explained the asymmetry present in the $I_{ds} - V_{ds}$ characteristics on the basis that two nominally equal length gates produce a slightly different length potential profile.

Figure 6-10 replots the location of the two peaks in V_{ds} as a function of V_{g1}. The peaks are found to move linearly with the gate voltage at an approximate rate of 21 meV/V. This linear dependence of the resonance level positions as a function of the gate voltage was already illustrated in Fig. 6-4. The peak separation is about 2.9 meV and is constant for a range of gate voltages. The fixed peak separation is evidence for that the transmission coefficient is negligibly altered and only shifted proportionately to a change in V_{g1}. If we neglect the asymmetry present in the $I_{ds} - V_{ds}$ measurement and allocate the applied voltage symmetrically to the barriers,

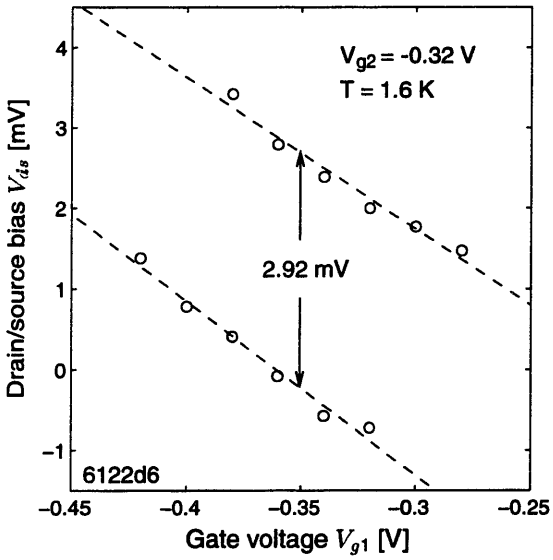

Figure 6-10: Resonant level position in terms of drain/source voltage as a function of voltage applied to gate 1. The voltage applied to gate 2 is fixed at -0.32 V. The data is obtained from Fig. 6-8(b).

the intersubband spacing between the two resonant levels is equal to half of the peak separation; $\Delta E = 2.9/2 = 1.45$ meV. This energy separation of the uppermost two resonant levels compares well with the calculated results of 1.51 meV based on this gate geometery.

6.7 Summary

In this chapter we explored the dc transport properties of a lateral dual gate device. We made theoretical predictions about the way in which the behavior of resonant levels between the two barriers manifests itself in the drain/source current. Measurements were performed both in the small and large drain/source bias regime. The experimental results were found to be consistent with theoretical predictions.

Chapter 7

Photo-response of lateral dual gate device

7.1 Introduction

The electron transport through dual gate devices is in many ways analogous to electron transport through a single vertical quantum well. Resonant tunneling in vertical quantum wells has been observed well into the THz-regime [82, 83]. The photoconductive gain of quantum-well structure was analyzed by Liu [84] and the frequency dependent response has been measured [85]. In this chapter we will present the results of measurements performed with symmetric and asymmetric dual gate devices and in particular investigate the frequency response of these devices.

Section 7.2 considers how the dc drain/source current I_{ds} is affected by the presence of radiation: the goal is to obtain a relationship between the absorbed radiation power and the change in the drain/source current ΔI_{ds}. When normalizing this expression by the total power absorbed, we find the current responsivity of the device, R_I, as a function of frequency. Since R_I can be expressed in terms of the device's

$I_{ds} - V_{ds}$ characteristics, predictions of ΔI_{ds} can be based on both microscopic theory, which does not take barrier distortions into account due to the finite bias voltage; and the dc $I_{ds} - V_{ds}$ response of the actual device, which does include the effects of barrier distortion. Experimental data of ΔI_{ds} are shown for two biasing methods, for $I_{ds} - V_{ds}$ in section 7.3 and for $I_{ds} - V_g$ in section 7.4. The observed ΔI_{ds} are then compared with predictions based on the two approaches mentioned above. A summary of the experimental findings is given in section 7.5.

7.2 Radiation response: Theory

The planar antenna which focusses the incident radiation produces an ac voltage across the device. As a result, the voltage difference between the drain and the source regions in the presence of radiation is equal to the sum of the dc drain/source bias V_0 and the ac voltage V_1. The total voltage drop can be written as

$$V_{ds}(t) = V_0 + V_1 \cos \omega t, \tag{7.1}$$

where ω is the angular frequency of the radiation field. In chapter 2 we found that in the presence of such an ac voltage, electrons tunneling through potential barriers can absorb and emit modulation quanta in multiples of the energy $\hbar\omega$. Such transitions are effectively taken into account by using the modified transmission coefficient T_ω when calculating the dc I_{ds}. Of course, T_ω only approximately describes the actual situation the electrons experience while traversing a double barrier potential. Large ac voltage swings distort the dc potential profile and reduce the sharpness of the resonant levels. The modulation also causes a reduction of the resonant level lifetime, since an electron in a quasi-bound level between the double barrier can absorb or emit modulation quanta which increases its probability of escape. Also, when a large V_0 is

applied across the device, on the order of E_F/e, the potential profile is significantly distorted. A finite V_0 changes the height of the two potential barriers, and hence, the transmission coefficient. In the derivation of the microscopic theory we neglect all these effects so that a straightforward method is obtained to compare theory and experiments. We need to keep in mind, however, that all three effects contribute to the destruction of the resonant levels.

From Eq. 2.19 the modified transmission coefficient T_ω for electrons with longitudinal energy $E_x + eV_0$ is given by

$$T_\omega(E_x + eV_{ds}(t)) = \sum_n J_n^2(\alpha) T(E_x + eV_0 + n\hbar\omega). \tag{7.2}$$

Here, $J_n^2(\alpha)$ is the square of the n-th order Bessel function, with argument $\alpha \equiv eV_1/\hbar\omega$. The argument α is the dimensionless parameter describing the strength of the ac voltage V_1 relative to the angular frequency ω of the radiation field. After substitution of the modified transmission coefficient into Eq. 6.2, which accounts for the effect of the radiation field, we find

$$\begin{aligned}
I_{ds}(V_{ds}(t)) &= \frac{2ew}{h^2}\sqrt{2m^* k_B T}\int_0^\infty F_{-1/2}(\eta) \\
&\quad \times \left[\sum_n J_n^2(\alpha) T(E_x + eV_0 + n\hbar\omega) - T(E_x)\right] dE_x \\
&= \frac{2ew}{h^2}\sqrt{2m^* k_B T}\int_0^\infty F_{-1/2}(\eta) \\
&\quad \times \left[\sum_n J_n^2(\alpha) T(E_x + eV_0 + n\hbar\omega) - \sum_n J_n^2(\alpha) T(E_x)\right] dE_x \\
&= \sum_n J_n^2(\alpha) \left\{\frac{2ew}{h^2}\sqrt{2m^* k_B T}\right. \\
&\quad \left. \times \int_0^\infty F_{-1/2}(\eta)\left[T(E_x + eV_0 + n\hbar\omega) - T(E_x)\right] dE_x\right\},
\end{aligned} \tag{7.3}$$

where the unitary property of the sum $\sum_n J_n^2(\alpha) = 1$ has been used to interchange

the summation with the integral operation. We recognize the term in parenthesis $\{\cdot\}$ as the drain/source current I_{ds} when using a bias voltage of $V_0 + n\hbar\omega$. The current I_{ds} in the presence of an ac voltage can therefore be written as

$$I_{ds}(V_{ds}(t)) = \sum_n J_n^2(\alpha) I_{ds}(V_0 + n\hbar\omega/e). \tag{7.4}$$

Eq. 7.4 gives a convenient recipe for calculating $I_{ds}(V_{ds}(t))$ in terms of the $I_{ds} - V_{ds}$ characteristics in the absence of radiation. We note that the formalism derived above is analogous to results obtained for superconductor-insulator-superconductor (SIS) tunnel junctions [32, 86]. Although Eq. 7.4 successfully describes photon-assisted transport in these tunnel junctions, several shortcomings are expected for the case of dual gate devices where the transmission coefficient depends on the values of V_0 and V_1.

For purposes of data analysis, it is sufficient to consider the device's response at low radiation power levels. In this limit ($\alpha \ll 1$) the square of the Bessel functions $J_n^2(\alpha)$ in Eq. 7.4 for $n = 0$ and ± 1 can be expandend in terms of α, $J_0^2(\alpha) \approx 1 - \alpha^2/2$ and $J_{\pm 1}^2(\alpha) \approx \alpha^2/4$. Higher order terms in sum can be neglected. The change in the current or the radiation-induced current, ΔI_{ds}, can therefore be written as a function of V_1 and ω

$$\begin{aligned} \Delta I_{ds} &= I_{ds}(V_{ds}(t)) - I_{ds}(V_0) \\ &\approx \tfrac{1}{2} V_1^2 \frac{e}{\hbar\omega} \left[\frac{I_{ds}(V_0 - \hbar\omega/e) - 2I_{ds}(V_0) + I_{ds}(V_0 + \hbar\omega/e)}{2\hbar\omega/e} \right]. \end{aligned} \tag{7.5}$$

The absorbed radiation power is related to the ac voltage by $P_\omega^{\text{abs}} = V_1^2/2R_\omega$. Here R_ω is the resistance of the device at bias point V_0 [86]. This resistance is evaluated

using a finite difference derivative of $I_{ds} - V_{ds}$, not the local derivative; hence

$$P_\omega^{\text{abs}} = \tfrac{1}{2} V_1^2 \left[\frac{I_{ds}(V_0 + \hbar\omega/e) - I_{ds}(V_0 - \hbar\omega/e)}{2\hbar\omega/e} \right]. \tag{7.6}$$

This absorbed power P_ω^{abs} must be distinguished from the incident power P_ω^{inc} of the radiation field. For a given P_ω^{inc}, the magnitude of P_ω^{abs} depends on the device impedance Z_q. A large mismatch between the antenna impedance of $R_a \approx 70\ \Omega$ and Z_q results in a large power reflection and only small a amount of power will be coupled into the device. We therefore expect the observed ΔI_{ds} in high resistance domains to be smaller than predicted compared w. $_{ds}$ generated in low resistance domains because of the relative reduction of P_ω^{abs}.

Finally, the current responsivity can be found by combining Eq. 7.5 and Eq. 7.6:

$$\begin{aligned} R_I &\equiv \Delta I_{ds}/P_\omega^{\text{abs}} \\ &= \frac{e}{\hbar\omega} \frac{I_{ds}(V_0 + \hbar\omega/e) - 2I_{ds}(V_0) + I_{ds}(V_0 - \hbar\omega/e)}{I_{ds}(V_0 + \hbar\omega/e) - I_{ds}(V_0 - \hbar\omega/e)}. \end{aligned} \tag{7.7}$$

Eq. 7.7 expresses R_I at radiation frequency ω in terms of the dc $I_{ds} - V_{ds}$ characteristics [86]. Comparison of the measured ΔI_{ds} can therefore be made not only with microscopic theory, but also when using the measured dc $I_{ds} - V_{ds}$ of the device. The second approach offers following advantages. The device's asymmetry is automatically incorporated into the predictions and the effects due to barrier distortion for large values of V_0 are taken into account. Although the asymmetry can be incorporated into the microscopic theory (as will be done in the next section), effects of the barrier distortion are difficult to account for. We therefore expect that predictions based on the measured dc $I_{ds} - V_{ds}$ more accurately reflect the device's photo-response compared with microscopic theory. We realize that the above statement is contradictory to the one presented in Verghese *et al.* [78]. We agree that electrons with

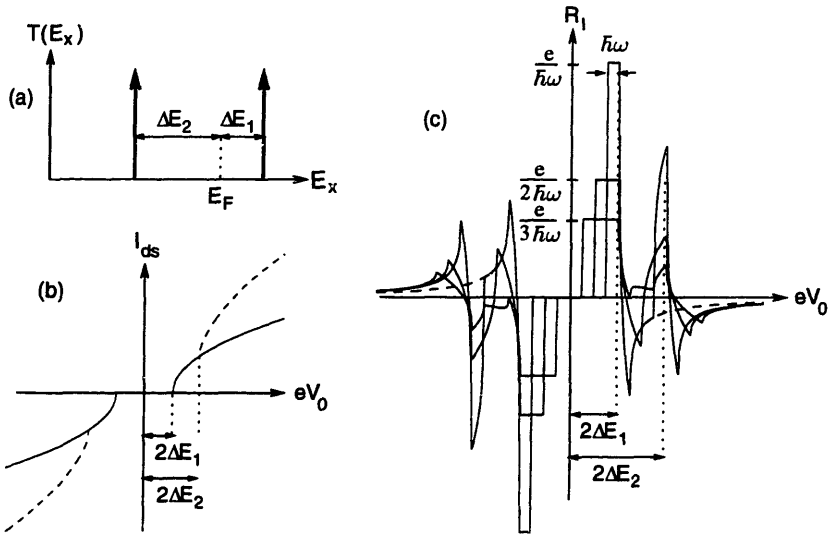

Figure 7-1: (a) Illustration of transmission coefficient through a model double barrier potential with two resonant levels. (b) Drain/source current I_{ds} as a function of eV_0 when (i) $a_1 = 1$ and $a_2 = 0$ (solid curve) and (ii) $a_1 = a_2 = 1$ (dashed curve). (c) Current responsivity R_I as a function of eV_0 for case (i) and (ii), displayed by the solid and the dashed curve, respectively. The frequency was set equal to $\omega = \Delta E_1/2\hbar$, $\Delta E_1/\hbar$, and $3\Delta E_1/2\hbar$.

energy E_x which absorbed a modulation quanta $\hbar\omega$ are subject to the transmission coefficient $T(E_x + \hbar\omega)$. Hence, at zero bias we would expect that microscopic theory predicts ΔI_{ds} accurately. Based on simulation results, however, we found that for a finite V_{ds} the transmission coefficient is significantly distorted even for a small V_{ds} (the bias voltage was dropped linearly along the double barrier potential). Using the transmission coefficient at zero V_{ds} to calculate ΔI_{ds} at finite V_{ds} does not accurately describe the situation. The arguments above are based on an understanding of the dc transport characteristic of the dual gate device. A comparison between R_I calculated from the two approaches will be compared to experimental results in section 6.6.

At this point it seems appropriate to illustrate the behavior of Eq. 7.7 for a simple model system. This will provide helpful insights when analyzing the non-trivial behavior of a device. We will simply take the transmission through a resonant

level of a double barrier potential as a δ-function. If the separation between the i-th resonant level location and the Fermi energy E_F is denoted by ΔE_i, we can write,

$$T(E_x) = \sum_i a_i \delta(E_x - E_F - \Delta E_i), \tag{7.8}$$

where E_x is the electron longitudinal energy and a_i is the transmission probability through the i-th level. When substituting Eq. 7.8 into Eq. 6.2, we find an expression for the dc $I_{ds} - V_0$. At zero temperature, assuming a symmetric voltage drop across the barrier, we find

$$\begin{aligned} I_{ds}(V_0) &= \frac{2ew}{h^2}\sqrt{2m^*}\sum_i a_i \left[\sqrt{eV_0 - 2\Delta E_i}\,\theta(eV_0 - 2\Delta E_i)\right. \\ &- \left.\sqrt{2\Delta E_i - eV_0}\,\theta(2\Delta E_i - eV_0)\right]. \end{aligned} \tag{7.9}$$

In Fig. 7-1(a) and (b) we schematically illustrate $T(E_x)$ and I_{ds} for two resonant levels taking $\Delta E_2 = -2\Delta E_1$. The current responsivity R_I, calculated using Eq. 7.7, is plotted in Fig. 7-1(c) for $\hbar\omega = \Delta E_1/2$, ΔE_1, and $3\Delta E_1/2$. We find that a photo-induced current will be generated even before the onset of conduction in the dc $I_{ds} - V_0$ characteristics. For example for $\hbar\omega = \Delta E_1$ the width of this region is $\hbar\omega$. The current responsivity in this voltage interval

$$0 < |eV_0| - 2\Delta E_1 < \hbar\omega,$$

is seen to remain constant, provided that $\hbar\omega < 2\Delta E_1$. The constant value, equal to $e/\hbar\omega$, represents the peak value the responsivity can theoretically obtain. This peak responsivity can be interpreted as transmission of a single electron through the resonant level after the electron absorbed a single modulation quanta $\hbar\omega$ [86]. Quantum limited detection is therefore achieved in this voltage interval. With this

example in hand, we are now ready to analyze the photo-induced current for a dual gate device.

7.3 $I_{ds} - V_{ds}$ photo-response

This section discusses the measured photo-response of an asymmetric dual gate device [78]. Figure 7-2 shows the $I_{ds} - V_g$ characteristics of the device. In this measurement we fixed the voltage of the long gate $V_{g,l}$ while the voltage of the short gate $V_{g,s}$ was varied. The behavior of the device is similar to the one described in section 7.4. The large shifts in the threshold voltage, on the order of 0.4 V when compared to values obtained from simulations, are probably due to trapped charge.

The $I_{ds} - V_{ds}$ characteristics of the device were measured setting $V_{g,l} = 6$ mV and varying $V_{g,s}$ from -0.24 V to -0.21 V in steps of 5 mV. For these gate voltage values, the zero V_{ds} operating point is to the left of the peak marked by the arrow in Fig. 7-2. Figure 7-3 shows the measured radiation-induced current ΔI_{ds} at 90 GHz and 270 GHz. Each curve corresponds to a different value of $V_{g,s}$. When comparing the left and the right data set, we notice that the amplitudes of the undulations are markedly different. At 90 GHz, the difference in ΔI_{ds} between peak 1' and valley 2 is 7.5 nA while at 270 GHz it has reduced to 2.5 nA. For both data sets we also notice a shift of the valleys 1 and 2 towards more negative V_{ds} as $V_{g,s}$ increases (marked by the arrow labeled 1 and 2 in Fig. 7-3). The direction of this shift can be explained as follows. A more positive $V_{g,s}$ lowers the height of the short barrier and will reduce the confinement of the resonant levels between the barriers. This reduction of the confinement will shift the resonant levels down in energy. If the Fermi energy is larger than the energy at which the resonant level of interest is located, the bias voltage must be increased to activate current transport through the level. Such a shift was already observed for the symmetric device measured in chapter 6. With a gate voltage of

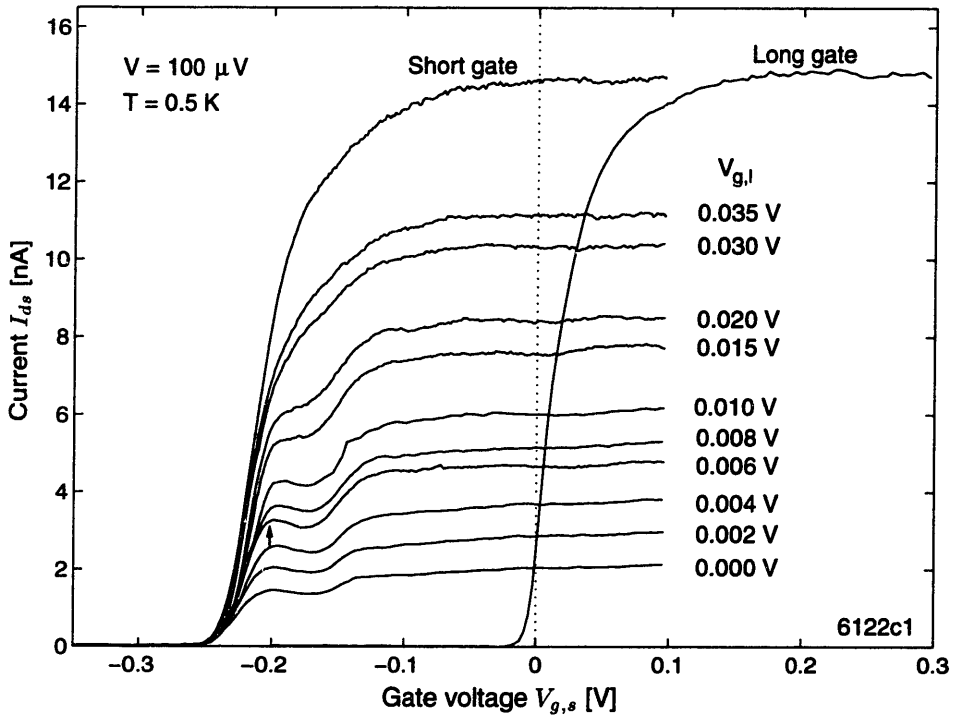

Figure 7-2: The top two curves show I_{ds} as a function of $V_{g,s}$ and $V_{g,l}$. The remaining curves show I_{ds} as a function of $V_{g,s}$ for $V_{g,l}$ fixed at values ranging from 0 to 35 mV. The peak observed at $V_{g,s} \approx -0.2$ V, marked by the arrow, is caused by a resonant level. The device was biased in the vicinity of the arrow during the radiation measurements. Measurement was performed using a bias voltage of $V_b = 100$ μV with a load resistor of $R_l = 10$ kΩ at a temperature of $T = 0.5$ K.

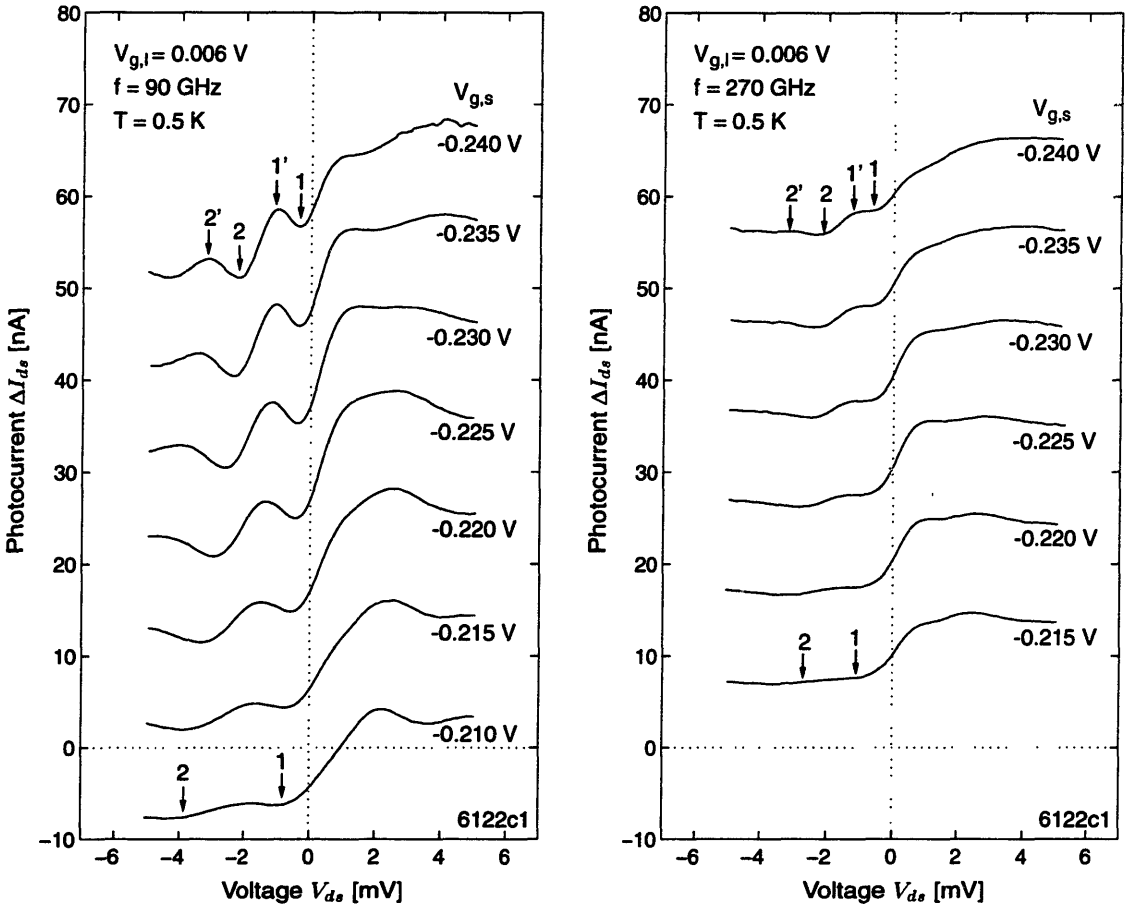

Figure 7-3: Photo-induced current ΔI_{ds} at 90 GHz (left) and 270 GHz (right) as a function of V_{ds}. The valley and peak due to two resonant levels have been marked by (1,1') and (2,2'), respectively. The voltage on the long gate, $V_{g,l}$, is kept fixed at 6 mV. The voltage on the short gate, $V_{g,s}$, is varied from -0.24 V to -0.21 V in steps of 5 mV. The positions of the valley/peak structure shifts to lower values of V_{ds} as $V_{g,s}$ increases. The curves have been offset by 10 nA for clarity.

$V_{g,s} = -0.23$ V, the separation between the two valleys 1 and 2 is 2.2 mV. Therefore, the intersubband spacing for this device is approximately $\Delta E_{12} = 2.2/2 = 1.1$ meV.

In contrast to radiation measurements with a quantum point contact discussed in chapter 5, no reversal of the polarity of ΔI_{ds} could be achieved for the dual gate device when the input direction of the radiation was varied. Only the magnitude of ΔI_{ds} was affected. In fact, this dependence was used to optimize the radiation coupling to the device. We already measured the dependence of ΔI_{ds} for a drain/source coupled QPC as the polarization plane of the incident radiation was oriented parallel or perpendicular to the axis of the planar antenna (see Fig. 5-16). Figure 7-4(a) and (b) shows ΔI_{ds} for the asymmetric dual gate device. This measurement was performed several days after the measurements shown in Fig. 7-3, during which the device remained at 4.2 K. Although the device characteristic appears to have changed significantly, this change does not influence the conclusion based on this measurement. The signal was significantly reduced for the perpendicularly polarized electric field, while a maximum signal was observed for the parallel polarized electric field. This would be expected if ΔI_{ds} were predominantly because of interaction of the barrier traversing electrons with the oscillating potential.

Next, we checked to see if the amplitude decrease of the undulations at higher radiation frequency was consistent with theory by using Eq. 7.7. Figure 7-5 shows the transmission coefficient as a function of the electron longitudinal energy E_x. In the simulation, the top of the potential barrier of the long gate coincided with the Fermi energy E_F. The height of the potential barrier of the short gate is varied in increments of 5%, relative to the height coincident with the Fermi energy (see inset in Fig. 7-5). We found a linear shift of the resonant levels as the height of the short barrier was varied. The direction of the shift was consistent with the observed shift in the data if we identify the sharp level below E_F (varies from 12 meV to 12.5 meV)

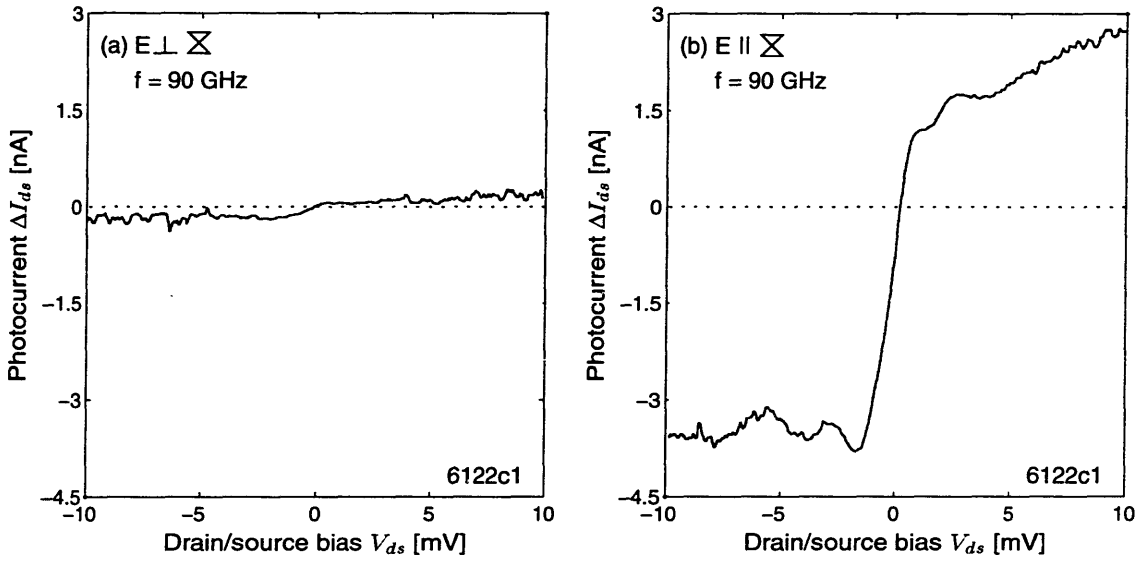

Figure 7-4: (a) Photocurrent of asymmetric double barrier device at 90 GHz radiation with polarization orthogonal to the bowtie antenna. (b) Polarization plane parallel to the antenna. Measurement temperature was 0.5 K.

as resonant level 1. A more positive value of $V_{g,s}$ shifts the peak downward in energy and a larger value of V_{ds} is required to activate conduction through this level. This shift was already discussed extensively in Fig. 6-10. Before using these transmission coefficients to calculate the current, we wanted to incorporate the asymmetry in the device's $I_{ds} - V_{ds}$ into our model. The value of the asymmetry indicates how large a fraction of V_{ds} is dropped on the drain side compared to the source side of the dual barrier device. We determined the asymmetry of the device by measuring the magnitude of $I_{ds}(V_0)$ at $V_0 = \pm 5$ mV. If we denote the current at these two bias points by $I_\pm$ the asymmetry factor ρ can be expressed by the ratio

$$\rho \equiv \frac{|I_-|}{|I_-| + |I_+|}.$$

For the asymmetric dual gate device we found $\rho = 0.565$. This asymmetry is in-

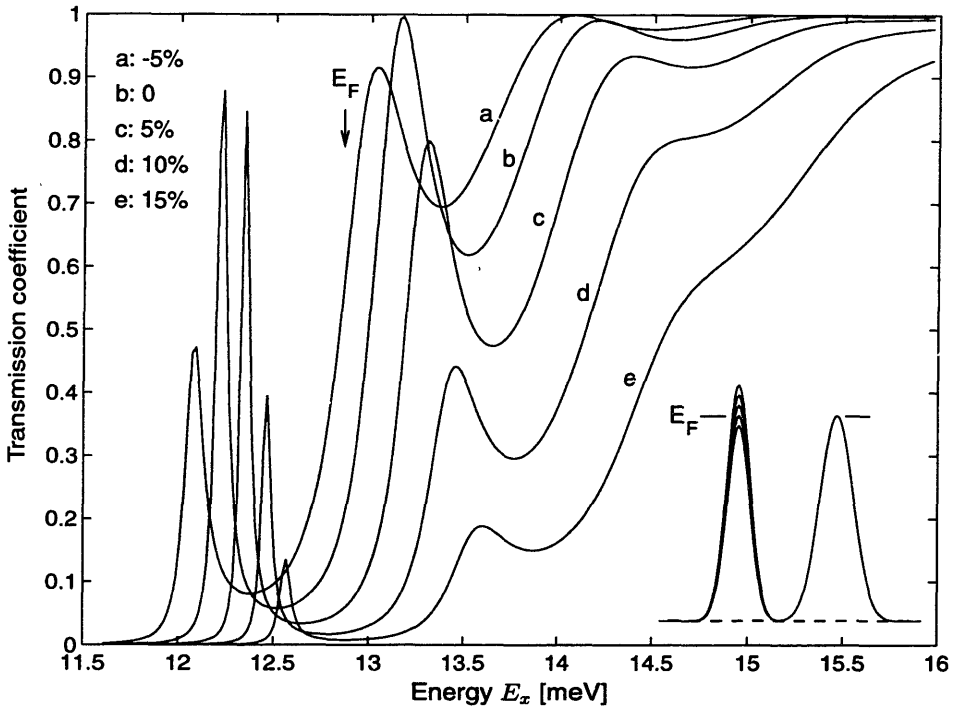

Figure 7-5: Calculated transmission coefficient as a function of energy. The top of the barrier produced by the long gate is kept fixed at the Fermi energy. The barrier of the short gate is varied from 5% below to 15% above the Fermi energy. The insert shows the potential profile for the two barriers. Simulation parameters used are 50 nm and 130 nm gate length with a 250 nm separation, a channel width of 3 μm, and a Fermi energy of 12.86 meV. The physical dimensions correspond to the layout of the asymmetric device 6122c1.

corporated into Eq. 6.2 by using the transmission coefficients $T(E_x + [1-\rho]eV_{ds})$ and $T(E_x - \rho eV_{ds})$ instead of $T(E_x + eV_{ds})$ and $T(E_x)$, respectively. The calculated $I_{ds} - V_{ds}$ is then substituted into Eq. 7.7 to find the theoretically predicted responsivity R_I. Figure 7-6(a) shows a plot of the calculated currents for the five gate voltage values a through e. From curve e we find the predicted I_{ds} to be 150 nA when the bias voltage is $V_{ds} = 2$ mV. For the device, when $V_{g,s} = 235$ mV and $V_{g,l} = 6$ mV, we measured a current of 20 nA using the same bias voltage of 2 mV. The cause of this large discrepancy between the observed and calculated currents is not clearly understood, but could be explained in part by the large resistance of the ohmics [78]. A weak non-linearity because of activation of resonant levels immediately above and below the Fermi level is apparent in the calculated curves. In Fig. 7-6(b) we show the predicted responsivity for gate bias condition c (5%) calculated for the three frequencies 90 GHz, 180 GHz and 270 GHz. As we illustrated with the simple model system in Fig. 7-1(c), the two valleys (marked 1 and 2), are because of two resonant levels. In that example, we found the peak responsivity was proportional to $1/\omega$ and the width of the first dip was proportional to ω. This dependence on frequency is also seen when R_I is calculated based on a more complicated model for the dual barrier device using a realistic $T(E_x)$. The calculated R_I shows features similar to the measured ΔI_{ds}: two well-defined valleys for negative V_{ds}. Consistent with observations, the amplitude of the undulations decreased as the radiation frequency was increased. Incorporation of the asymmetry factor $\rho = 0.565$ did result in a marked difference in R_I positive V_{ds} compared to negative V_{ds}. The differences, however, are not as large as in the measured ΔI_{ds}. The actual asymmetry factor of the device might therefore be even greater than 0.565. The separation between the two valleys 1 and 2 (marked by the arrows) is 1.6 mV, which gives a resonant level spacing of approximately $\Delta E_{12} = 0.8$ meV. This separation is slightly smaller than an estimate

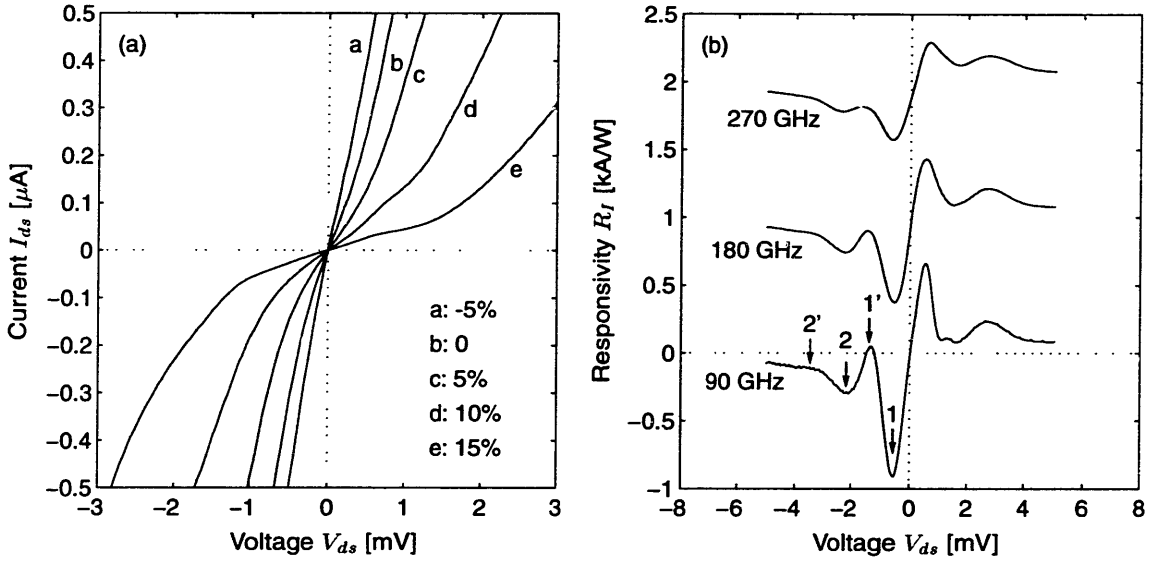

Figure 7-6: (a) Drain/source current I_{ds} as a function of drain/source voltage V_{ds}. The calculation was done using an electron reservoir temperature of 0.5 K and an asymmetry of 0.565. (b) Predicted current responsivity R_I as a function of drain/source voltage V_{ds} for bias condition c (5%).

based on the measurements.

One significant discrepancy that exists between the experimentally measured ΔI_{ds} and the theoretical prediction for R_I is the relative amplitude of the valleys 1 and 2, which are reversed. In part, as we are going to show below, the distortion of the potential barrier caused by the finite V_0 accounts for this. Such a distortion always results in a broadening of the resonant levels and a reduction of the peak transmission. This broadening will significantly reduce the amplitude of R_I at the first peak. Another reason for the reduced amplitude is perhaps because of the difference between P_ω^{abs} and P_ω^{inc}. For small values of V_{ds}, the resistance R_ω of the device is large and a relatively smaller amount of power is absorbed compared to when V_{ds} is large and R_ω has decreased. This smaller amount of absorbed power would further reduce the amplitude of ΔI_{ds} at valley 1 compared to valley 2. Estimates of R_ω

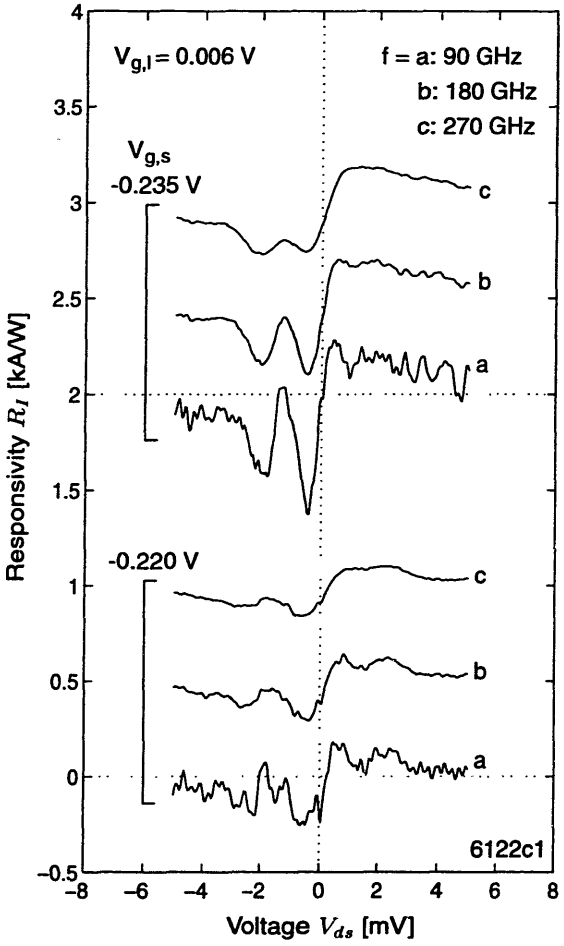

Figure 7-7: Calculated R_I at frequencies 90 GHz, 180 GHz and 270 GHz using a model based on the experimental $I_{ds} - V_{ds}$ curve.

corresponding to the valley minimum are given in Table 7.1: they are different by about a factor of two.

A second, independent prediction for R_I can be obtained by using the measured $I_{ds} - V_{ds}$ in Eq. 7.7. We have used the same data set as shown in Verghese *et al.* [78], but instead of smoothing the data which was done in that previous work, we used the raw data for our analysis. The result of the calculations for three different frequencies is shown in Fig. 7-7. The noise in the curves is because of evaluation of the finite difference ratio, which tends to amplify the high-frequency noise present in the raw data. Two gate voltage conditions have been selected: $V_{g,s} = -0.235$ V and -0.22 V while $V_{g,l} = 6$ mV. The calculation of R_I predicts again the general

Table 7.1: Comparison between predictions for P_ω^{abs} using the microscopic model with a theoretically derived $T(E_x)$ using an asymmetry factor of $\rho = 0.565$, and from calculation of R_I using the experimentally measured $I_{ds} - V_{ds}$. The detection efficiency η is found by dividing R_I by $e/\hbar\omega$. The photo-induced current ΔI_{ds} for the valleys 1 and 2 are used. The gate voltages applied to the device were $V_{g,s} = -0.235$ V and $V_{g,l} = 6$ mV.

				$T(E_x)$		$I_{ds} - V_{ds}$		
f [GHz]	Valley #	ΔI_{ds} [nA]	R_ω [kΩ]	R_I [A/W]	P_ω^{abs} [pW]	R_I [A/W]	P_ω^{abs} [pW]	η [%]
90	1	-4.1	98	-910	4.5	-630	6.5	23
90	2	-9.6	53	-300	32	-430	22	16
270	1	-1.9	88	-430	4.4	-260	7.3	29
270	2	-4.2	42	-220	19	-270	16	29

behavior of the measured ΔI_{ds}. Using the actual dc $I_{ds} - V_{ds}$ for the device, we find that the relative amplitude of the two valleys has changed; they are almost the same. We believe this reduction is because the measured dc $I_{ds} - V_{ds}$ properly accounts for the distortion of the transmission coefficient at finite V_{ds}. Such an improvement in the prediction of R_I compared to microscopic theory was expected, as we noted in our earlier discussion. In Table 7.1 we have summarized the results from calculation based on the microscopic model and using the measured dc $I_{ds} - V_{ds}$ for the valleys 1 and 2. The measured ΔI_{ds} corresponding to bias condition $V_{g,s} = -0.235$ V and $V_{g,l} = 6$ mV is shown. We find that the current responsivities from both methods result in comparable values for P_ω^{abs} on the order of tens of pW.

The success of the prediction for R_I based on microscopic theory and using experimentally measured $I_{ds} - V_{ds}$ was encouraging. The main features could be explained based on a straightforward theoretical model. The discrepancies between the microscopic theory and the measured ΔI_{ds} were partly explained by the distortion a finite V_0 causes since a calculation of R_I using the measured $I_{ds} - V_0$ reduced the discrepan-

cies. The difference in the estimated value of P_ω^{abs} at the minimum of the two valleys can partially be accounted for by the difference in R_ω.

7.4 $I_{ds} - V_g$ photo-response

In the second set of measurements, we explored the response of a symmetric dual gate device by measuring ΔI_{ds} as a function of gate voltage V_{g1} applied to one of the 50 nm gates. Both V_{ds} and the voltage applied to the second gate, V_{g2}, were kept fixed. The data is shown in Fig. 7-8 at three different frequencies. In each measurement, the power of the frequency source was adjusted to obtain approximately the same ΔI_{ds} at the peak. The general features of the curves are similar. All exhibit one isolated peak, one valley and a slow steady increase for gate voltages above -0.4 V. Closer inspection reveals an increase of the minima to the right of the peak for higher radiation frequencies. In addition, the height of the peak with respect to the magnitude of the photo-current ΔI_{ds} at $V_{g1} = -0.4$ V changes. At 39.2 GHz the ratio of the peak height to ΔI_{ds} at $V_{g,1} = -0.4$ V is 1.5, while at 255 GHz it is reduced to 0.75. The dashed line shows the $I_{ds} - V_g$ characteristics. This curve has been scaled to be visible on the scale of ΔI_{ds}. The current at the peak of the $I_{ds} - V_g$ curve was 2.7 nA, while the peak current for ΔI_{ds} at 39.2 GHz is only 50 pA. The amplitudes are different by a factor of 50.

Predicting ΔI_{ds} for this measurement is more involved than in the previous case. For each gate voltage value, the transmission coefficient is different. Hence, the current responsivity R_I must be recalculated with the appropriate transmission coefficient at each value for the gate voltage. Figure 7-9 shows R_I as a function of the radiation frequency for values of V_{g1}, varying from -0.65 V to -0.8 V in steps of 5 mV. Inspecting R_I for $V_{g1} = -0.8$ V, we notice a peak occuring in the responsivity at around 280 GHz. This corresponds to the energy difference between E_F and the res-

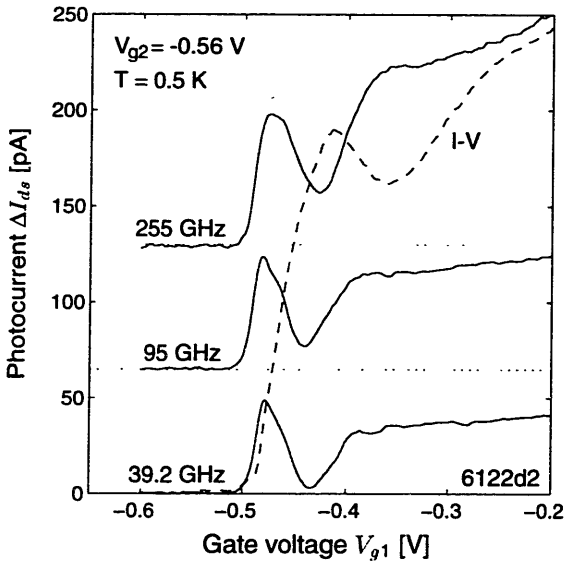

Figure 7-8: Photo-induced current as a function of bias voltage, applied to gate 1 using symmetric device. The voltage applied to the second gate is fixed at $V_{g2} = -0.56$ V. The curves have been offset by 65 pA for clarity. For comparison, we have plotted $I_{ds} - V_g$ for the same bias conditions, shown by the dashed line in arbitrary units. A bias voltage of $V_b = 75$ μV and a load resistor of $R_l = 10$ kΩ were used for this measurement.

onant level between the double barrier. This scenario corresponds to the simulation results obtained in chapter 2 for the dual gate device. As V_{g1} increases, this peak shifts towards lower frequencies. This downward shift was expected, because for a lower barrier height the resonant level position was reduced. At $V_{g1} = -0.725$ V, the current responsivity reaches a maximum at low frequencies. When V_{g1} is below -0.7 V the resonant level between the double barrier falls below E_F. A negative responsivity is found for this case.

Plotting these simulation results as functions of the gate voltage V_{g1}, we obtained the plot shown in Fig. 7-10. We have selected three frequencies corresponding to values used in the experiment. The responsivity is shown at an interval of V_{g1} where the transmission coefficient changes rapidly (the calculated $T(E_F)$ is shown by the dashed line). The simulation results suggest that the peak responsivity decreases as the radiation frequency increases. In addition, the peak position shifts toward lower gate voltages for increasing frequencies. The peak shifts about 40 mV as the frequency is increased from 43 GHz to 254 GHz. A negative responsivity is observed when $T(E_F)$ reaches a maximum. Similarly, this minima shifts by a small amount,

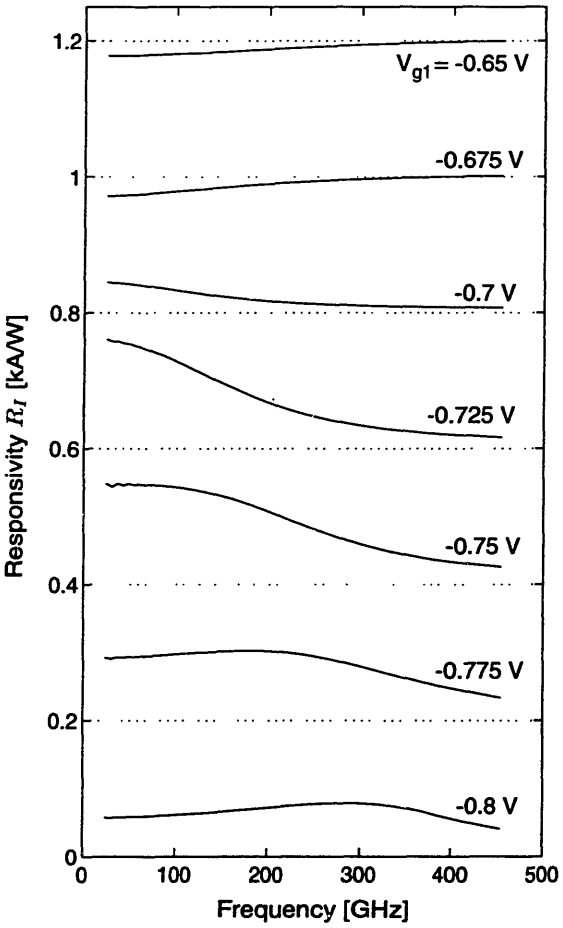

Figure 7-9: Current responsivity of a symmetric device as a function of frequency. Voltage of one gate, V_{g1}, was varied from -0.825 V to -0.6 V in steps of 25 mV, while voltage of the second gate, V_{g2}, was fixed at -0.75 V. Gate lengths were 50 nm with a separation of 130 nm. The electron reservoir temperature was 0.5 K. The curves have been vertically offset by 0.2 kA/W for clarity.

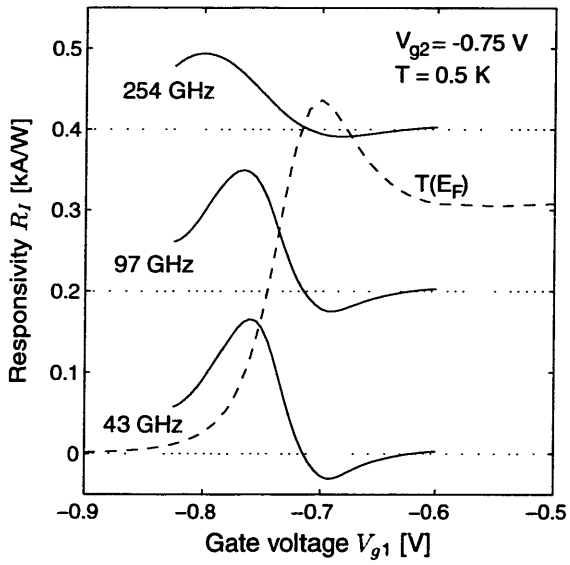

Figure 7-10: Current responsivity of a symmetric device as a function of gate voltage V_{g1}, for a radiation frequency of 43, 97, and 254 GHz. The voltage applied to the second gate was fixed at $V_{g2} = -0.75$ V. Gate lengths were 50 nm with a separation of 130 nm. The electron reservoir temperature was 0.5 K. For reference, the transmission coefficient at the Fermi energy, $T(E_F)$, is shown by the dashed line in arbitrary units. The curves for R_I are vertically offset by 200 A/W for clarity.

about 5 mV, in the same frequency interval. The peak R_I at 43 GHz is 165 A/W. Since the measured ΔI_{ds} at 39.2 GHz is 50 pA, the predicted absorbed radiation power is only 0.3 pW. As V_{g1} approaches zero, only a single barrier remains, and R_I is found to be virtually frequency independent. The responsivity for a single barrier at frequencies below 50 GHz is about 5.6 A/W, while it decreases to 5 A/W at 300 GHz. This is a change of only 10%. We conclude that the largest frequency dependent behavior is expected at the onset of conduction of the device. Further, R_I decreases as the radiation frequency is increased for a fixed P_ω^{abs}.

The simulation results show the same single peak response as seen in the data. In the measurement, even though ΔI_{ds} decreases significantly to the right of the peak, no negative current is observed. Also, the peak location does not move as a function of frequency. The absence of a negative ΔI_{ds} cannot be explained in the framework of the current model. Even if symmetric heating were considered, it would result in the same polarity of thermal current as R_I predicts. We speculate that the absence of any peak shift with frequency is because of the rapid movement of the potential profile with respect to the Fermi energy in the neighborhood of the conduction theshold.

This effect was important for the behavior of a QPC near the conduction threshold and was consistent with self-consistent simulation studies [65]. A rapid movement of the Fermi energy with respect to the potential profile below the conduction onset would result in a conduction threshold which appears to be pinned at a fixed value of V_{g1}. If this is indeed the case, the predicted frequency dependent shift would not be observable. In order to verify our hypothesis about the behavior of the Fermi energy for the dual gate device near the conduction threshold, self-consistent calculations of the system behavior would be required.

7.5 Summary

A frequency-dependent ΔI_{ds} has been observed when measuring both $I_{ds} - V_{ds}$ and $I_{ds} - V_g$. Using the modified transmission coefficient, T_ω, we have been able to reproduce the main features of the data. The observations appear to be consistent with prediction obtained from the radiation-induced transport model through the double barrier structure. Thermal heating of the electrons in the 2DEG may be present, but would not account for the frequency dependence in ΔI_{ds} unless the 2DEG absorption exhibits a dependence on both the gate voltages and the frequency.

Chapter 8

Conclusion

This thesis investigated the effects of radiation on quantum effect devices. The effort was motivated by the quest for novel radiation sensors capable of coherent detection for frequencies approaching the THz-range. Since electron transport in quantum effect devices is ballistic, quantum limited radiation detection is possible in principle. This effect is analogous to photon-assisted transport in superconducting-insulating-superconducting tunnel junctions. In the course of this work, we studied the effects of radiation on two types of devices: a quantum point contact with a gate coupled and a drain/source coupled antenna, and a dual gate device with drain/source coupled antenna. The primary accomplishments of the work are summarized below:

- The Tien-Gordon theory was extended to accommodate an energy dependent transmission coefficient. The concept of a modified transmission coefficient was introduced to describe the effects of radiation on phase-coherent electron transport through quantum effect devices.

- Planar self-complementary antennas were integrated with quantum effect devices. The antenna is used to focus the radiation field and produce an ac voltage between the antenna terminals. An individual quantum effect device is

subjected to this ac voltage, and the photo-induced change in the dc transport of the device can be measured.

- A saddle-point potential was used to model the transport characteristics of quantum point contacts. By analysis of $I_{ds}-V_g$ and the temperature dependence of the transconductance, we were able to find values for both the longitudinal and the transverse curvatures.

- The bolometric response and thermopower were studied in a quantum point contact subject to a radiation-induced ac voltage oriented transverse to the electron transport direction.

- The rectified radiation-induced current was studied in a quantum point contact with the antenna oriented along the electron transport direction.

- Evidence was observed for the existence of resonant levels in symmetric and asymmetric dual gate device. Energy level spacing agreed well with predicted values obtained from simulation.

- The experimentally observed frequency dependent response of dual gate devices was found to be consistent with predictions using the modified transmission coefficient. As a direct consequence of this interpretation, the data suggests absorption of modulation quanta $\hbar\omega$ takes place when ballistic electrons traverse the time-modulated double barrier potential.

Our efforts have resulted in partial success. Convincing evidence of absorption or emission of modulation quanta $\hbar\omega$ from the time-oscillating single barrier potential by a ballistic electron has eluded us. Although a frequency dependent radiation-induced current is observed for a dual gate device, no characteristic shift with frequency was seen, only a decrease of the amplitude of the undulations was observed. Several

mechanisms could be at work which made observation of the shift impossible. First, the gate bias voltage we applied positioned the top of the barriers near the Fermi energy. Therefore, the resonant levels observed in the $I_{ds} - V_{ds}$ measurements are very broad, and observation of the sidebands for these levels is difficult. Secondly, these levels are also most severely affected by ac distortions of the potential barrier, resulting in a rapid loss of the resonant levels. One remedy in future experiments might be to further lower the temperature, which would make it possible to utilize the sharper resonant level positioned further below the top of the barrier.

In case of the quantum point contact, we found that heating the 2DEG dominated the radiation response for a gate coupled antenna. This conclusion was based on the fact that the radiation-induced current could be completely reversed by changing the direction of incidence of the radiation. The radiation-induced current observed for a drain/source coupled quantum point contact compared well with the predicted rectification response. The response of this device did depend on the polarization of the radiation field, although the signal did not vanish when the polarization plane was oriented orthogonal to the antenna axis as was the case for the dual gate device. This supports our belief that the observed signals are partly of thermal origin and partly caused by rectification.

One major difficulty at this time is reliable fabrication of high quality quantum effect devices. We have seen evidence of both large threshold voltage shifts and poor thermal cycling characteristics. These effects make it difficult to repeat experiments for verification of device behavior, and limit the useful lifetime of the devices. In particular, these non-idealities most seriously affected the devices fabricated using very shallow 2DEGs. Elimination of the threshold voltage shifts would greatly improve the technical significance of quantum-effect devices.

We would like to conclude with a few remarks about possible future efforts. In our exploration of the radiation response of quantum effect devices, we were limited to single frequency sources which were mechanically tunable. When one performs spectroscopy, it is advantageous to use a broad-band source and to measure a complete frequency spectrum of the device response. Such a complete frequency spectrum would make comparison possible between the magnitude of the radiation-induced currents at different frequencies. Signals of spurious origin, such as cavity resonances, could then be recognized as well, and possibly eliminated. In the future, it might also be worthwhile to use the quantum effect devices as mixers. If quantum effect devices were connected to suitably designed coplanar waveguides, the ac currents induced by radiation from two sources with slightly different center frequencies could be measured. This could establish direct evidence of inelastic transport of ballistic electrons in quantum-effect devices caused by interaction with a time-modulated barrier in quantum effect devices. Finally, we believe that future efforts should focus on improving the radiation coupling into the quantum-effect device; in particular, a stronger confinement of the ac electric field must be achieved. This would enhance the process of modulation quanta absorption by the ballistic electrons and reduce the amount of heating of the 2DEG.

Appendix A

Device summary

In Table A.1 we list the key properties of the devices measured in this thesis. Each device is identified using the substrate name and a location marker. The location marker consists of a number and a character indicating the row and column on the processed wafer where the device was located. The name of the devices used in a particular experiment has been indicated in each data set.

Table A.1: Summary of pertinent information on the devices used in the experiments.

Sample	Location	Type	Polarization
m22	c2	qpc	transverse
m22	c4	qpc	transverse
6167	a1	dot	longitudinal
6167	d2	dot	longitudinal
6122	d4	tqpc	longitudinal
6122	d7	dot	longitudinal
6122	c2	asym	longitudinal

Appendix B

Device fabrication

B.1 Split-gate process

1. Basic steps

The split-gate process consists of four photolithography steps and one electron beam lithography step. These main fabrication steps are listed below in chronological order. We will also give procedures useful for glassware cleaning and initial wafer preparation. Specific details about each item on the list follows.

1. **Processware and chrome mask clean:** Newly purchased glassware and used contact chrome masks can be cleaned with this procedure.
2. **Sample degrease:** Substrate should be degreased when initially received from MBE growers and between photo steps.
3. **Mesa isolation etch (MESA):** Removes the GaAs cap layer and part of the AlGaAs layer by wet etching. As a result, the 2DEG remains intact only in regions (mesas) not etched. This photolithography step uses a clear field mask.

4. **Ohmic contacts (DIFF):** Deposition of an alloy which, during annealing, diffuses into the material and forms an ohmic contact to the 2DEG. After diffusion, the semiconductor directly under the ohmic metal is n^{++}-doped. This photolithography step is a lift-off process and uses a dark field mask.
5. **Test structures (ALIG):** Cr/Au layer defines contact pads for the TLM and Hall bar. After processing of this mask level, the test structures are complete and can be bonded. This makes it possible to measure the material characterisitics at liquid He4 temperatures. An alignment cross is also included in this level for alignment during the e-beam lithography step. This photolithography step is a lift-off process and uses a dark field mask.
6. **E-beam lithography process:** Submicron sized Au/Pd Schottky gates, defining the quantum effect device geometry, are deposited following the electron-beam processing with a JEOL 5DII e-beam system.
7. **Antenna layer (ANT):** Cr/Au layer is deposited which defines the planar antenna, the bonding pads, and the connections to the ohmic contacts and the gates. This photolithography step is a lift-off process and uses a dark field mask.

The names we used to identify each mask are given in paranthesis. For the positive photo-resist which was used for the photolithography processing, the dark field patterns are opaque, while the clear field patterns are transparant.

2. Design rules

The following design rules were followed during the layout of the photolithography mask:

- All features had an alignment tolerance greater than 5 μm, to make alignment with a contact aligner easy.

- The minimum feature size used for the contact mask was 1 μm.
- The largest grid pattern size for devices on JEOL 5DII e-beam machine at NNF was 80 $\times$ 80 μm^2. The fine features for the gate structure of the device were therefore kept smaller than this area.
- The bonding pads were made large enough to allow two or three shots with the bonder, and for a double-bond. A pad measuring 150$\times$150 μm^2 was judged to be sufficient for this purpose.
- A chip center-to-center spacing of 5 mm was used in order to expose 4 rows of chips with the JEOL 5DII e-beam machine at NNF when using the 16 mm-slot sample holder.
- The antenna layer was deposited last, so that the thin metal of the e-beam layer was covered with a thick antenna metal.
- The antenna layer only partially overlapped the ohmics layer. This made it possible to descum the exposed ohmic region before deposition of the antenna metal, without killing the 2DEG in the mesa.

'Descumming' is the removal of the residual organic scum that may be left over after development of the photoresist. The best way to clean the surface is to do a very brief RIE in oxygen — this removes the undesired photoresist in the developed areas. The oxygen plasma tends to destroy the 2DEG in areas which are not covered with photoresist. The antenna layer, therefore, only partially overlaps the ohmics.

B.2 Optical lithography process

1. Processware and chrome mask clean

1. Mix NH_3OH:H_2O_2:H_2O in ratio of 1:1:5 (make about 1 liter).
2. Heat mixture slowly to 80° C using a double beaker. Monitor temperature with a thermometer; this takes about 20 minutes.
3. Boil items for 15 minutes in solution.
4. Rinse in de-ionized water (DI) for 5 minutes.
5. Blow dry with N_2.

This solution is extremely effective in removing organic contaminants, including residual photoresist [87]. This cleaning must be done in the acid hood.

2. Sample degrease

1. Boil sample in 1,1,1-Trichloroethane (TCE) at 80° C for 5 minutes.
2. Ultrasound in TCE for 5 minutes.
3. Ultrasound in acetone for 5 minutes twice.
4. Ultrasound in methanol for 5 minutes twice.
5. Rinse in DI for 1 minute.
6. Blow dry with N_2.

Always monitor TCE during heating and use a set of teflon tweezers to agitate liquid. TCE has a tendency to overheat if left alone and can suddenly boil over when a sample is immersed into the liquid. Keep in mind that TCE is carcinogenic and avoid breathing fumes.

3. Photolithography with positive resist

1. Sample degrease with TCE, acetone and methanol.
2. Dehydration bake at 200° C for 30 minutes, cool to ambient temperature.

3. Deposit Shipley Microposit Primer (adhesion promoter) and allow contact with substrate surface for 10 s, then spin at 6500 rpm for 10 s [88].
4. Spin Shipley 1818 resist at 6500 rpm for 30 s for a 1.6 μm film thickness.
5. Soft bake at 90° C for 30 min, cool to ambient temperature.
6. Remove edge bead with acetone soaked applicator.
7. Duration of contact mask exposure is about 5 s on the standard Karl-Suss aligner (365 nm, 8 mW/cm^2).
8. (*) Chlorobenzene soak for about 2 minutes [89, 90, 91, 92].
9. (*) Blow dry with N_2.
10. (*) Bake at 90° C for 1 minute to drive out solvents.
11. Develop with Shipley premixed MF 319 developer for 60 s. When using chlorobenzene soak the developing time should increase by 15 to 20 s.
12. Rinse with DI for 2 minutes.
13. Blow dry with N_2.
14. Inspect developed areas with 100× microscope. Make sure no colored streaks are present; they indicate underexposure.
15. (**) Hardbake at 90° C (ideally at 115° C) for 30 minutes, cool to ambient temperature.

The step marked with (*) were used for lift-off processes while the step marked with (**) was used before the mesa etching. Edge beads form frequently on the front and the back side of odd shaped samples during photoresist spinning. These crests of accumulated resist along the circumfence must be removed before the sample is mounted in the aligner. This restores the even thickness of the sample, thus improves alignment and guarantees a more uniform exposure. The development time of the

photoresist varies slightly from run to run. These changes are caused by long-term variability of aligner lamp brightness, photo resist thickness changes (viscosity increases as resist ages) and developer freshness. A few test runs with dummy Si wafers is advisable to check exposure time before every run.

The chlorobenzene treatment alters the constituents of the upper region of the photo resist. As a result, the resist develops a satisfactory lift-off profile during development. The chlorobenzene soak time should be adjusted for each process run so that the appearance of the photolithographic pattern is delayed by 15 to 20 s, compared to the development time when no chlorobenzene is used. Chlorobenzene is a fairly strong narcotic and all work must be done in a well-ventilated area to avoid inhalation of fumes. It should be treated with extreme caution since it represents a severe carcinogenic health hazard.

4. Mesa isolation etch (MESA)

1. Photolithography with (**) step.
2. Mix NH_4:H_2O_2:H_2O in ratio of 5:1:240 (prepare about 500 ml).
3. Etch sample for 150 s (approximate etch rate for GaAs is 40 nm/minute).
4. Rinse with flowing DI for 2 minute.
5. Strip resist by soaking sample in acetone for 10 minutes.
6. Rinse with methanol and DI.
7. Blow dry with N_2.
8. Measure mesa height with Dektac.

The etch solution should be mixed immediately before use. Peroxide (H_2O_2) looses its effectiveness if exposed to air for an extended time. Calibration of the etch rate

was done using a blank GaAs sample. After successive etching of several samples, the etch rate decreases due to a saturation of the solution.

5. Ohmic contacts (DIFF)

1. Photolithography with (*) steps.
2. Etch sample in buffered oxide for 10 s, rinse thoroughly with flowing DI for 30 s, blow dry with N_2, and immediately afterward load the sample into the e-beam evaporator.
3. E-beam evaporate ohmic contact metals in the following order: 5 nm of Ni, 60 nm of Ge, 120 nm of Au, 30 nm of Ni, and 30 nm of Au [94, 95].
4. Lift-off by soaking sample in acetone for 10 minutes (if neccessary, ultrasound carefully after waiting for the full 10 minutes).
5. Rinse with methanol and DI.
6. Blow dry with N_2.
7. Rapid thermal anneal sample: Ramp at a rate of 30 °C/s to 250° C and hold for 10 s. Then ramp at a rate of 30 °C/s to 415-440° C and hold for 10 s. Exact anneal temperature depends on sample size and lamp condition.
8. Measure TLM structures and determine contact and sheet resistance at room temperature. Repeat annealing in increments of 5° C if contact resistance is poor. Typical values for the contact resistance and the sheet resistance are shown in Fig. B-1.

Buffered oxide, a mixture of 49% HF and NH_4F (1:7), is a diluted and less dangerous solution than concentrated HF. Nevertheless, all safety precautions must be taken

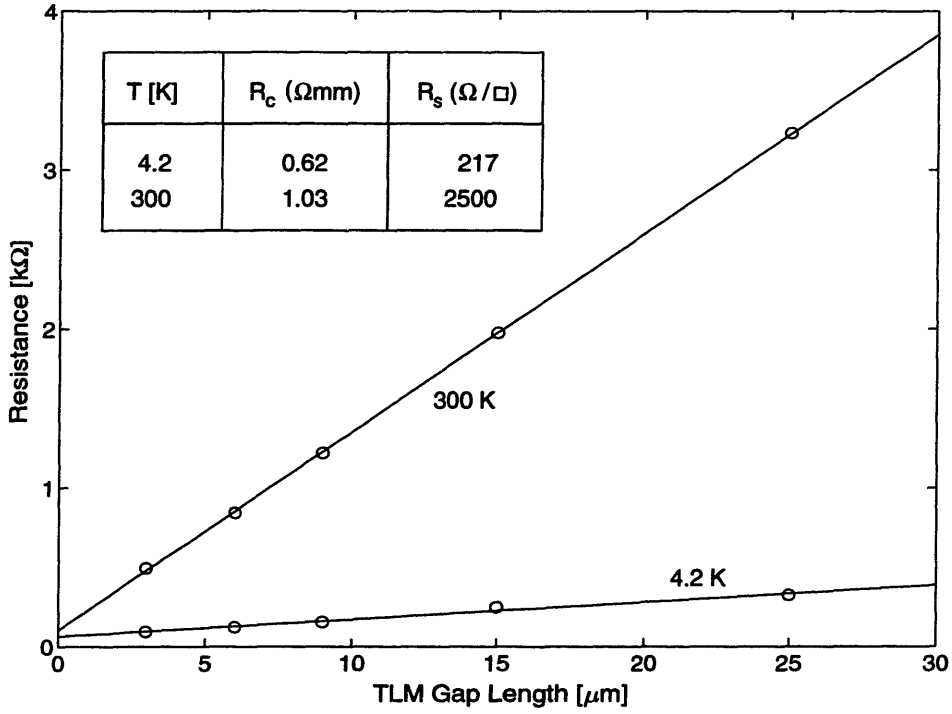

Figure B-1: Resistance measurement of 20 μm wide TLM channel on sample 6043. The 2DEG carrier concentration was 2.4×10^{11} cm^{-2}, and the mobility was 1.3×10^5 cm^2/V·s at 4.2 K.

when working with this etchant. The fluoride ion readily penetrates the skin, causing destruction of deep tissue layers and even bone.

The annealing of the samples was done using a rapid thermal annealer (RTA). A blank 2" GaAs wafer was placed on the quartz tray in the RTA, and the sample was placed face down in the center of that wafer. The blank wafer is used to reduce the variability of the anneal time for different sized samples and also provides an arsenic atmosphere during annealing. The TLM was measured using a probestation and a Hewlett&Packard 4145 parameter analyzer. Sweeping a complete $I - V$ was found to be helpful in distinguishing between an ohmic contact behavior and a Schottky contact behavior. A plot of acceptable TLM characteristics is shown in Fig. B-1 for a measurement performed at room temperature and at 4.2 K.

6. Test structures (ALIG) and antenna layer (ANT)

1. Photolithography with (*) steps.
2. Plasma descum in O_2 for 30 s at 100 W.
3. Do buffered oxide etch immediately prior to loading in thermal evaporator.
4. Thermal evaporation of metal layers in the following order: 5 nm of Cr and 200 nm of Au.
5. Lift-off layer by soaking in acetone for 10 minutes (if neccessary ultrasound carefully).
6. Rinse with methanol and DI.
7. Blow dry with N_2.

B.3 Electron-beam lithography process

Two metal film thicknesses were tried during the fabrication runs. The two layer process (marked with $*$) is used for producing the ultimate fine features, while the single layer process (marked with $**$) is used for metal depositions up to 200 nm. The devices (QPCs) made using the single layer process did not work. The split-gate separation in the design was too small and the channel conduction was pinched off at very small values of the gate voltage ($\sim$-0.1 V). Consequentely, no 2D to 1D transition was observed because of this small threshold voltage.

1. Sample degrease with TCE, acetone and methanol.
2. ($*$) Spin 3% solution of Dupont 2010 PMMA in MIBK at 4000 rpm for 30 s for a film thickness of 60 nm.
3. ($**$) Spin 6% solution of Dupont 2010 PMMA in MIBK at 6500 rpm for 30 s for a film thickness of 366 nm.
4. Bake on hotplate at 170° C for 60 minutes.
5. ($*$) Spin 3% solution of Dupont 2041 PMMA in MIBK at 5000 rpm for 30 s for a film thickness of 40 nm.
6. ($*$) Bake on hotplate at 170° C for 60 minutes.
7. Parameters for JEOL 5DII e-beam system (accelerating voltage 50 kV, beam current 75 pA): ($*$) line dose 0.75 nC/cm and area dose 300 μC/cm^2, ($**$) line dose 1.5 nC/cm and area dose 450 μC/cm^2.
8. Develop e-beam exposed pattern with a premixed solution of methyl-isobutyl-ketone (MIBK):iso-propyl alcohol (IPA) (1:3) developer for 45 s at 21° C.
9. Rinse in IPA for 1 minute.

10. Blow dry with N_2.
11. (*) Thermally evaporate 18 nm of AuPd alloy (3:2).
12. (**) E-beam evaporate in the following order: 5 nm of Cr and 200 nm of Au.
13. Lift-off layer by soaking in methylene chloride:acetone (1:3) for 10 minutes. Ultrasound carefully if neccessary to lift off remaining metal.
14. Inspect metal deposition and measure dimensions using scanning electron microscope.

Using an accelerating voltage of 50 kV, an aspect ratio of 5:1 has been achieved, but a more conservative aspect ratio of 2:1 is more reasonable without investing too much time. This limits the metal thickness of a gate line if the smallest feature metal lines are desired. The two-level electron-beam lithography process described above was developed by Dr. M. J. Rooks of the National Nanofabrication Facility at Cornell University. A detailed description of this nm-scale fabrication technology can be found in Rooks *et al.* [96].

Appendix C

Gate biasing circuit

For safety reasons, a battery-powered gate bias circuit was developed which could supply only 0 to -5 volts. This simple but convenient circuit is shown in Fig. C-1. The battery operation avoids any interference from 60 Hz noise, present on power lines. An REF-02 +5 V precision voltage reference/temperature transducer from PMI was used to obtain a stable voltage, independent of small drops in the battery voltage. Using a 10-turn 100 kΩ potentiometer, the output voltage is easily adjusted in increments of 1 mV.

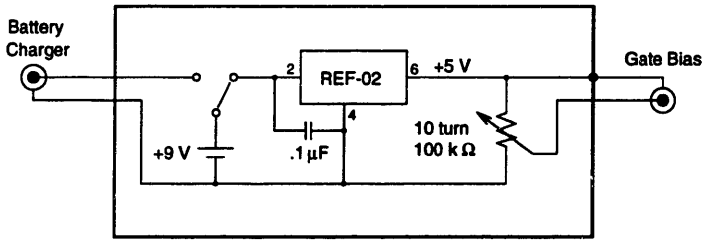

Figure C-1: Battery powered circuit for dc gate bias. Output voltage is adjustable from 0 to -5 V.

Bibliography

[1] B. J. van Wees, H. van Houten, C. W. J. Beenakker, J. G. Williamson, L. P. Kouwenhoven, D. van der Marel, and C. T. Foxon, "Quantized conductance of point contacts in a two-dimensional electron gas," Phys. Rev. Lett. **60** (9), 848–850 (1988).

[2] D. A. Wharam, T. J. Thornton, R. Newbury, M. Pepper, H. Ahmed, J. E. F. Frost, D. G. Hasko, D. C. Peacock, D. A. Ritchie, and G. A. C. Jones, "One-dimensional transport and the quantisation of the ballistic resistance," J. Phys. C **21**, L209–L214 (1988).

[3] L. P. Kouwenhoven, B. J. van Wees, C. J. P. M. Harmans, J. G. Williamson, H. van Houten, C. W. J. Beenakker, C. T. Foxon, and J. J. Harris, "Nonlinear conductance of quantum point contacts," Phys. Rev. **39** (11), 8040–8043 (1989).

[4] H. van Houten, C. W. J. Beenakker, P. H. M. van Loosdrecht, T. J. Thornton, H. Ahmed, M. Pepper, C. T. Foxon, and J. J. Harris, "Four-terminal magnetoresistance of a two-dimensional electron-gas constriction in the ballistic regime," Phys. Rev. B **37** (14), 8534–8536 (1988).

[5] B. J. van Wees, L. P. Kouwenhoven, H. van Houten, C. W. J. Beenakker, J. E. Mooij, C. T. Foxon, and J. J. Harris, "Quantized conductance of magnetoelectric

subbands in ballistic point contacts," Phys. Rev. B (Rapid Communications) **38** (5), 3625–3627 (1988).

[6] Y. Hirayama and T. Saku, "Transport characteristics of a series ballistic point contacts," Phys. Rev. B **41** (5), 2927–2930 (1990).

[7] J. C. Wu, M. N. Wybourne, W. Yindeepol, A. Weisshaar, and S. M. Goodnick, "Interference phenomena due to a double bend in a quantum wire," Appl. Phys. Lett. **59** (1), 102–104 (1991).

[8] J. A. del Alamo and C. C. Eugster, "Quantum field-effect directional coupler," Appl. Phys. Lett. **56** (1), 78–80 (1990).

[9] A. Palevski, M. Heiblum, C. P. Umbach, C. M. Knoedler, A. N. Broers, and R. H. Koch, "Lateral tunneling, ballistic transport, and spectroscopy in a two-dimensional electron gas," Phys. Rev. Lett. **62** (15), 1776–1779 (1989).

[10] S. Y. Chou, D. R. Allee, R. F. W. Pease, and J. S. Harris, Jr., "Observation of electron resonant tunneling in a lateral dual-gate resonant tunneling field-effect transistor," Appl. Phys. Lett. **55** (2), 176–178 (1989).

[11] K. Ismail, W. Chu, D. A. Antoniadis, and H. I. Smith, "Surface-superlattice effects in a grating-gate GaAs/GaAlAs modulation doped field-effect transistor," Appl. Phys. Lett. **52** (13), 1071–1073 (1988).

[12] W. Cai, T. F. Zheng, P. Hu, B. Yudanin, and M. Lax, "Model of phonon-associated electron tunneling through a semiconductor double barrier," Phys. Rev. Lett. **63** (4), 418–421 (1989); and W. Cai, T. F. Zheng, P. Hu, M. Lax, K. Shum, and R. R. Alfano, "Photon-assisted resonant tunneling through a double-barrier structure for infrared-radiation detection," Phys. Rev. Lett. **65** (1), 104–107 (1990).

[13] G. Galeczki and G. Nimtz, "Electron quantum valve device — a new type of FIR-detector," Infrared Phys. **31** (1), 85–88 (1991).

[14] G. Nimitz, A. Enders, and R. Pelster, "On the conductivity of mesoscopic metals and semiconductor structures: device aspects," Int. J. Electronics **73** (5), 983–993 (1992).

[15] Qing Hu, "Photon-assisted quantum transport in a quantum point contact," Phys. Rev. Lett. **62**, 837 (1993).

[16] T. H. Büttgenbach, R. E. Miller, M. J. Wengler, D. M. Watson, and T. G. Phillips, "A broad-band low-noise SIS receiver for submillimeter astronomy," IEEE Trans. Microwave Theory Tech. **MTT-36** (12), 1720–1726 (1988).

[17] S. Gearhart, J. Hessler, W. Bishop, T. Crowe, and G. M. Reibeiz, "A wide-band 760-GHz planar integrated Schottky receiver," IEEE Microwave Guided Wave Lett. **3** (7), 205–207 (1993).

[18] J. R. Tucker, "Quantum limited detection in tunnel junction mixers," IEEE J. Quantum Electron. **QE-15** (11), 1234–1258 (1979).

[19] H. P. Röser, H. W. Hübers, T. W. Crowe, and W. C. B. Peatman, "Nanostructure GaAs Schottky diodes for FIR-infrared heterodyne receivers," J. Appl. Phys., (Oct. 1992).

[20] L. Pfeiffer, K. W. West, H. L. Störmer, and K. W. Baldwin, Appl. Phys. Lett. **55**, 1888 (1989).

[21] G. L. Timp and R. E. Howard, "Quantum mechanical aspects of transport in nanoelectronics," Proc. IEEE **79** (8), 1188–1207 (1991).

[22] H. I. Smith and D. A. Antoniadis, "Seeking a radically new electronics," Technology Review, 26–39 (April 1990).

[23] M. Büttiker and R. Landauer, "Traversal time for tunneling," Phys. Rev. Lett. **49** (23), 1739–1742 (1982); M. Büttiker and R. Landauer, "Traversal time for tunneling," Physica Scripta **32**, 429–434 (1985); M. Büttiker and R. Landauer, "Traversal time for tunneling," IBM J. Res. Develop. **30** (5), 451–454 (1986).

[24] H. C. Liu, "Theory of ac quantum conduction through an ideal constriction," Superlattices and Microstructures **12** (1), 17–23 (1992).

[25] M. J. Hagmann, "Resonance due to the interaction of tunneling particles with modulation quanta," Appl. Phys. Lett. **66** (7), 789–791 (1995).

[26] P. Johansson, "Resonant tunneling with a time-dependent voltage," Phys. Rev. B **41** (14), 9892–9898 (1990).

[27] A.-P. Jauho, "Numerical simulations of resonant tunneling in the presence of inelastic processes," Phys. Rev. B (Rapid communications) **41** (17), 12327–12329 (1990).

[28] N. S. Wingreen, A.-P. Jauho, and Y. Meir, "Time-dependent transport through a mesoscopic structure," Phys. Rev. B (Rapid communications) **48** (11), 8487–8490 (1993)

[29] K. Yakubo, S. Feng, and Qing Hu, "Direct simulation of photon-assisted quantum transport," submitted to Phys. Rev. **B**, (April 1995).

[30] H. de Raedt and K. Michielson, "Algorithm to solve the time-dependent Schrödinger equation for a charged particle in an inhomogeneous magnetic field: Application to the Aharonov-Bohm effect," Computers in Physics **8** (5), 600–607 (1994).

[31] R. Tsu and L. Esaki, "Tunneling in a finite superlattice," Appl. Phys. Lett. **22** (11), 562–564 (1973).

[32] P. K. Tien and J. P. Gordon, "Multiphoton process observed in the interaction of microwave fields with the tunneling between superconductor films," Phys. Rev. **129** (2), 647–651 (1963).

[33] J. H. Davies, I. A. Larkin, and E. V. Sukhorukov, "Modeling the patterned two-dimensional electron gas: Electrostatics," J. Appl. Phys. **77** (9), 4504–4512 (1995).

[34] Two-dimensional Poisson solver was written by G. L. Snider, Applied and Engineering Physics Dept., Cornell University, Ithaca, NY 14853, (1992).

[35] I. N. Bronshtein and K. A. Semendyayev, *Handbook of Mathematics*, 3rd edition, ed. K. A. Hirsch, Verlag Harry Deutsch, 410 (1985).

[36] M. J. McLennan and S. Datta, Sequal v2.1 TR-EE 89-17, Simulation program which performs a quantum mechanical analysis of electron transport, School of Electrical Engineering, Purdue University, March 1989.

[37] The FWHM energy width of a Lorentzian line shape transmission coefficient is related to the resonant level lifetime τ by the uncertainty principle: $\tau \sim \hbar/\Delta E$; S. Gasiorowicz, *Quantum physics*, 365 (John Wiley & Sons, 1974).

[38] C. C. Eugster, "Electron waveguide devices," PhD thesis, MIT, 28–30 (1993).

[39] Dr. J. Smet while member of Professor C. Fonstad's group at MIT, Professor M. Melloch and coworkers at Purdue University, and Dr. A. Förster at the ISI Forschungszentrum GmbH Jülich in Germany.

[40] M. Krüger, "Einfluss der Electron-Electron-Wechselwirkung auf den electronischen Transport in 2DEG in AlGaAs/GaAs," Diplomarbeit in Physik, ISI Forschungszentrum Jülich GmbH, August 1994.

[41] P. M. Mooney, "Deep donor levels (DX centers) in III-V semiconductors," J. Appl. Phys. **67** (3), R1–R26 (1990); J. J. Plombon, W. W. Bewley, C. L. Felix, M. S. Sherwin, P. Hopkins, M. Sundaram, and A. C. Gossard, "Far-infrared capture of electrons by DX-centers," Appl. Phys. Lett. **60** (16), 1972–1974 (1992); and B. Yang, Z. Wang, Y. Cheng, J. Liang, L. Lin, Z. Zhu, B. Xu, and W. Li, "Influence of DX centers in the $Al_xGa_{1-x}As$ barrier on the low-temperature density and mobility of the two-dimensional electron gas in GaAs/AlGaAs modulation-doped heterostructure," Appl. Phys. Lett. **66** (11), 1406–1408 (1995).

[42] M. R. Melloch, D. C. Miller, and B. Das, "Effect of a GaAs buffer layer grown at low substrate temperatures on a high-electron-mobility modulation-doped two-dimensional electron gas," Appl. Phys. Lett. **54** (10), 943–945 (1989).

[43] P. F. Goldsmith, "Quasi-optical techniques at millimeter and submillimeter wavelength," Chapter 5 in Infrared and Millimeter Waves **6**, 277–343 (1982); and D. B. Rutledge, S. E. Schwarz, and A. T. Adams, "Infrared and submillimetre antennas," Infrared Phys. **18**, 713–729 (1978).

[44] H. G. Booker, J. I. E. E. **93** (3A), 620–626 (1946).

[45] D. B. Rutledge. D. P. Neikirk, and D. P. Kasilingam, "Integrated-circuit antennas," in *Infrared and Millimeter Waves* **10**, edited by K. J. Button, Academic Press, 1–87 (New York, 1983).

[46] R. C. Compton, R. C. McPhedran, Z. Popović, G. B. Rebeiz, P. Tony, D. B. Rutledge, "Bow-tie antenna on a dielectric half-space: Theory and experiment," IEEE Trans. Antennas Propag. **AP-36**, 7–12 (Nov 1988).

[47] D. B. Rutledge and M. S. Muha, "Imaging antenna arrays," IEEE Trans. Antennas Propag. **AP-30**, 535–540 (1982).

[48] T. Ando, A. B. Fowler, and F. Stern, "Electronic properties of two-dimensional systems," Rev. Mod. Phys. **54** (2), 437–672 (1982).

[49] Model 8 in. dewar with 10 T magnet and lambda tail made by Cryomagnetics Inc., Oak Ridge, Tennessee 37830.

[50] Wire-wound grid type QWG/RT. 1.5 inch diameter through aperture, wound with 10 μm diameter tungsten wire with 25 μm center-to-center spacing. Two-piece stainless frame, approximately 1/8 inch thick. Frame outer diameter nominally 2 inches. Polarizer made by QMC Instruments Ltd., Department of Physics, Queens Mary and Westfield College, London.

[51] Model P4-42 pyroelectric detector with 2 mm diameter $LiTaO_3$ senser element made by Molectron Detector Inc., Portland, OR 97224.

[52] Wideband mechanically tunable Gunn oscillator Model H104, 74-112 GHz, J. E. Carlstrom.

[53] Frequency multipliers, Model MU3-03-T2 (doubler) and MU03-03-T3 (trippler) made by Millitech Corp., P. O. Box 109, South Deerfield, MA 01373.

[54] Model 122 CO_2 pumped far-infrared laser system made by Laser Photonics Inc., Orlando, FL 32826.

[55] M. Rosenbluh, R. J. Temkin, and K. J. Button, "Submillimeter laser wavelength tables," Appl. Optics **15** (11), 2635–2644 (1976).

[56] International Cryomagnetics Inc., Indianapolis, Indiana.

[57] The speciality materials used in the construction of the quasi-optical system and the device mount can be obtained from the following suppliers: TPX is made by Mitsui Petrochemical Industries, Ltd.; the 0.5" diameter single crystal Z-cut sapphire lens was custom made by Wolf Engineering, Box 2311, New Port Beach, CA 92663; and Vespel, a material used in the construction of the optics mount, is made by Du Pont, Polymers Division, 1007 Market Street, Wilmington, DE 19898.

[58] M. Born and E. Wolf, "Principles of optics," (New York, Pergamon Press, 1970). Detailed TPX lens fabrication is described in a guide by A. D. Smith, "Aspheric TPX lens fabrication for low /F number, low loss far infrared applications," Department of Physics, University of California, Berkeley, CA, (1982).

[59] M. N. Afsar, "Precision millimeter-wave measurements of complex refractive index, complex dielectric permittivity, and loss tangent of common polymers," IEEE Trans. Instrum. Meas. **IM-36** (2), 530–536 (1987).

[60] M. N. Afsar, "Dielectric measurements of millimeter-wave materials," IEEE Trans. Microwave Theory Tech. **MTT-32** (12), 1598–1608 (1984); S. Roberts and D. D. Coon, "Far-infrared properties of Quartz and Sapphire," J. Optical Soc. America **52** (9), 1023–1029 (1962); E. V. Loewenstein, D. R. Smith, and R. L. Morgan, "Optical constants of far infrared materials," Appl. Optics **12** (2), 398–406 (1973).

[61] E. Hecht and A. Zajac, "Optics," 167–170 (Addison-Wesley Publishing Company, Inc., Reading MA, 1974).

[62] Ultralow noise precision operational amplifier OP27-EZ made by PMI, obtained from Analog Devices, Norwood, MA.

[63] Model 1212-0554 multi-section EMI/RFI π-filters made by Murata Erie, Trenton, Ontario.

[64] H. A. Fertig and B. I. Halperin, "Transmission coefficient of an electron through a saddle-point potential in a magnetic field," Phys. Rev. B **36** (15), 7969–7976 (1987).

[65] S. E. Laux, D. J. Frank, and F. Stern, "Quasi-one-dimensional electron states in a split-gate GaAs/AlGaAs heterostructure," Surface Sci. **196**, 101-106 (1988).

[66] M. Büttiker, "Quantized transmission of a saddle-point constriction," Phys. Rev. B (rapid communications) **41** (11), 7906–7909, (1990).

[67] A. Szafer and A. D. Stone, "Theory of quantum conduction through constriction," Phys. Rev. Lett. **62** (3), 300–303 (1989).

[68] E. Tekman and S. Ciraci, "Novel features of quantum conduction in a constriction," Rapid Comm., Phys. Rev. B **39** (12), 8772–8775 (1989).

[69] P. F. Bagwell and T. P. Orlando, Phys. Rev. B **40**, 1456 (1989).

[70] S. B. Kaplan and A. C. Warren, "Magnetoconductance oscillations of a quasi-one-dimensional electron gas in a parabolic transverse potential," Phys. Rev. B **34** (2), Rapid Communications, 1346–1348 (1986).

[71] D. A. Wharam, U. Ekenberg, M. Pepper, D. G. Hasko, H. Ahmed, J. E. F. Frost, D. A. Ritchie, D. C. Peacock, and G. A. C. Jones, "Empirical relation between

gate voltage and electrostatic potential in the one-dimensional electron gas of a split-gate device," Phys. Rev. B **39** (9), 6283–6286 (1988).

[72] F. Hekking and Y. V. Nazarov, "Photovoltaic effect in quantum adiabatic transport as a way to pump electrons," Phys. Rev. B **44** (20), 11506–11509 (1991).

[73] S. Feng and Qing Hu, "Far-infrared photon-assisted transport through quantum point-contact devices," Phys. Rev. B **48** (8), 5354–5365 (1993).

[74] D. D. Arnone, J. E. F. Frost, C. G. Smith, D. A. Ritchie, G. A. C. Jones, R. J. Butcher, and M. Pepper, "Effect of terahertz irradiation on ballistic transport through one-dimensional quantum point contacts," Appl. Phys. Lett. **66** (23), 3149–3151 (1995).

[75] P. Středa, "Quantized thermopower of a channel in the ballistic regime," J. Phys.: Condens. Matter **1**, 1025–1027 (1989); P. Středa, "Thermomagnetic coefficients of inversion layer in high magnetic field," J. Phys. C: Solid State Phys. **16**, L369–L374 (1983).

[76] A. M. Kreschuk, M. Yu. Martisov, T. A. Polyanskaya, I. G. Savel'ev, I. I. Saidashev, A. Ya. Shik, and Yu. V. Shmartsev, "Energy relaxation of 2D electrons at an AlGaAs/GaAs heterojunction at helium temperatures," Solid State Commun. **65** (10), 1189–1192 (1988).

[77] Model H3R-8 dewar made by Infrared Laboratories Inc., Tuscon, AZ 85719.

[78] S. Verghese, R. A. Wyss, Th. Schäpers, A. Förster, M. J. Rooks, and Qing Hu, "Photon-assisted transport through quantized energy states in a lateral dual-gate device," submitted to Rapid Communications, Phys. Rev. **B**.

[79] $F_{-1/2}(\eta) = \int_0^\infty d\epsilon\ \epsilon^{-1/2}[1 + \exp(\epsilon - \eta)]^{-1}$. For a review see J. S. Blakemore, "Approximations for Fermi-Dirac integrals, especially the function $\mathcal{F}_{1/2}(\eta)$ used

to describe electron density in a semiconductor," Solid-State Elect. **25** (11), 1067–1076 (1982).

[80] J. N. K. Connor, Mol. Phys. **15**, 13 (1968).

[81] J. M. Bigelow and J.-P. Leburton, "Self-consistent simulation of quantum transport in dual-gate field-effect transistors," J. Appl. Phys. **76**, 2887 (1994).

[82] T. C. L. G. Sollner, W. D. Goodhue, P. E. Tannenwald, C. D. Parker, and D. D. Peck, "Resonant tunneling through quantum wells at frequencies up to 2.5 THz," Appl. Phys. Lett. **43** (6), 588–590 (1983).

[83] J. S. Scott, J. P. Kaminski, M. Wanke, S. J. Allen, D. H. Chow, M. Lui, T. Y. Liu, "Terahertz frequency response of an $In_{0.53}Ga_{0.47}As$/AlAs resonant-tunneling diode," Appl. Phys. Lett. **64** (15), 1995–1997 (1994).

[84] H. C. Liu, M. Buchanan, G. C. Aers, and Z. R. Wasilewski, "Single quantum well intersubband infrared detector using GaAs-AlGaAs asymmetrical double-barrier structures," Semicond. Sci. Technol. **6**, C124–C127 (1991); and H. C. Liu, "Photoconductive gain mechanism of quantum-well intersubband infrared detectors," Appl. Phys. Lett. **60** (12), 1507–1509 (1992).

[85] B. J. Keay, P. S. S. Guimaraes, J. P. Kaminski, S. J. Allen, P. F. Hopkins, A. C. Gossard, L. T. Florez, and J. P. Harbison, "Superlattice transport in intense terahertz electric fields," Surf. Sci. **305**, 385–388 (1994).

[86] J. R. Tucker and M. J. Feldman, "Quantum detection at millimeter wavelength," Rev. Mod. Phys. **57** (4), 1055–1113 (1985).

[87] H. I. Smith, "Cleaning of oxides," MIT internal cleanroom memo, July 1985.

[88] Microposit S1400 series photo resist information sheet from Shipley Company Inc., Marlborough, MA.

[89] M. Hatzakis, B. J. Canavello, and J. M. Show, "Single-step optical lift-off process," IBM J. Res. Dev. **24**, 452–460 (1980).

[90] R. M. Halverston, M. W. MacIntyre, and W. T. Mostiff, "The mechanism of single step lift-off with chlorobenzene in a diazo-type resist," IBM J. Res. Dev. **26**, 590–595 (1982).

[91] Y. Mimura, "The mechanism of overhang formation in diazide/novolak photoresist film by chlorobenzene soak process," J. Vac. Sci. Tech. B **4** (1), 15–21 (1986).

[92] J. Smet and D. Greenberg, private communication.

[93] For general references, see R. E. Williams, "Gallium arsenide processing techniques," (Dedham, MA, Artech House, 1984), where Chapter 5 deals with wet etching techniques and chapter 6 concentrates on photolithography; or "Gallium Arsenide, Materials, Devices, and Circuits," edited by M. J. Howes and D. V. Morgan (Wiley, New York, 1986).

[94] M. Heiblum, M. I. Nathan, and C. A. Chang, "Characteristics of AuGeNi ohmic contacts to GaAs," Solid-State Elect. **25** (3), 185–195 (1982).

[95] M. Otsubo, H. Kumabe, and H. Miki, "Liquid phase epitaxial growth of GaAs from Au-Ge-Ni melts," Solid-State Elect. **20**, 617–621 (1977).

[96] M. J. Rooks, C. C. Eugster, J. A. del Alamo, G. L. Snider, and E. L. Hu, "Split-gate electron waveguide fabrication using multilayer poly(methylmethacrylate)," J. Vac. Sci. Technol. B **9** (6), 2856–2859 (1991). PMMI has been obtained from OCG (Olin and Ciba-Geigy), 5 Garret Moutain Plaza, West Paterson, NJ 07424.

THESIS PROCESSING SLIP

FIXED FIELD: ill. _____ name _____

index _____ biblio _____

► COPIES: (Archives) Aero Dewey (Eng) Hum

Lindgren Music Rotch Science

TITLE VARIES. ►☐ _____

_____

_____

NAME VARIES: ►☑ Andreas

_____

IMPRINT: (COPYRIGHT) _____

►COLLATION: 238 pp.

_____

►ADD. DEGREE: _____ ► DEPT.: _____

SUPERVISORS: _____

_____

_____ — _____

_____ — _____

_____ — _____

_____ — _____

_____ — _____

_____ — _____

_____ — _____

NOTES:

cat'r: date:

page: 544

►DEPT: E.E.

►YEAR: 1995 ►DEGREE: ~~PH~~ Ph.D.

►NAME: WYSS, Rolf A.

_____